

Application of Remote Sensing and Geographic Information Systems for Mineral Predictive Mapping, Deseado Massif, Southern Argentina

by

Raul Pablo Andrada de Palomera

Thesis submitted to the
International Institute for Geo-information Science and Earth Observation
in partial fulfilment of the requirements for the degree of
Master of Science in Geo-information Science and Earth Observation for
Mineral Resource Exploration

Degree Assessment Board:

Dr. K. Hein (External examiner)

Prof. Dr. F.D. van der Meer (Chair)

Dr. E.J.M. Carranza (1st supervisor, member)

Drs. F. van Ruitenbeek (2nd supervisor, member)

Drs. J.B. de Smeth (Acting EREG Programme Director, member)



**INTERNATIONAL INSTITUTE FOR GEO-INFORMATION SCIENCE AND EARTH OBSERVATION
ENSCHEDÉ, THE NETHERLANDS**

Disclaimer

This document describes work undertaken as part of a programme of study at the International Institute for Geo-information Science and Earth Observation. All views and opinions expressed therein remain the sole responsibility of the author, and do not necessarily represent those of the institute.

Abstract

The study of geological characteristics of low-sulfidation epithermal deposits (LSED) elsewhere and in the Deseado Massif, and Fry analysis (point pattern analysis) of spatial distributions of LSED in the study area were carried out to determine geological controls on LSED that could be used as spatial evidences for predictive mapping of LSED potential on regional and district scales.

The Fry analyses indicate that the LSED are structurally controlled and there are differences in strengths of regional structural controls on LSED in different parts of the area. In the western half of the area, fractures with azimuth orientations of 145-170° and of 105-125° were the principal structural controls. In the eastern half of the area, fractures with azimuth orientations of 40-60° were the principal structural controls although structural controls by fracture systems with NW trends are apparent but weaker. The differences in strengths of structural controls by different fracture systems in different parts of the area are probably due to migration in time of volcanism, fracture generation, and mineralization from ENE to WSW and by the changes in the stress directions during the Jurassic.

Based on literatures of previous works in the area and based on results of Fry analysis, geological features indicative of LSED on a regional scale are (a) presence of Chon Aike, La Matilde and Bajo Pobre Formations; (b) presence of regional NW-trending fractures, and (c) presence of clay alteration. The indicative lithological features were extracted from regional scale geological maps. The indicative structural features were extracted from shaded-relief images of a digital elevation model. The indicative hydrothermal alteration features were extracted from Landsat data. Based on literatures of previous works in the area, geological features indicative of LSED on a district scale are (a) presence of pre-Bajo Grande Formations; (b) density of fractures (considering all fractures), and (c) presence of clay alteration and abundance of silica. The “mineralogical” indicative features (i.e., clay and silica) were extracted from ASTER data. The spatial associations of these regional and district scale geological features with known LSED were quantified by way of weights-of-evidence analysis.

On a regional scale, the indicative lithological features are shown to have strongest spatial association with the LSED in the area. Of the two sets of fracture systems, those with azimuth orientations of 145-170° are positively spatially associated with the LSED while those with azimuth orientations of 105-125° lack spatial association with the LSED. The mapped clay alteration shows weakest positive spatial association with the LSED. Spatial evidences used in regional scale predictive modelling were (a) favorable lithologies, (b) fractures with azimuth orientations of 145-170° and (c) clay alteration. The predictive model delineates 16,630 km² (23.5% of total area of 70,828 km²) as zones favorable for occurrence of LSED. The regional scale predictive model has a success rate of 80% (i.e., percentage of training deposits in predicted favorable zones) and a prediction rate of 100% (i.e., percentage of validation deposits in predicted favorable zones).

For district scale predictive modelling, weights-of-evidence analysis was carried out only inside areas of the favorable lithologies. The structural and mineralogical evidences are positively spatially associated with the LSED although spatial association of the former with the LSED is stronger. Predictive modelling in the area covered by favorable lithologies resulted in delineation of 671 km² (12.65% of area covered by favorable lithology) of zones favorable for occurrence of LSED. The district predictive model has a success rate of 77% (i.e., percentage of training deposits in predicted favorable zones) and a prediction rate of 100% (i.e., percentage of validation deposits in predicted favorable zones).

Comparison of results of weights-of-evidence modelling at regional and district scales show that the available datasets can be applied to assist the process of sequentially reducing grounds of interest during mineral exploration in the area.

Acknowledgement

I would like to acknowledge ITC and the Dutch Government for granting me the scholarship to study in The Netherlands, and my Company, Fomicruz S.E. for allowing me to be absent all this time and providing economic support; specially to Ing. Roberto Traba for his encouragement and support from the beginning, to Miguel Ferro, Dr. Norma Abuin and Lic. Daniel Pérez for their support.

I want to thank Dr. John Carranza, my supervisor, for his guidance and great corrections to my drafts, but mainly for inducing me to think in a more critical and scientific way.

I want to express my gratitude to Drs. Frank van Ruitenbeek, my second supervisor, for corrections and recommendations and to Drs. Boudewijn de Smeth for his continuous support during all the time I was in ITC.

I am grateful to Prof. Dr. Martin Hale for his very useful advice and to Prof. Dr. Freek van der Meer for his technical recommendations.

Thanks to Dr. Raul Fernández, Lic. Karina Mykietiuk, Lic. Mario Tessone and Lic. Daniel Vargas for providing geological information.

Thanks to all the friends I made during my stay in Enschede, whom I will remember for ever for making my life here more pleasant.

I am grateful to my mother, father and sister, and my friends in Argentina for their support in several ways.

My special gratitude to Pia and Pili, my wife and daughter, for joining me in this enterprise since the time it was planned to its end.

Contents

Abstract	iii
Acknowledgement	iv
Contents	v
List of figures	vi
List of tables	vii
CHAPTER 1: Introduction.....	1
1.1. Background to the research.....	1
1.2. Research problem definition	2
1.3. Research objectives	2
1.4. General Research Methodology.....	3
CHAPTER 2: The Study Area	5
2.1. Location.....	5
2.2. Lithostratigraphy of the Deseado Massif	5
2.3. Structural geology of the Deseado Massif	8
2.4. Regional tectonic evolution of the Deseado Massif.....	9
2.4.1. Tectonic evolution of the basement	10
2.4.2. Tectonic evolution during the Gondwanic cycle.....	11
2.4.3. Tectonic evolution during the break up of Gondwanaland	11
2.5. Epithermal gold mineralization in the Deseado Massif	12
2.6. Discussion.....	14
2.7. Conclusions	16
CHAPTER 3: Conceptual LSED Exploration Model	17
3.1. General characteristics of LSED.....	17
3.2. General guidelines for exploration of LSED	19
3.3. Distribution patterns of LSED in the Deseado Massif	20
3.3.1. Fry analysis	21
3.3.2. Results of Fry analysis	22
3.4. Discussion of results	27
3.5. LSED recognition criteria.....	29
3.6. Concluding remarks	30
CHAPTER 4: Extraction of Geological Features.....	31
4.1. General considerations.....	31
4.2. Extraction of regional scale geological features	34
4.2.1. Regional scale lithological features.....	34
4.2.2. Regional scale hydrothermal alteration	35
4.2.3. Regional scale structural features.....	39
4.3. Extraction of district scale geological features	40
4.3.1. District scale lithological features	40
4.3.2. District scale hydrothermal alteration	40
4.3.3. District scale structural features	42
4.4. Concluding remarks	44
CHAPTER 5: Predictive Mapping of LSED Potential.....	45
5.1. Weight-of-evidence (WofE) method	45
5.1.1. WofE calculations	45
5.1.2. Tests of conditional independence	48
5.2. WofE application to regional scale mapping of LSED potential	50
5.2.1. Spatial association of LSED with regional scale geological features.....	50
5.2.2. Regional scale prediction of mineralized zones	55
5.3. WofE application to district scale mapping of LSED potential	58
5.3.1. Spatial association of LSED with district scale geological features.....	58
5.3.2. District scale prediction of mineralized zones	61
5.4. Discussion and concluding remarks.....	63
CHAPTER 6: Conclusions and Recommendations.....	65
6.1. Conclusions	65
6.1.1. Geological controls of LSED in Deseado Massif	65
6.1.2. Mapping of geological features indicative of LSED	66

6.1.3. Predictive mapping of LSED potential.....	66
6.2. Recommendations	67
References	69

List of figures

Figure 2.1: Location of Deseado Massif (in light orange surrounded by dashed lines) showing main lithological units (modified from Schalamuk et al., 2002).	5
Figure 2.2: Schematic section of the Deseado Massif. The area is divided into blocks by NNW-SSE regional fault systems. And the blocks are slightly tilted to the east (modified from Ramos, 2002).	9
Figure 2.3: Geotectonic framework of the Argentinian Patagonia.	10
Figure 3.1: Schematic model of a low-sulfidation epithermal system (from Hedenquist et al., 2000).	18
Figure 3.2: Temperature and pH stability of some hydrothermal minerals (from Hedenquist et al., 2000).	19
Figure 3.3: Graph showing relative vertical positions of pathfinder metals halos in an ore deposit of low-sulfidation epithermal style (modified from Hoffman, 1986; and Pirajno, 1992).	19
Figure 3.4: Map of study area showing locations of 48 LSED used in the Fry analysis.	23
Figure 3.5: Graph generated using all deposits available (48 deposits). a) Fry plot with 2256 translations obtained using all the deposits. b) Rose diagram of all translations. A predominant direction at 120°-130° and a less strong one at 160°-170° are easily recognized in a) and b) ; others at 90°-100°, at 140°-150°, and at 50°-60° can be recognized in the rose diagram but are not obvious in the Fry plot. c) Rose diagram of translations of less than 100 km length showing possible enhanced local controls at 50°-60°.	24
Figure 3.6: Fry plot and its corresponding rose diagram for 39 deposits hosted in Bahía Laura Group.	25
Figure 3.7: Graphs generated with points of the western and eastern sectors. In the west a general NW trend is emphasized, in the east the NE trend is predominant and the NW trends are secondary or absent.	26
Figure 3.8: Map of the Deseado Massif showing lithology, approximate position of regional scale fractures zones that divide the Deseado Massif in large blocks (Ramos, 2002), rose diagrams for the western and eastern sectors, and directional plots of four district scale areas called Cerro Saavedra, Josefina-Esperanza, Cerro Vanguardia and Martinetas-La Paloma.	27
Figure 3.9: Comparison of five rose diagrams generated from four sets of deposits, and of four directional diagrams for deposits in four district scale areas of the Deseado Massif	29
Figure 4.1: Spectra of some alteration minerals showing their characteristic absorptions pikes, and wavelength intervals of Landsat ETM and ASTER bands (modified from Sabins, 1999).	32
Figure 4.2: Rock emissivity minima in the thermal range of the spectrum and their shifts to shorter wavelengths as silica content increases. Also shown are the ASTER thermal bands (modified from Sabins, 1999).	33
Figure 4.3: Geological map of the Deseado Massif compiled by digitization of seven 1:250,000 scale geological maps produced by SEGEMAR.	35
Figure 4.4: Map of regional scale lithological evidence. Chon Aike, La Matilde, Bajo Pobre, and Roca Blanca Formations have been grouped in one unit.	36
Figure 4.5: Comparison of the results of clay alteration mapping in the La Josefina test area. a) Ratios of band 5 to 7; b) Principal component image 4 from the PCA of bands 1, 4, 5 and 7. The ratio technique shows slightly better contrast, although both enhance areas with known alteration.	37
Figure 4.6: Map of regional scale clay alteration. Ratio image of bands 5 to 7 of Landsat 7 ETM+ have been filtered (by a low pass 9x9 kernel size filter) and thresholded to generate this map.	38
Figure 4.7: Regional scale lineaments interpreted and digitized over shaded relief images of a DEM with visual support of mosaicked Landsat images.	39
Figure 4.8: Reflectance curves for four common alteration minerals and ASTER SWIR and VNIR spectral bands. Curves were produced with data from the JPL1 spectral library with materials of less than 45 microns grain size (Grove et al., 1992).	41
Figure 4.9: Results obtained with different alteration mapping techniques in the La Josefina test area. a) and b) were applied to TIR bands to map silica content; c) , d) , e) and f) were applied to SWIR bands to map clay alteration. Result in each case, were stretched in the same way to compare them (first, linear stretch to 255 possible values; second, 1% histogram stretch for better display). Red polygons indicate presence of clays including kaolinite in the south-central part; blue polygons represent opaline silica; and cyan polygons are silicified rocks; usually the opaline silica in the west is surrounded by some argillized rocks.	42

Figure 4.10: Images produced for district scale potential mapping. a) Clay alteration image produced from SWIR bands of ASTER. b) Silica alteration image (k-Index) generated from TIR bands of ASTER. c) Lineament density image produced from lineaments interpreted from Landsat images and derived products. White dots are mineral deposits.	43
Fig. 5.1: Venn diagram showing an area of study T , an area covered by mineral deposits D , and an area covered by a binary predictor pattern B , which represents certain evidence that can be used to update the prior probability of deposit; D and B means presence while \bar{D} and \bar{B} means absence of binary patterns.	46
Fig. 5.2: Proximity to regional scale fractures with azimuth orientations of 105-125° used as one set of regional scale structural evidence.	51
Fig. 5.3: Proximity to regional scale fractures with azimuth orientations of 145-170° considered to represent fractures produced by extension during Jurassic rifting and used here as one set of regional scale structural evidence.	52
Fig. 5.4: Change of contrast (C) and studentized contrast ($SigC$) with cumulative distance class for structures with azimuth orientations of 105-125°.	52
Fig. 5.5: Binary predictor maps used in regional scale mapping of LSED potential. Map c) was excluded from the combination of predictor maps.	54
Fig. 5.6: Regional posterior probability map for LSED of the Deseado Massif generated by combination of lithological, alteration and structural evidences through weights of evidence method. Blue and red colors indicate posterior probabilities higher than the prior probability.	56
Fig. 5.7: Binary regional LSED favorability map. The set of mineral deposits used for prediction and the set used for validation are overlapped on the favorability map. The area in the slanted box was selected for district scale mapping of LSED potential.	57
Fig. 5.8: Evidence maps used for district scale WofE modelling. (a) Clay alteration map and (b) K-silica index map were buffered in steps of 200 m up to 600 m. (c) Density sliced map of density of lineaments; density classes were determined using percentiles.	58
Fig. 5.9 Evidence maps used for district scale WofE modelling only inside areas of favorable lithology. Clay alteration map (a) , silica abundance map (b) and density of lineaments map (c) were classified using percentile classes.	59
Fig. 5.10 Binary predictor maps (weight maps) used for the district scale potential mapping. a) Map of clay alteration. b) Map of silica abundance. c) Map of lineament density.	61
Fig. 5.11 Classified district scale LSED posterior probability map (a) and classified favorability map (b) . Mineral deposits used for prediction and validation are overlaid.	62

List of tables

Table 2.1: Approximate area of Pre-Bajo Grande Units outcropping in the Deseado Massif and percentage of a total of 29 deposits that is hosted by each unit.	13
Table 3.1: Predominant (P) and secondary (S) directions recognized in Fry plots and corresponding rose diagrams generated with different sets of deposits. Range according to a certain length is used to restrict translations plotted in a rose diagram.	28
Table 4.1: Characteristics of Landsat ETM and ASTER bands.	32
Table 5.1: Contingency table showing four possible overlap conditions (cells in grey) between two binary predictor patterns and binary patterns of mineral deposits (Modified from Bonham-Carter, 1994).	49
Table 5.2: List of equations used for WofE calculations. Std =standard deviation; $npixt$ =total pixels in study area; $npixd$ =pixels with deposits; $npixb$ =pixels of present binary pattern or cumulative buffer class; $npixbd$ =pixels of present binary pattern or cumulative buffer class with deposits. (m_1, m_2, m_n) =predictor (weight) maps. $PostPro$ =posterior probability map. $N\{D\}pred$ = predicted number of deposit; Pp =posterior probability of each pixel in posterior probability map; $npix$ =number of pixels with certain posterior probability. (Compiled from Bonham-Carter, 1994; Carranza, 2003)	50
Table 5.3: WofE calculations for the four regional evidence maps. Lithology includes Chon Aike, La Matilde and Bajo Pobre Formations. Bold italics indicate threshold values used to create binary predictor patterns.	53
Table 5.4: Values of X^2 obtained in pairwise test of conditional independence for regional scale mapping.	54
Table 5.5: WofE calculations only inside areas of favorable lithology (Pre-Bajo Grande Formations). Note the negative values of $W+$ and C obtained for the set of structures with azimuth orientations of 105-125°.	55
Table 5.6: Result of overall test of conditional independence for posterior probability map shown in Fig. 5.6.	56
Table 5.7: Calculation of weights and contrasts only inside areas of favorable lithology. Bold italics indicate the selected threshold cumulative classes to create binary predictor maps.	60
Table 5.8: Values of X^2 obtained in pairwise test of conditional independence for district scale mapping.	61

Table 5.9: Result of overall test of conditional independence for posterior probability map shown in Fig. 5.11a.63
Table 5.10: Confusion matrix derived from cross operation of regional scale and district scale favorability maps to compare results of potential mapping at both scales in zones of favorable lithology in the district scale area. Values in the matrix are number of 100x100m pixels.64

CHAPTER 1: Introduction

1.1. Background to the research

Metalliferous deposits have been exploited to cover the necessities of developing countries; however, the prices of most metals have strongly decreased in the last years. Prices of some metals like gold and platinum group metals have nevertheless, been always in a better position in comparison to most other metals. Gold prices have risen again and this gives good expectations for the market in following years. Therefore, exploration for gold is still one of the best options for many mining companies.

A company that implements mineral prospection or exploration programs usually carries out work at many different scales (from small to large) with the objective to release and to retain barren and potentially-mineralized areas respectively, out of the initially acquired exploration areas, until it ends up with areas worthy enough for drilling. During these mineral exploration programs, abundant data of different types are generated. Various datasets from geological, geochemical, geophysical surveys, different remote sensing (RS) data (including satellite images and aerial photographs), and topographic data, have to be managed and integrated to define target areas. In the past, such integration of multiple datasets was done in analogical way, overlapping different layers of information by means of transparencies in an attempt to discover relationships between layers. Today this integration of datasets can be done digitally using a Geographic Information System (GIS).

A GIS is a computer-based system which main purpose is to provide support for making decisions using spatial data. This purpose can be achieved through organizing, visualizing, querying, combining, or analyzing data, or by making predictions with that data (Bonham-Carter, 1994). The ultimate objective of using a GIS during mineral exploration is to predict the approximate positions of new mineral deposits. For doing this, the data to be integrated should be indicative of the mineral deposits searched, according to an exploration model customized for the area under analysis.

Remote sensing data often constitutes an important part of the database introduced in a GIS because of its intrinsic digital nature, and because it can be used as the base over which to overlap other data (Legg, 1994). Satellite RS provides invaluable help when carrying out exploration activities in remote areas with poor or not up-to-date topographic maps. Even without sophisticated treatments, RS data are a useful source of information for logistic purposes, including recognition of roads, tracks, land use, general topography, presence of surface water and drainage system. If bands of satellite imagery are combined in a natural color composite they can give a general idea of some geological characteristics, like presence of very reflective clay minerals or the position and direction of the main structures. The use of RS data allows effective localization of targets and reducing costs and time spent during geophysical, geochemical and fieldwork prospection (Rokos et al., 2000). Time consumed for geological mapping of a prospective area can be greatly diminished by the use of RS techniques.

There are two general approaches for using remote sensing in mineral exploration (Sabins, 1999). One approach is to map geology and structures at regional and local scale; the other is to recognize hydrothermal alteration that can be associated to mineral deposits. Because geology, structure and hydrothermal alteration can be used as indications of the presence of mineral deposits, a combination of both approaches, which can be done in a GIS, is convenient. In addition, topographic data in the form of digital elevation models can be combined with remotely sensed imagery to map geological features indicative of mineralization of the type sought (Rokos et al., 2000).

Mineral potential mapping (MPM) is a process of spatial prediction that has the objective of delineating areas with different probabilities of hosting certain types of mineralization. Mineral

potential mapping is carried out by integrating different types of geo-data that provide useful indications of mineral deposits of interest. A GIS is therefore useful for MPM. The main steps in generating mineral potential maps are (Wright and Bonham-Carter, 1996): (1) establishing the exploration conceptual model; (2) building a spatial database; (3) spatial data analysis (extraction of evidence maps and assigning of weights); and (4) combination of evidence maps to predict mineral potential.

1.2. Research problem definition

This research is focused on the applications of geographical information systems and remote sensing in the exploration of low-sulfidation epithermal deposits (LSED) in the Deseado Massif, Southern Argentina. Mining is one way to improve the economic growth of the area, and is an activity, that from many years to now, the local Government is trying to promote. Due to the possibilities of the area, investments in mineral exploration can be attracted. However, the potential investors usually require organized datasets to decide if the area fits their expectations, to plan their exploration activities, for making decisions, etc. Therefore, the importance of having access to such datasets for the promotion of the area is huge. Mineral potential maps can be an important part of those datasets; such maps help to focus exploration efforts over the most prospective areas, thereby increasing the chances of mineral discoveries and optimizing exploration expenditures. In addition, they can be employed for planning the land uses by predicting future exploration activities (Boleneus et al., 2001). However, there is no mineral potential map comprising the whole area of the Deseado Massif.

The main reason for the lack of mineral potential maps in the area is that the Deseado Massif is poorly explored. The area is thought, however, to have high potentiality for new Au-Ag discoveries (Schalamuk et al., 2002). Despite this notion, there is a paucity of research about the geological controls of the gold mineralization in the whole Deseado Massif. Studies of structural controls of gold mineralization in the area are scarce and localized in small areas (Marchionni et al., 1999; Mykietiuik et al., 2000; Mykietiuik et al., 2002). While it is generally known that most LSED in the area are locally hosted by structures with directions that vary from N-S to E-W (Schalamuk et al., 2002), some exceptions exist such as Eureka, Rio Pinturas, Laguna Guadalosa and part of La Josefina. It is therefore important to establish the regional and district structural controls of known gold occurrences in order to generate gold potential maps.

This research tend to answer three main questions:

- (1) How can geological controls for LSED in the Deseado Massif be deduced from available data?
- (2) How can geological indications for LSED in the Deseado Massif be mapped from available data?
- (3) How can potentially mineralized zones in the Deseado Massif be mapped using available geological maps and remotely sensed data?

1.3. Research objectives

This research work had three main objectives:

- (1) To explain the mineral deposit distribution in the Deseado Massif by geological controls.
- (2) To produce maps for the main geological indicators of LSED in the Deseado Massif.
- (3) To generate a mineral potential map for the Deseado Massif using geological data and remote sensing data.

1.4. General Research Methodology

The four main steps defined above for mineral potential mapping (section 1.1) set the guides for this research work. During the first step, the conceptual exploration model for LSED in the Deseado Massif was established. First, the general characteristics of LSED were defined through a comprehensive literature review and then the characteristics of the LSED in the Deseado Massif were analyzed. This was partially done by studying the spatial distribution of the mineral deposits in the area. The analysis of point maps by means of Fry plots was used to determine the possible structural controls on mineral deposition. Finally, the deposit recognition criteria for the LSED in the area under analysis were established.

During the second step, a database was generated using available data. This consisted in the main following tasks: (a) digitization of seven geological maps at scale 1:250,000 covering the study area; (b) digitizing of linear features likely to have a structural meaning; (c) generation of a map of the 48 most important gold mineral deposits present in the area (that would be subsequently used during most of the data analysis); (d) compilation and digitization of the clay and silica alteration maps of one known area; (e) acquisition of 11 Landsat7 ETM+ satellite images, and generation of a mosaic using part of those images to cover the whole study area; (f) acquisition of ASTER images covering most of the area under study and generation of a mosaic with them.

The third step was divided in three parts. The first part consisted in the reorganization of geological datasets, processing of remote sensing data for generation of clay mineral alteration maps and lineament density maps. During the second part, evidence maps were extracted from the database according to the conceptual models and deposit recognition criteria determined before. Finally, the spatial association between the different evidence maps and the known deposits was quantified, and in this way, weights were assigned to each one of them.

The fourth step involved the combination of the evidence maps, with their weights, to generate a predictive mineral potential map. Finally, a small set of deposits and mineral occurrences was used to validate the predictive map.

CHAPTER 2: The Study Area

2.1. Location

The Deseado Massif is located in the southernmost part of the Extra-Andean Patagonia in southern Argentina (Fig 2.1). It covers an area of about 60,000 km² and is located approximately between latitudes 46°20'S and 50°00'S and between longitudes 65°30'W and 70°55'W. The Deseado Massif consists of a large non-deformed stable area that had a positive relief through most of its history (Harrington, 1962). It is composed in great part by Upper Jurassic pyroclastic and lava flows of acid to mesosilicic composition.

The Deseado Massif was considered as one of the Argentinean geological provinces by Leanza (1958) and Ramos (1999), and as a Mesozoic gold-silver metallogenic province" (Schalamuk et al., 2002). In agreement with those authors, the Deseado Massif is considered in this thesis as a geological and metallogenic province.

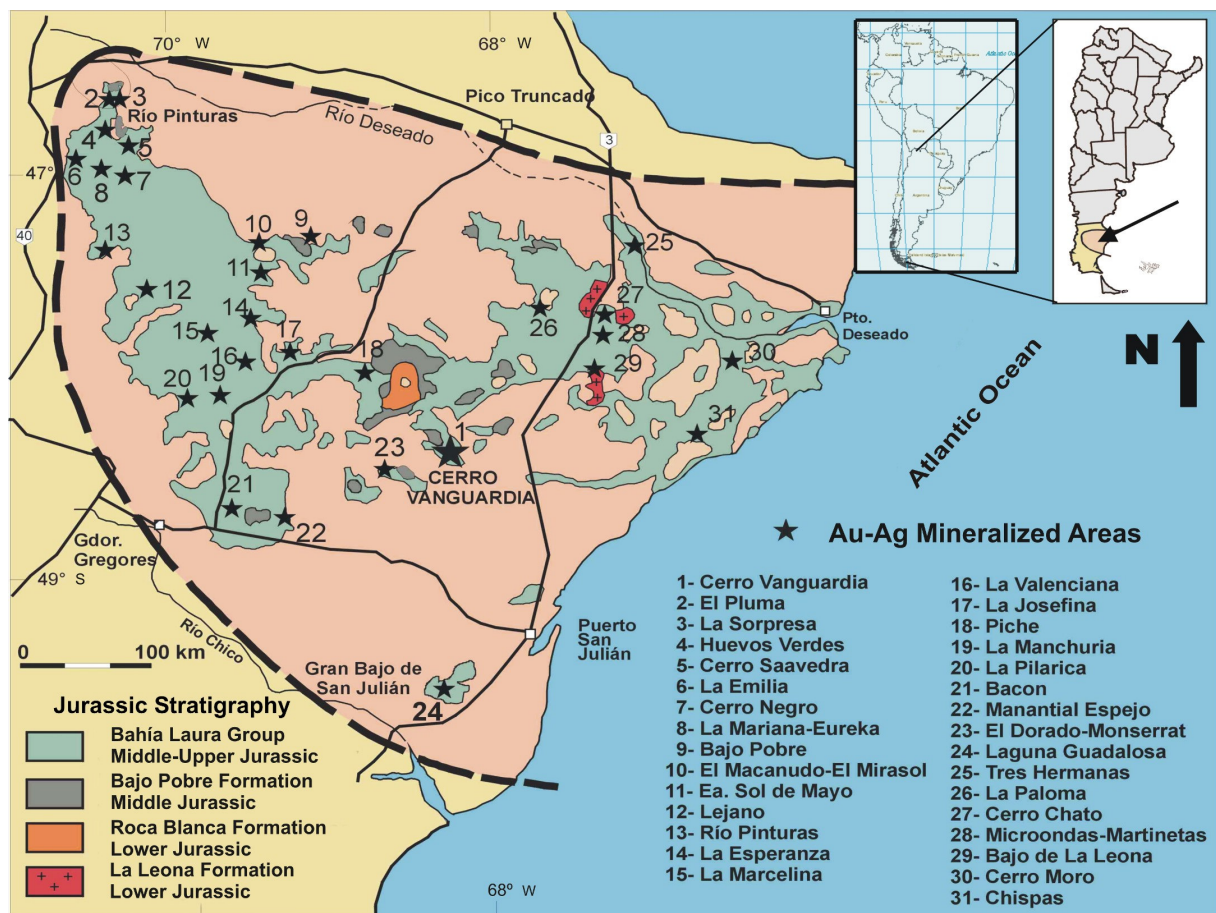


Figure 2.1: Location of Deseado Massif (in light orange surrounded by dashed lines) showing main lithological units (modified from Schalamuk et al., 2002).

2.2. Lithostratigraphy of the Deseado Massif

The oldest rocks in the area are small outcrops of low and medium grade metamorphic rocks of Upper Precambrian to Lower Paleozoic age (Schalamuk et al., 2002) with different degrees of magmatic silicic injection (Panza and Cobos, 2001). A K/Ar date of 540 ± 20 Ma was reported for the basement

rocks (Pezzuchi, 1978), which are called La Modesta Formation and consisting of schists, phyllites, slates, quartzites, gneisses, and amphibolites. The metamorphic rocks are intruded by granitic and tonalitic rocks of 470-400 Ma age (Chebli and Ferello, 1974) with ductile to ductile-fragile deformations (Giacosa et al., 2002; Ramos, 2002). The rocks of La Modesta Formation were probably generated by moderate regional metamorphism (Panza and Cobos, 2001). These metamorphic rocks are considered to be allochthonous and represent an exotic terrain accreted to the Gondwana continent before Late Devonian or even during Middle Permian (Mpodozis and Ramos, 1989; Ramos, 1984; Ramos et al., 1986). These rocks are grouped in this work with the denomination of “Pre-Permian” Formations.

Unconformably overlying the Pre-Permian rocks is a group of continental sediments ascribed to the Permian Formations La Golondrina (Archangelsky, 1958) and La Juanita (Arrondo, 1972), and to the Triassic Formation El Tranquilo (Di Persia, 1962). La Golondrina (Archangelsky, 1958, 1967) and La Juanita Formations are composed of continental sedimentary rocks including a thick sequence (thickness up to 2200 m for La Golondrina and 220 m for La Juanita) of quarto-feldspathic sandstones, siltstones lithic sandstones, and conglomerates. These sediments were deposited in N-S to NNW trending fault-bounded depocenters (de Barrio et al., 1986) and are interpreted to be synrift sediments deposited in intracratonic rift basins (Palma and Ubaldón, 1988). The N-S or NNW-SSE direction of the basins is probably inherited from the pre-existing structural configuration of the Early Paleozoic basement (Uliana et al., 1989). Outcrops of these Formations are present just in the eastern part of the Deseado Massif and their extension is very limited.

El Tranquilo Formation (Di Persia, 1956) of Middle or even Lower to Upper Triassic age (De Giusto et al., 1980) is also composed of continental sedimentary deposits, with a total thickness of 600 to 650 m (Panza, 1994) and constitutes a very small portion of the outcrops of the Deseado Massif. Its depositional environments were probably alluvial plains. It consists of rhythmically alternating fine to coarse quartz sandstones and shales in the lower part and shales, fine conglomerates and redbed sandstones in the upper part (Sanders, 2000). In its middle parts, the succession contains synsedimentary volcanics and shows simultaneous coarsening, which is indicative of relief reactivation.

Following the deposition of El Tranquilo Formation, a long hiatus in sedimentation occurred in the Deseado Massif. During Lower Jurassic, in the NE of the Deseado Massif, granitic rocks called La Leona Formation, related to the opening of the Atlantic Ocean were intruded (Varela et al., 1991). These rocks are I-type granitic rocks (Márquez et al., 2002) with compositions corresponding to calc-alkaline granodiorites, granites, adamellites, tonalites and diorites, and with compositional tendencies to be alkaline in its youngest part (Godeas, 1985). These intrusive rocks are considered post-tectonic rocks emplaced in a back-arc setting by De Barrio et al. (1986); however, other authors (Forsythe, 1982; Márquez et al., 2002; Ramos, 1983) considered that they might have been part of a magmatic arc.

During the rest of the Jurassic, in a general extensional tectonic environment, great amounts of pyroclastic rocks were emplaced including those early deposits corresponding to the Roca Blanca Formation (De Giusto, 1956; Di Persia, 1956; Herbst, 1965), and later deposits belonging to the Bajo Pobre Formation (Lesta and Ferello, 1972) and to the Bahía Laura Group (Lesta and Ferello, 1972).

The Roca Blanca Formation comprises a subaerial sequence of tuffs, sandstones, mudstones and volcanoclastic-sedimentary rocks of Liassic (Lower Jurassic) age. In the lower two thirds of the Formation, psamites are dominant and become coarser towards the top. Over the entire Formation, pyroclastic materials are abundant, but in its upper third intercalated tuffs are predominant (Panza, 1994). This Formation has a maximum thickness of 900 m (Panza, 1982). The sediments of this Formation seem to have been deposited in a fluvial to lacustrine environment, and the source of the pyroclastic materials was interpreted to have been a rhyolitic volcanism outside the Deseado Massif (de Barrio et al., 1986). The deposition may have occurred in fault-driven active rift basins (Sanders,

2000). The Roca Blanca Formation is usually covered by the basalts and volcanic agglomerates of Bajo Pobre Formation or by rocks of the Bahía Laura Group, which lie unconformable over it (Panza, 1982).

The Bajo Pobre Formation, of middle Jurassic age, is composed of more predominantly porphyritic to aphanitic olivine basalts and less predominantly of porphyritic andesites, basaltic agglomerates, and minor mafic tuffs, conglomerates and sediments (Sanders, 2000). The bottom of this Formation is characterized by altered basaltic lava flows, while the upper parts are characterized by intercalations of pyroclastic and sedimentary materials, including volcanic agglomerates. The mean thickness of the Formation varies from 150 to 200 m in most of the outcrops, but it reaches up to 600 m locally (Panza, 1994). The volcanic rocks of the Bajo Pobre Formation resulted from fissural eruptions that would have generated large basaltic fields, while the sedimentary deposits would have been generated by subsequent erosion of the basalts (Panza, 1994). The deposition of the Bajo Pobre Formation could have had occurred in a rift zone related to the break-up of Gondwanaland and opening of the Atlantic Ocean.

Temporally related with the magmatic episode that generated the Bajo Pobre Formation is a group of hypabyssal porphyritic andesites that intrudes El Tranquilo, Bajo Pobre and Roca Blanca Formations and that is covered unconformably by the Bahía Laura Group. Panza (1982) used the name Cerro Leon Formation for these hypabyssal porphyritic andesites.

During Middle and Upper Jurassic, a pyroclastic volcanic-sedimentary complex of acid to mesosilicic composition was deposited; this was called Bahía Laura Group (Feruglio, 1949; Lesta and Ferello, 1972). These Jurassic rocks form more than half of the Deseado Massif area. The Bahía Laura Group is mainly rhyolitic and sometimes dacitic in composition. It is composed by the Chon Aike Formation (Archangelsky, 1967), which is formed mainly by pyroclastic and lava flows, and by the La Matilde Formation (Archangelsky, 1967; Stipanovic and Reig, 1956), which is formed by volcanoclastic and sedimentary intercalations. The acid to mesosilicic magmatism that produced the Bahía Laura Group was interpreted as to be due to deep level anatexis of the lower crust (Pankhurst and Rapela, 1995). Schalamuk et al. (1999) proposed a period of volcanism of about 50 Ma for the Bahía Laura Group, having radiometric ages between 177-125 Ma. However, the age of Bahía Laura Group in relation to the Bajo Pobre Formation has been controversial because radiometric dating gave similar ages for both volcanic events. In 1999, (Feraud et al.) proposed a migration of the age of the Jurassic volcanism in the area from east (around 178 Ma) to west (about 144 Ma), which could explain the presence of same ages for the two different volcanic events and allows the Bajo Pobre Formation to be older than Bahía Laura Group

The Chon Aike Formation is composed of a thick sequence of ignimbrites of rhyolitic to rhyodacitic composition, with subordinate agglomerates and volcanic breccias, and scarce tuffs and rhyolitic lava domes (Panza, 1994). The individual ignimbrite layers are compact and usually of 5 to 15 m thickness but that can sometimes reach 30 m. The thickness of Chon Aike is difficult to determine and very variable because it is limited by upper and lower erosional boundaries (Panza, 1982). In the Tres Cerros geological sheet, the thickness varies between 200 and 600 m (Panza, 1994); however, it can reach 1200 m (Sanders, 2000). The Chon Aike Formation is intercalated with La Matilde Formation but stratigraphic relationships are not very well understood because of rapid lateral changes in facies and thickness in the volcanic pile (de Barrio et al., 1986).

La Matilde Formation includes mainly tuffs and volcanoclastic-sedimentary rocks with intercalations of thin ignimbrite layers (Panza, 1994). The dominant tuffs are generally fine grained or slightly sandy, they are glassy or crystalline, and usually compact. The thickness of this Formation is also difficult to determine, but Panza (1994) inferred a maximum thickness of 150 m for parts of the area. This Formation represents a continental fluvial and sometimes lagoonal environment developed at the same time of an intense volcanic activity in distal areas.

During the last part of the Jurassic (Kimmeridgian-Tithonian) and the Cretaceous time, some continental sediments were deposited as Bajo Grande (Di Persia, 1956) and Baqueró (Archangelsky, 1963) Formations. The Bajo Grande Formation of Upper Jurassic to Lower Cretaceous age consists of a continental sequence of sandstones, conglomerates and pyroclastic materials, and scarce intercalated shales and limestones. The Formation's thickness is variable between 80 and 350 m (Panza and Marín, 1998). These deposits lie unconformably over the Chon Aike Formation (de Barrio et al., 1986). The lower portions of the Bajo Grande Formation, mainly composed of sandstones and tuffites with scarce conglomerates, were deposited in a fluvial environment. The upper portion consists of a sequence of fine-grained tuffs and some intercalated tuffites (Panza, 1994). The deposition of this Formation marks a continued subsidence of new Jurassic depocenters in the Deseado Massif (Sanders, 2000).

The Baqueró Formation, of lower Cretaceous age, has a thickness of 100 to 140 m and is composed by two Members. The lower Member consists of conglomerates, sandstones, siltstones, and shales. The Upper Member, which is more widespread, is composed by a sequence of rhythmically intercalated cinerites and tuffs. This Formation lies on an angular unconformity over the Bajo Grande Formation. The depositional environment of the lower member of Baqueró Formation is fluvial and sometimes lagoonal, while the upper member indicates sedimentation during almost continuous fall of ash derived from a distal volcanic area (Panza and Marín, 1998).

These Cretaceous sediments were partially covered in turn by Upper Cretaceous basalts and the Sarmiento Formation (Feruglio, 1949). After these, subaqueous sediments of Patagonia Formation of Upper Oligocene age were deposited. During the Miocene, continental sediments of the Santa Cruz Formation were deposited, and lately covered by large Mio-Pliocene basaltic lava flows.

2.3. Structural geology of the Deseado Massif

Structurally, rigid blocks limited by fractures characterize the Deseado Massif. Movements of these blocks produced gentle folds with limbs dipping less than 20° (Fernández et al., 1996). The folded rocks are mainly those of La Matilde, Bajo Grande, and Baqueró Formations, but sometimes also those of Roca Blanca, and Chon Aike Formations.

According to Coira et al. (1975) the basement was divided in blocks by fractures that were later reactivated by strengths coming from different directions. During the Lower Mesozoic an east-west compression generated a sinistral transcurrent system (Nullo, 1991). This compression was probably produced because of subduction from the west from the Carboniferous-Permian. During the Upper Triassic, the compressive regime changed to a general extensional regime that continued up to the Upper Jurassic or Lower Cretaceous. A series of NNW-SSE direction faults, controlled by basement structures, were developed (Reimer et al., 1996). These faults produced a series of blocks (grabens, half-grabens, and horsts), which are slightly tilted to the east (Fig. 2.2) and in detail have a complex structure formed by transverse faults that segmented the bigger structures (Ramos, 2002).

Two main fracture systems were defined for part of the area by Panza (1982) as the El Tranquilo system, with average principal direction around Azimuth 145° and a conjugated direction around Azimuth 60°; and the Bajo Grande system, with mean principal direction at 116° and a conjugated direction around 35°. However these systems are recognized with slightly different directions in different sectors of the Deseado Massif; they varies from 143° to 160° and from 57° to 65° for the principal and conjugated directions of El Tranquilo system, and from 116° to 130° and 21° to 36° for the principal and conjugated directions of Bajo Grande system. In some areas these variations produce overlapping of the principal directions of both systems, what makes them difficult to differentiate. The age of these systems is not precisely established (Fernández et al., 1996), but it is known that the Bajo Grande system is subsequent to El Tranquilo system, and that the Bajo Grande system formed

prior to the deposition of Baqueró Formation (Panza, 1982). However, in some cases these fractures have been reactivated probably by movements after the Oligocene (Panza, 1994).

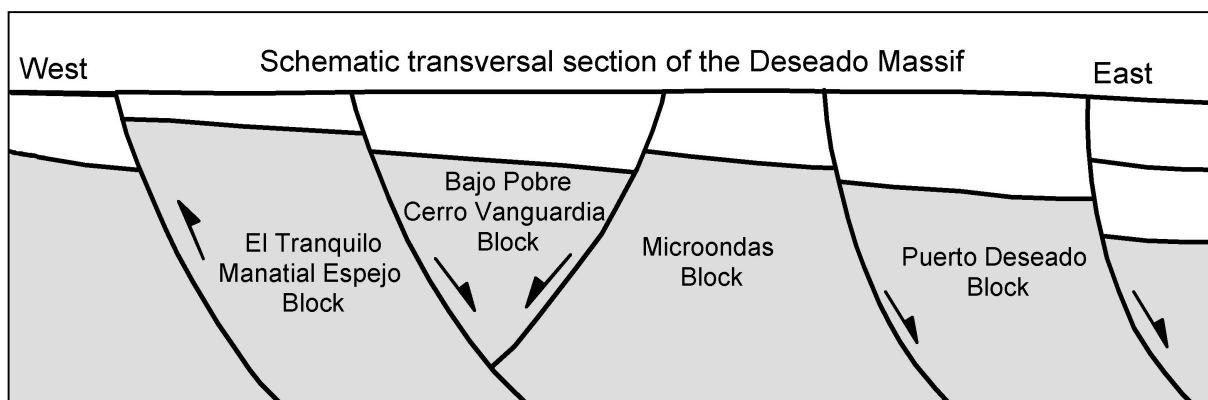


Figure 2.2: Schematic section of the Deseado Massif. The area is divided into blocks by NNW-SSE regional fault systems. And the blocks are slightly tilted to the east (modified from Ramos, 2002).

Their characteristics of both systems are not very well defined but it has been interpreted that the principal direction of El Tranquilo system was produced by sinistral movement and its conjugated by dextral movement. The principal direction of the Bajo Grande system shows also sinistral movement and its conjugated, dextral movement (Panza, 1994). Considering the bisector between both conjugated directions of El Tranquilo system, the strengths that reactivated the fractures for these system might have came from the west, while for the Bajo Grande system the strengths that reactivated the fractures probably came from the WSW (Panza, 1994). However, other authors interpreted slightly different directions of strength; (Fernández et al., 1996) considered that the strengths during generation of El Tranquilo system came from the WNW (between N80W and N60W), and latter they would have shifted to the SW generating the Bajo Grande system.

During some times in the geological history of the area such as in the upper Jurassic, the main directions of both systems acted as areas of stress release, controlling the formation of quartz veins (Panza, 1994; Panza and Marín, 1998).

A third system has been defined for some areas mainly in the area of Río Pinturas in the north of the Deseado Massif. It was called Río Pinturas system (de Barrio, 1989) and its main direction is 10° with a conjugated direction around E-W but not very clearly defined. Mykietiuik et al. (2002) recognized this system in La Esperanza area and inferred that the main fields of strength during the generation of that system were coming from the NW. They pointed out also that this direction is present in that area mainly in the sectors with hydrothermal alteration.

Reimer et al. (1996) pointed out that from Upper Jurassic to Lower Cretaceous three compressive events with strengths from different directions (varying from N15°E to N45°W) occurred. The original normal faults were therefore inverted during different compressive events. Many of the large structures described in the geological maps are inverse faults formed in this way.

2.4. Regional tectonic evolution of the Deseado Massif

The Extra-Andean Argentinian Patagonia is composed of two persistent positive physiographic features: the Somuncura Massif in the north and the Deseado Massif in the south. Both massifs are mainly composed by Mesozoic volcanic rocks generated by volcanic activity produced during crustal extension prior and during the opening of the Atlantic Ocean. They are separated by post Jurassic basins that extent eastwards in the Atlantic Ocean (Fig. 2.3). The tectonic evolution of the area is still

not completely understood, but different explanations have been proposed and are summarized in the following subsections.

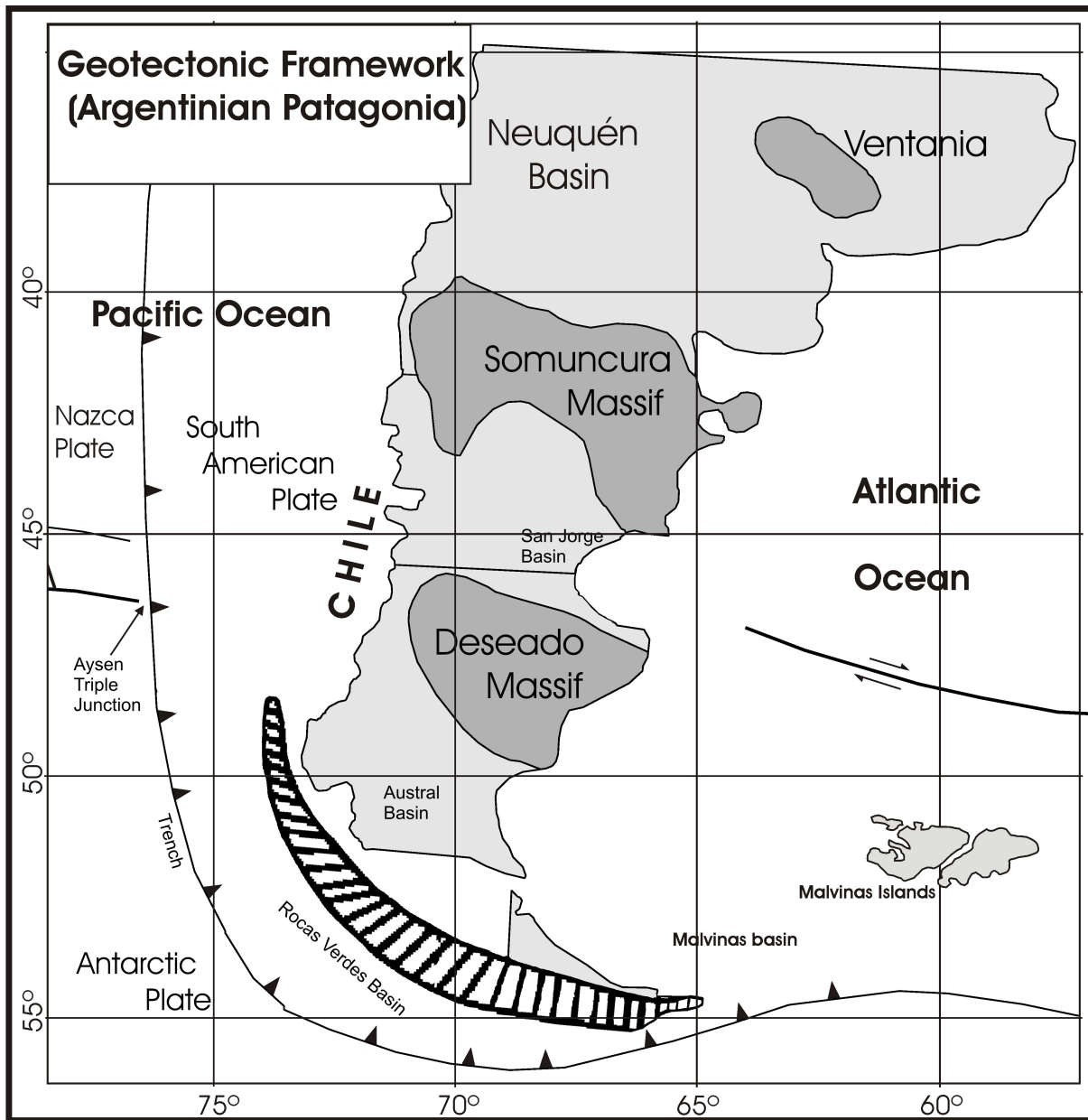


Figure 2.3: Geotectonic framework of the Argentinian Patagonia.

2.4.1. Tectonic evolution of the basement

There are two alternative explanations for the tectonic evolution of the metamorphic basement, which is composed by La Modesta Formation and associated intrusives (Ramos, 2002). One explanation accepts the Patagonian metamorphic basement as part of the Gondwanaland. This hypothesis considered that the Somuncura and Deseado massifs were part of the southwestern border of that continent (Caminos et al., 1988; Forsythe, 1982; Uliana et al., 1985). This explanation is weak because it does not consider the Early Paleozoic magmatism of the Deseado Massif, which consists of 470-400 Ma tonalites and granitic rocks intruding La Modesta Formation, and that corresponds to an active margin.

Other explanation, proposed initially by Frutos y Tobas (1975), considers the Deseado Massif basement as an allochthonous terrain, a micro-plate independent from the rest of Patagonia. The presence of a northwest-southeast trending and southwest dipping subduction zone was proposed for the Lower Paleozoic between the Somuncura Massif and the Deseado Massif. This hypothesis is partially confirmed by the asymmetry of the rift basins that were later developed on the hanging wall of the proposed suture during the Permian and the Jurassic (Ramos, 2002). The granitic and tonalitic intrusions in the Deseado Massif can be interpreted as part of the magmatic arc, and the strong deformation would have taken place during the subsequent collision (Ramos, 2002).

2.4.2. Tectonic evolution during the Gondwanic cycle

Three different hypotheses have been proposed to explain the Gondwanic Cycle (Ramos, 2002). One hypothesis (Forsythe, 1982) proposes a subduction zone in the Pacific margin and a large magmatic arc that occupied Patagonia and some extension to the north of it. This model does not explain satisfactorily the deformation in the Cape system in South Africa and in Ventania (north of Somuncura), which shows strong northeast-vergent folding with intensity diminishing towards that direction.

Another hypothesis, by Lock (1980) and modified by Dalziel et al. (2000), proposes a trench located to the south of Tierra del Fuego and corresponding to a horizontal subduction combined with a hot spot located below the Somuncura Massif. This hypothesis explains the Permian deformation in Ventania as a cause of a horizontal subduction, and the intense Permian plutonic activity in Somuncura as caused by the presence of the hot spot. The intense thermal anomaly would have been responsible for the triple point that produced the break up of the western Gondwanaland and explains the subsequent development of the intense volcanism during the Jurassic in the Deseado Massif. However, available datings in the Somuncura area indicate Carboniferous and Permian ages for rocks with different geochemical characteristics that cannot be explained by the hot spot (Ramos, 2002).

The third hypothesis was presented initially by Ramos (1984) for South America and by Winter (1984) for South Africa, and subsequently modified by Palma (1989). They considered Patagonia as an independent terrain formed by agglutination of the Somuncura, Deseado and probably western Antarctica terrains (called "Austral" continent) that would have collided against the western flank of the Gondwana continent during the Lower Permian. The subduction zone between the Gondwana continent and Patagonia would have been inclined to the south, and the magmatic arc would have been located to the north of the Somuncura Massif. During the collision, the Ventania system and the Somuncura massif would have suffered intense deformation. In the Deseado Massif this events would have produced extension with rifting processes on the hanging wall of the Early Paleozoic suture. Basins formed during this extension would have hosted the sediments that compose the Permian La Golondrina and La Juanita Formations. At the same time, the western Patagonia could have already been subjected to subduction and development of a Carbonic-Permian magmatic arc.

2.4.3. Tectonic evolution during the break up of Gondwanaland

After the Gondwanic orogeny and a thermal subsidence period that controlled the deposition of El Tranquilo Formation, a general extensional process was established. This was a consequence of the extension initiated during Permian, and begun in Northern Patagonia during the Triassic and continued in the Deseado Massif during Lower to Middle Jurassic. This extension produced initially the rocks of Bajo Pobre Formation, and subsequently the predominant rhyolitic magmatism of the Bahía Laura Group (Ramos, 2002). This acid magmatism would be intra-plate and independent of the subduction processes (Kay et al., 1989). Geophysical evidences allow these volcanic rocks to be interpreted as syn-extensional (Uliana and Biddle, 1988).

Crustal thinning contemporaneous with the acid magmatism was produced by the development of a series of half-grabens that structured the basement of the Deseado Massif. These large half-grabens are tilted to the east and have a complex structure with transverse faults that segment them (Ramos, 2002). This extensional episode reached its maximum activity during the Aalemiiano-Bajociano (Middle Jurassic, 175-164 Ma). The products of the rhyolitic eruptions filled the half-grabens (Uliana and Biddle, 1988) and changed in the top to sedimentary intercalations typical of synrift, ending with them the Jurassic extensional episode.

During middle Jurassic in the western part of Patagonia, the subduction had already begun. Arc volcanic rocks with ages ranging approximately from 173 to 145 Ma were emplaced in the Patagonian Cordillera during an extensional regime controlled by normal faulting. This shows that during Jurassic, most of the Southern Patagonia suffered extensional events that precluded the opening of the Atlantic Ocean (Uliana and Biddle, 1988).

The migration towards WSW of the age of the Jurassic volcanism was in the opposite direction to the one expected during the break up of a continent. This was explained by (Feraud et al., 1999), arguing that the migration was probably due to variations in the physical characteristics of the subduction. Those variations that could either have been slowing of subduction rates or steepening of the oceanic subducted plate, would have produced propagation of the extensional regime towards the WSW, which ended in the opening of the back arc Rocas Verdes-Sarmiento basin located at present in the south west of Patagonia (Fig. 2.3). In addition, a spreading of the thermal effect of the Karoo-Antarctica-Tasmanian plume could have had helped the volcanism migration and could explain the unusual large volume of magma generated in the Patagonian area.

During deposition of the Bajo Grande Formation (Upper Jurassic-Lower Cretaceous), the clockwise rotation of the South American continent prior to the opening of the South Atlantic Ocean was accommodated by a system of dextral transcurrent faults with E-W (or ESE-WNW) directions, which crossed the Deseado Massif and overprinted the old rift fractures. These movements had a component of strong compression that formed negative and positive transpressional structures and would have promoted graben inversion, block movements and local tilting of the Jurassic ash flow tuffs (Sanders, 2000) and even of the Bajo Grande Formation. Sanders (2000) proposed that during Bajo Grande time in some sectors the tuffs were deposited while in adjacent areas, resurgent doming in calderas and doming eruptions, tilting and gold-silver veins deposition in geothermal fields along regional strike-slip faults were produced.

The Deseado Massif shows extensional reactivations during the Aptian (Early Cretaceous) that produced the eruptions of pyroclastic flows of the Baquero Formation that overlies on an angular unconformity with the eo-Cretaceous and Jurassic rocks (de Barrio et al., 2000; Hechem and Homoc, 1987). The extensions ceased at the end of the Lower Cretaceous when the South Atlantic Ocean basin opened, and the Deseado Massif became a positive feature, which persisted throughout the Cretaceous and Tertiary periods while mayor sedimentary basins formed to the north and south (Sanders, 2000).

2.5. Epithermal gold mineralization in the Deseado Massif

Starting in the 1990's, several companies have carried out exploration works in the Deseado Massif and they found out that Au anomalies are widespread all over the area. This was highly encouraging, however just two deposits are being exploited today, the Cerro Vanguardia Au-Ag deposit and the Mina Marta Ag-Au deposit. In the meantime, other anomalous zones are being explored and some are in an advanced stage of exploration.

Considering its geological and metallogenic characteristics, the Deseado Massif can be considered as a differentiated Au-Ag Mesozoic province with epithermal mineralizing events related to post volcanic episodes (Schalamuk et al., 2002). The characteristics of more than 30 known Au-Ag

deposits and mineral occurrences indicate them to be low-sulfidation epithermal deposits. The deposits are principally vein type and characterized predominantly by quartz veins and in less proportions by stockworks, breccias and disseminations. The vein infilling has occurred usually in multi-episodic way.

The epithermal mineralizations in the Deseado Massif are associated spatially and temporally to the Jurassic volcanism (Schalamuk et al., 2002). The spatial association is confirmed by field data; Chon Aike Formation constitutes the more frequent host rock (Table 2.1), but Bajo Pobre Formation and sometimes La Golondrina, La Leona, Roca Blanca and La Matilde Formations also host some mineralized veins (Schalamuk et al., 1997).

The temporal association seems to be confirmed by radiometric dating obtained from alteration minerals in some of the Au-Ag-bearing quartz veins of the Deseado Massif. Minerals from Cerro Vanguardia deposit were dated by K/Ar method obtaining ages of 151 ± 3.5 Ma and 152 ± 3.6 Ma (Arribas et al., 1996) for illitic materials, and an age of 138.5 ± 3.3 Ma for some altered adularias. In Manatial Espejo deposit, adularias dated by K/Ar method, gave two different ages, of 142.6 ± 3.5 Ma and 124.8 ± 3.0 Ma. This disagreement of ages may imply that the younger age may be due to post-mineralization alteration processes, and therefore, it has to be interpreted cautiously. Some adularias were also dated by Ar/Ar method and yielded 134 ± 5 Ma for Manatial Espejo, 157 ± 1.5 Ma for Cerro Vanguardia, and 167.9 ± 1.71 Ma for the Martinetas deposit (eastern part of the Deseado Massif). These different ages of adularias have to be considered minimum ages due to the possible re-setting of Argon in the adularia after mineralization (Schalamuk et al., 2002). The age of mineralization in the eastern part of the Deseado Massif is believed to be older than those in the western part (Sanders, 2000). The datings presented above and some ages of 113-114 Ma obtained in quartz veins of the Fachinal deposit (Chile) by the Ar/Ar and K/Ar methods (Townley et al., 2000), could support this idea; however, more dating is needed to confirm this hypothesis

Table 2.1: Approximate area of Pre-Bajo Grande Units outcropping in the Deseado Massif and percentage of a total of 29 deposits that is hosted by each unit.

Pre-Cretaceous Units	Area (km ²)	Percentage of each Unit	Approximate % of Contained Deposits (total=29)
Bahía Laura Group	22786	92.6	76
Bajo Pobre	1165	4.7	14
Roca Blanca	255	1.0	3
La Leona	159	0.6	Remaining 7 % are hosted by some of these formations together with the previous ones.
La Golondrina – La Juanita	162	0.7	
PrePermian	25	0.1	
El Tranquilo	47	0.2	
Cerro Leon	15	0.1	
Total	24613	100	

According to Sanders (2000), mineralization is of Late Jurassic to Early Cretaceous age. During that time, there were crustal extension and high heat flow and geothermal fields were active along dextral, transpressional fault systems (Sanders, 2000). Hydrothermal circulation would have occurred during a regime of very favorable ground preparation, and throughout fractures that could have been either the Lower Mesozoic rift faults or the younger Mesozoic normal and dextral transpressive faults with directions closer to E-W. Local stress fields would have determined which of all the possible structural directions was under tension at the time of fluid flow and generation of quartz veins. In La Josefina area, mineralization occurred mainly in fractures with 160° azimuth (El Tranquilo system) and also in the interval 0° to 30° (Fernández et al., 1996). In the Cerro Vanguardia deposit area, the dominant directions of quartz veins are from 115° to 125°

Mainly native gold, electrum, native silver, argentite, and variable amounts of pyrargirite, freibergite, petzite and other sulfosalts compose the ore in most deposits. Sometimes the precious metals are associated with sulfides such as galena, sphalerite, and chalcopyrite. The gangue consists mainly of different varieties of silica, together with pyrite, arsenopyrite, calcite, barite, adularia, rhodochrosite, siderite and rare monacite. The hydrothermal alteration is represented by dominant silicification and argillization. The latter is characterized by hypogene illite and illite-smectite, and supergene kaolinite. Usually the contact between mineralized zones and host rocks are sharp. Supergene minerals such as limonite, manganese oxides, and scarce alunite and gypsum, have been identified. The deposits are associated with silicified rocks that are weathering resistant and produce topographic highs that are excellent features for prospection for the Au-Ag deposits (Schalamuk et al., 2002).

The presence of several known silica sinters and other paleo-surface indicators, such as the presence of stromatolites, show that in many cases the upper parts of the systems are preserved. The silica sinters are remarkable features for mineral exploration in this area. The different deposits show different erosion levels, from sinter to intermediate Au-Ag-rich veins to deeper base metal-rich bearing veins (Schalamuk et al., 1997).

The gold-silver veins in the Deseado Massif could be genetically related to buried late stage rhyolitic to dacitic intrusives, which promoted local intense hydrothermal activity (Sanders, 2000). Some low-sulfidation deposits in the Deseado Massif are probably related to calderas, which have been proposed as at El Dorado-Monserrat (Echavarría and Etcheverry, 1999), La Josefina (Fernández et al., 1996), and Martinetas-Microondas (Schalamuk et al., 2002). Some large circular features observed in several places such as Cerro Vanguardia, have also been interpreted as calderas (Schalamuk et al., 1997). However, definitive evidences of the presence of calderas have not been found yet. Probably, the age of the volcanic rocks and the several changes (alteration, erosion) they have undergone make it very difficult to recognize unquestionable evidences of the presence of these volcanic features. In addition, the explosive initial volcanism controlled by semi-grabens probably caused the calderas not to have typically rounded shapes (Fernández et al., 1996).

2.6. Discussion

The more accepted hypotheses for the geotectonic evolution of the Deseado Massif are summarized and synthesized as follows:

During the Early Paleozoic, a subduction zone located between Somuncura and Deseado Massifs is proposed. In this context, the rocks of La Modesta Formation (ca. 540 Ma) would have been intruded by tonalites and granites (470 to 400 Ma) during arc magmatism over the subduction zone. Latter both plates would have collided and this would have produced the deformation of the La Modesta Formation and the intrusive rocks.

During Carboniferous-Permian, a subduction and subsequent collision occurred between the Gondwana continent in the north as a subducted plate and an agglomeration of the Somuncura and Deseado Massifs and probably part of Antarctica as the overriding plate in the south. During the same time, rifting produced basins with N-S or NNW-SSE trends in the Deseado massif on the overriding side of the Early Paleozoic suture, and the sediments of La Golondrina Formation were deposited in those basins. After that and during a period of thermal subsidence included in the same general extensional event, the Triassic sediments of El Tranquilo Formation were deposited. During subduction, plutonic rocks were emplaced in the Somuncura Massif. Subsequently during collision the Ventania area and the Somuncura Massif were strongly deformed. Concomitantly, subduction probably occurred in the Patagonian Pacific margin and produced a Carboniferous-Triassic magmatic arc that could have produced the intrusions of La Leona Formation during Triassic.

After the Gondwanic orogeny a general extension occurred. This extension began in the Northern Patagonia during the Triassic, passed to the Deseado Massif during Lower to Middle Jurassic and ended with the opening of the back arc Rocas Verdes-Sarmiento basin in the south west of Patagonia. This extension generated a series of grabens separated by normal faults of NNW-SSE direction and segmented by transversal faults with WSW-ENE direction. At the beginning of the extension, the rocks of Bajo Pobre Formation were deposited. Subsequently, the rhyolitic rocks of Bahía Laura Group were generated filling in the grabens that were being opened. Probably at the waning stages of the rhyolitic volcanism, erosion occurred generating the unconformity that separates the Bahía Laura Group from the rocks of Bajo Grande Formation. However, erosion might have not been very intense because there are several areas with preserved indications of palaeosurface mainly of La Matilde Formation and consisting of silica sinters, and presence of stromatolites.

During Upper Jurassic to Lower Cretaceous, Bajo Grande Formation was deposited marking subsidence and creation of new Jurassic basins. A system of transcurrent dextral faults with E-W or ESE-WNW directions was active in the area and according to the configuration of each fracture zone, local compression or extension was generated. These faults also produced graben inversion, block rotations and tilting of the Jurassic pyroclastic deposits and sometimes of the Cretaceous rocks of Bajo Grande Formation. During the Aptian (Early Cretaceous), extensional reactivations produced the eruptions and generation of ash that was deposited as part of the upper Member of the Baqueró Formation. Finally, at the end of Lower Cretaceous, the extension ceased and the Deseado Massif became a persistent positive area.

Gold-silver mineralizations in the Deseado Massif were produced during Middle and Upper Jurassic and also probably during the very Lower Cretaceous. Knowing the tectonic processes that took place during that time, it is inferred that the quartz veins that host the LSE mineralizations in the area were deposited in an environment ruled by generalized extension represented by grabens and half-grabens limited by NNW-SSE trending normal faults. However, the mineralizations could also have partly occurred during the transcurrent faulting produced immediately after the grabens formation, which is represented by approximately E-W or ESE-WNW fractures. It is still not clear, however, whether the mineralizations occurred just during grabens formation or also during the transcurrent faulting.

Some radiometric datings of gold-silver mineralizations in the Deseado Massif indicate a Middle Jurassic age for the eastern part of the area (Martinetas project), an Upper Jurassic age for the central part (Cerro Vanguardia mine), and Early Cretaceous ages for mineralizations located in Chile (Fachinal mine), slightly to the west of the study area. These ages support the theory of the westward migration of the processes that produced such mineralizations. As LSED are usually formed a short period after the main volcanic activity has ceased, the westward migration of the mineralizing process would be in accordance with the proposed migration of the Jurassic volcanism towards the WSW, from about 178 Ma in the east to about 144 Ma in the west. However, radiometric dates of mineralizations have to be interpreted carefully because the results can be due to post mineralizing alteration of the dated minerals. More dating will have to be done to confirm this theory.

The rocks that host the LSED in the area suggest that the mineralizing events occurred just during or slightly after deposition of the Bahía Laura Group, because there is no indication of mineralization in Bajo Grande or younger Formations. Therefore, disregarding their absolute age, the host rocks of interest in exploration of LSED in the area are those older than Bajo Grande Formation. The rocks that host most deposits are those of the Bahía Laura Group; however, this can be more related to the relative area occupied by those rocks than to the susceptibility of each lithologic formation to host mineralization. Using data presented in Table 2.1, it can be calculated that there are more than three times more deposits per unit area in either the Roca Blanca or Bajo Pobre Formations than in the Bahía Laura Group (Chon Aike and La Matilde Formations together). Therefore, the rocks of Bajo Pobre and Roca Blanca Formations could have been more receptive to be mineralized than those of

the Bahía Laura Group. In addition, some deposits are hosted in two different Formations, one of them is always Chon Aike and the other can be La Golondrina, Bajo Pobre or La Matilde Formations.

Because the characteristics of Au-Ag LSED in the area are very similar, the Deseado Massif is considered a gold-silver metallogenic province. Therefore, it is considered that exploration at province scale can be done over all the area using the same methodology and exploration models. However, when scale is more detailed, local changes may have to be considered in the definition of the model.

2.7. Conclusions

The gold-silver mineralizations in the Deseado Massif are of the low-sulfidation epithermal type and they show enough common characteristics over the area as to develop an exploration model that can be applied for the exploration of LSED in the area. Exploration for LSED in the area should consider the following:

- (1) The rocks of the Bahía Laura Group and probably those of Bajo Pobre Formation are potential host rocks, while rocks younger than the Bahía Laura Group can be rejected as hosts.
- (2) Most of the mineralizations seem to have occurred during a general extensional episode being controlled by NNW-SSE trending fractures (produced during rifting) and probably partially by WNW-ESE transcurrent fault systems. These fracture systems may have acted as hydrothermal fluid pathways. Some of the original NNW-SSE trending fractures may have been slightly rotated by subsequent transcurrent faulting.
- (3) The two main types of hydrothermal alterations related to the mineralizations are: a) silica related alterations, which are very useful indicators of the presence of the LSED in the area, and can appear in the form of veins (quartz, chalcedony or opal), silica sinters or host rock silicification; and b) clay alterations that form small envelopes around veins hosting mineralization and that consist mainly of illite, illite-smectite and some kaolinite.

CHAPTER 3: Conceptual LSED Exploration Model

Mineral deposit models have been defined by (Ludington et al., 1985) as "systematically arranged information that describes the essential attributes of a class of mineral deposit". An exploration model for a certain area and class of deposit can be generated by customizing a general mineral deposit model for the area under study. The exploration model has to include the main general characteristics of the type of deposit being sought. In this chapter, the general characteristics of LSED worldwide are first described; then, the spatial distribution of the most important LSED in the Deseado Massif is analyzed as a means of obtaining patterns that can provide insights into the geological controls on the low-sulfidation epithermal mineralization in the area. Finally, an exploration model customized for the area is described by means of a series of recognition criteria that can be used for mineral potential mapping.

3.1. General characteristics of LSED

Epithermal deposits can be classified in four major types: (1) low-sulfidation; (2) high-sulfidation; (3) intermediate-sulfidation; and (4) deposits related to alkaline magmatism. Low-sulfidation epithermal deposits (also called adularia-sericite, quartz-adularia, low-sulfur, or hot-spring deposits) are those in which sulfur appears in the fluids mainly as reduced species (S^{2-}) in HS^- and H_2S . Low-sulfidation epithermal fluids usually have neutral or near-neutral pH, and have salinities of less than 3 wt% NaCl equivalent. Gold is probably transported as Au^+ , which forms complexes with sulfur (mainly $AuHS(aq)$) so, that loss of H_2S by boiling is the preferred possible mechanism for gold deposition. The temperature of fluids during Au deposition is usually of less than 300°C, but gold can be deposited even at less than 100°C at near surface conditions.

Low-sulfidation epithermal deposits are usually located in two possible tectonic environments: (1) in arcs or back-arcs in subduction-related volcanic areas; (2) or less commonly, in extensional rift-related volcanic areas. The associated volcanism is typically calcalkaline and from acid to mesosilicic compositions, but they can also be related to alkaline magmatism and/or more basic rocks. In many cases, LSED are related to bimodal rift volcanism (Sillitoe, 2002). Their age is variable but typically they are Mesozoic or younger; this could partially be a result of their low preservation potential. The most common regional structural settings for LSED are caldera margins (Hayba et al., 1985); however, other settings are also common. They are strongly structurally controlled and typically occur in tight association with high angle fractures produced by extensional and transtensional stress regimes dominant in volcanic areas.

The host rocks of LSED can be of variable composition, from andesitic to rhyolitic, and any other kind of rock crossed by epithermal fluids, including sedimentary and metamorphic rocks. Ore depositions are produced usually more than 1 My after formation of the host rock (Hayba et al., 1985). The sizes of low-sulfidation deposits are very variable; for example, Comstock lode deposit covers an area of approximately 65 km² while McLaughlin deposit covers an area of less than 1 km² (Cooke and Simmons, 2000). The vertical mineralised intervals typically average about 300 m (Buchanan, 1981); however, they can reach as much as 700 m (Hayba et al., 1985). Their depths of formation can range from surface to up to 1 or 2 km (White and Hedenquist, 1995), but a majority has been deposited between 50 to 700 m below the paleo-water table.

Low-sulfidation deposits usually consist of open space fillings in veins, stockworks or breccias, but in some cases, they can occur as disseminated mineralization in permeable lithologies (Fig. 3.1). The quartz veins show abundant colloform-crustiform textures. Common lattice textures in the accompanying gangue are possible evidences of boiling and therefore encouraging for exploration because of the relationship of boiling with gold deposition. Ore is usually in the form of free electrum

or native gold, but can be disseminated in pyrite or more rarely as tellurides (Cooke and Simmons, 2000). They contain pyrite, pyrrhotite, arsenopyrite, and high-Fe sphalerite. The most conspicuous gangue minerals are quartz (highly predominant), adularia, and calcite. Presence of adularia and sericite (illite-muscovite), and the absence of high sulfidation state minerals as pyrophyllite, alunite, enargite, and luzonite, characterizes these deposits. In addition, the presence of silica sinters on the top of these deposits is clear evidence that they are of low-sulfidation style.

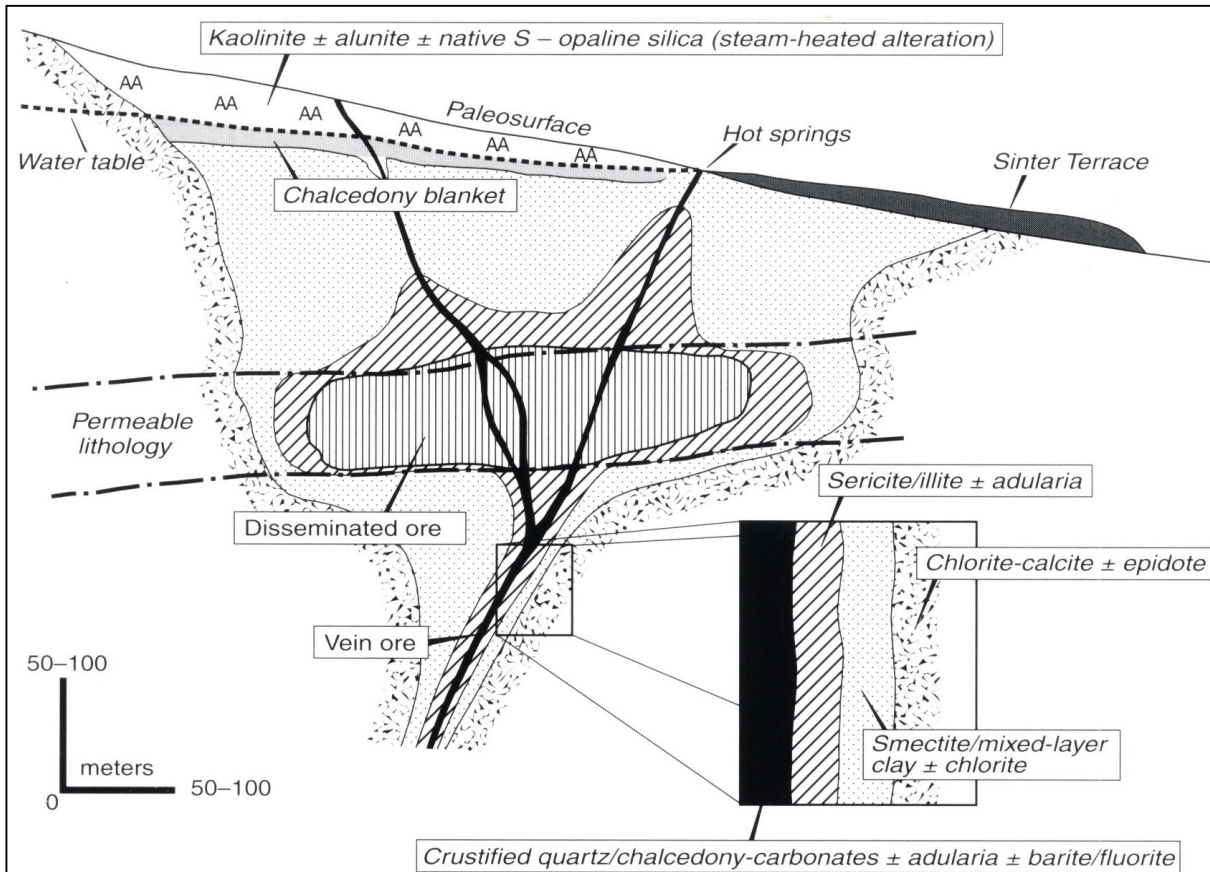


Figure 3.1: Schematic model of a low-sulfidation epithermal system (from Hedenquist et al., 2000).

The wall rock alteration assemblages include quartz, adularia, calcite, illite, chlorite, albite, epidote, zeolite, and pyrite. From the vein salvage into the adjacent country rock, adularia gives way to argillic alteration minerals and quartz abundance diminishes. The argillic alteration minerals are temperature and pH-dependent (Fig. 3.2) and organized around the center of the system, grading from illite close to the ore to illite-smectite to smectite, and finally to propylitic alteration as a bigger envelope around the deposits. Minor kaolinite and alunite can be present in areas of acid alteration generated by steam-heated waters, but they are not spatially related to the ore.

Because of their narrow dimensions, chemical halos of vein deposits are of small extent. The anomalies are well developed in veins and fracture materials because they are samples of the plumbing system, but not so well in the country rock (Govett, 1983). Geochemical studies of some active geothermal systems similar to ancient LSED showed element distributions that allow producing general geochemical models for these deposits (Fig. 3.3). However, variations occur from area to area. Elements that can be anomalously high in LSED and can be used as pathfinders include Au, Ag, As, Sb, Hg, Tl, Se, K, and the base metals Cu, Pb, and Zn (White and Hedenquist, 1995). The usefulness of these pathfinder elements resides in the fact that they form anomalous halos around the ore that are usually of much larger sizes than the halos produced by the ore elements.

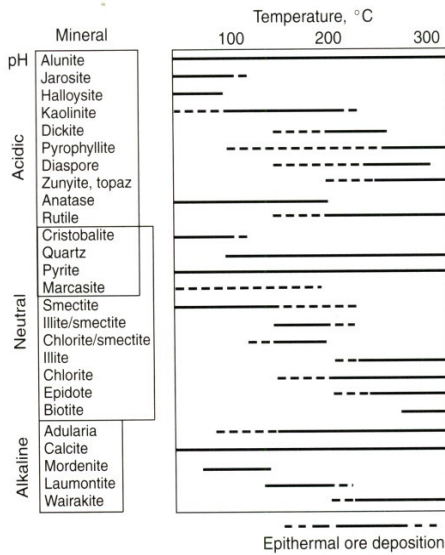


Figure 3.2: Temperature and pH stability of some hydrothermal minerals (from Hedenquist et al., 2000).

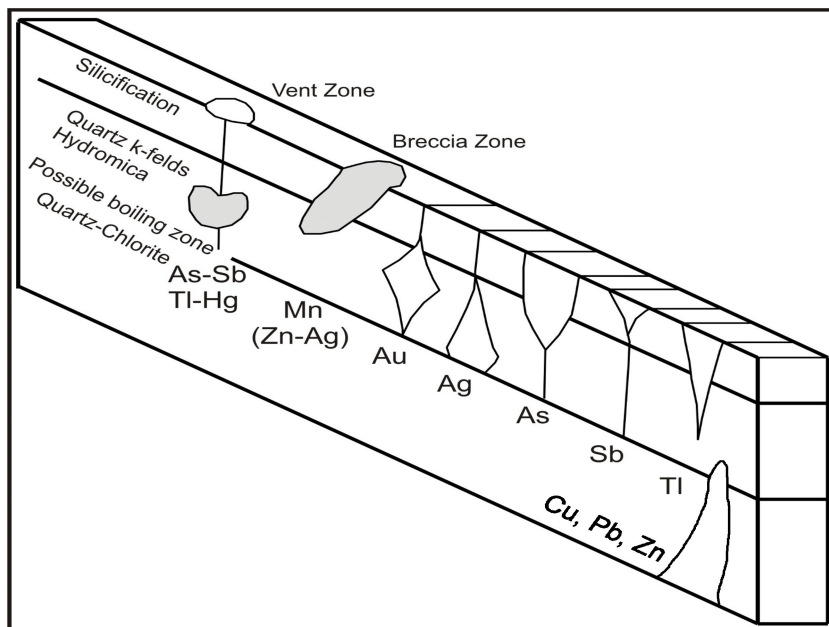


Figure 3.3: Graph showing relative vertical positions of pathfinder metals halos in an ore deposit of low-sulfidation epithermal style (modified from Hoffman, 1986; and Pirajno, 1992).

3.2. General guidelines for exploration of LSED

Unless they crop out at the surface, epithermal deposits of low-sulfidation and high-sulfidation styles are difficult exploration targets because they vary sharply in width and grade (White and Hedenquist, 1995). Moreover, low-sulfidation deposits are usually surrounded by narrow alteration halos in comparison to the broad halos of acid alteration that surround most of the high-sulfidation deposits.

Important aspects to be defined during exploration for epithermal deposits are: (1) the type of epithermal deposits being sought; (2) the level at which the systems are exposed; (3) the nature and location of paleo-conduits; and (4) probable controls on ore deposition and possible shape of orebodies. To define these aspects, the exploration geologist can make use of several tools such as knowledge of the regional geologic setting; lithological and structural mapping; mineralogical studies

of ore, gangue, and host rocks; textural studies; fluid inclusion studies; geochemistry; geophysics; and remote sensing. During the initial assessment of a prospect, the first goal is to determine if the paleo-systems in the area under study were epithermal, and if so, their style, high-sulfidation or low-sulfidation. This is crucial for developing valid models for the prospects being explored (White and Hedenquist, 1995).

The levels of exposure of ancient epithermal systems are critical for determining whether the deposits have potential to still host the Au (and Ag) rich interval of the system or that interval has already been eroded. LSED form at shallow crustal levels (Lindgren, 1922; White and Hedenquist, 1990), so regions that have been deeply eroded have less potential for new discoveries. Erosion and weathering have to be considered because they can mask the ore in places, but can also improve the ore quality through oxidation and can have effects on metal recoveries, improving them considerably. Supergene oxidation has effects over high-sulfidation deposits and disseminated low-sulfidation deposits in regions of arid and semi-arid climate (Hedenquist et al., 2000); however, in low-sulfidation veins, supergene oxidation is usually limited. Another goal during exploration is to detect the paleo-fluid flow channels and then to determine their potentiality as fluid conduits or hosts of mineralized zones (Hedenquist et al., 2000). By knowing their stability temperature fields, alteration minerals can be used for estimate isotherms and so paleo-fluid flow directions that could lead to the area of deposition.

Low-sulfidation deposits have a set of features that help to find them during exploration; some of these features can only be recognized at certain scales, while others can be recognized at a wide range of scales, from regional to district or deposit scale. Features recognized at continental scale are mainly related to tectono-magmatic settings of formation. Features observable at regional to district scales include: association with other types of deposits; host rock alteration; and geochemical, geophysical, lithological, and structural characteristics. Features that can be recognized only at the scale of the deposit include ore and gangue mineralogy and textures; and physicochemical characteristics of fluids trapped in fluid inclusions. The knowledge of the general characteristics of the above mentioned features for LSED together with some distinctive characteristics of the deposits in certain area could lead to the definition of deposit recognition criteria for that particular area.

3.3. Distribution patterns of LSED in the Deseado Massif

The study of spatial distributions of mineralization is an important issue in mineral exploration because it can give an insight about the geological controls responsible for the generation of mineral deposits, and therefore can help to visualize the possible locations of undiscovered deposits. One of the most important controls on the distribution of mineralization in most LSED is represented by fracture systems in which hydrothermal fluids can move and minerals can be deposited. For that reason, determination of structural controls on mineralization was prioritized in this research and the results were used to customize a conceptual exploration model for the area under study. In this subsection, a method called Fry analysis was used for studying the spatial distribution of mineral deposits in order to gain insights into geological controls on the mineralization.

Some people (statisticians, resource analysts, etc) believe that mineral resource evaluation can be achieved by studying the spatial distributions of mineral deposits without any necessary knowledge about the geology of ore deposits (Carlson, 1991). However, when geological controls of mineralization are inferable but not well understood, studying the spatial distribution of known mineral occurrences of interest could reveal patterns that betray controls of their formation. This idea is adopted in this thesis.

3.3.1. Fry analysis

Fry analysis is a point pattern analysis method that uses separations between all objects of an object distribution (Fry, 1979) in contrast to the nearest neighbor methods, such as the Ramsay's method (Ramsay, 1967). In these last ones, considering only separations between nearest neighbor objects could be a great disadvantage because nearest neighbors in undeformed rocks might not always remain so after significant deformation. When deformation is important, some distances between objects became so elongated that some points no longer remain nearest neighbors and therefore are not considered in the analysis. Fry analysis is also an alternative for directional variography studies (Vearncombe and Vearncombe, 1999). Fry analysis and variography both use pairs of data during computation but they diverge due to the algebraic approach in variography versus the geometric approach in Fry analysis. As a further contrast to variography, Fry analysis have several advantages such as using each and every spatial relationship, being a simple method, and not being dependent on mathematical models. In addition, Fry analysis can yield interpretable results even when the amount of deposits is small (Vearncombe and Vearncombe, 1999); which is usually the case in poorly explored areas. For these reasons, this method has been chosen here for the analysis of spatial distribution of LSED in the Deseado Massif.

Fry analysis uses a geometrical method of spatial autocorrelation. The method uses all center-to-center spatial relationships (or translations) between every pair of points. Each center-to-center spatial relationship is plotted as a point in a polar diagram, as a function of direction, having a different data point as center each time, until all points have been used as centers. The resultant graph, initially named "all object separation" plot (Hanna and Fry, 1979), is commonly known as "Fry plot". These plots display the relative position of each point to all other points viewed from a central position. Fry plots can be generated by first marking on a paper all points to be used and a series of parallel references. On a tracing paper also with parallel references, a point to be used as origin is marked. Then that point is placed over each one of the points of the first paper, and each time every remaining point of the first paper are transferred to the second paper. During this process, both paper sheets have to maintain the same orientation (i.e., keeping lines on the tracing paper parallel to the lines on the first paper). For "n" data points there are n^2-n translations or spatial relationships (Vearncombe and Vearncombe, 1999).

Fry analysis was originally developed and is mostly used in strain determinations for studies in structural geology. However, this method and similar ones have been used by some authors for other kinds of studies such as analyzing inter-atomic distances in crystals (Patterson, 1934, 1935; Perutz, 1942) and the distributions of igneous intrusions and orebodies (Allison et al., 1997; de Paor and Simpson, 1987; Lagarde et al., 1990; Leymarie, 1968; Vearncombe and Vearncombe, 1999).

Regional applications of Fry analysis in mineral exploration include the use of known deposits to deduce structural directions that control mineralization. Different geological features or mechanisms can selectively control deposits of different types, grades or sizes that coexist in the same area. These differences can be visualized by analyzing the rose diagrams of Fry plots. Fry plots have also been used to determine directions of continuity in ores, and controls on ore shoots making use of drilling data, such as grade control data in open pits, and ground projection of drilling intercepts with more than certain grade (Vearncombe and Vearncombe, 1999).

When this analysis is used for mineral exploration, its results can be interpreted by looking at the Fry plot, but also by looking at derivative rose diagrams generated from the Fry plots. If there are regular patterns in terms of spacing and orientation of points, the Fry plot will enhance such patterns allowing an easier visual interpretation of them. High frequencies of orientation observed in the plots can reflect orientations of structures that controlled the mineralization. When Fry plots are analyzed, parallel patterns can be separated at a recurrent distance from each other indicating which could be the spacing between the structural corridors with that orientation that are responsible for the pattern.

Controls other than geological can also be determined from the point patterns of a Fry plot, but if there is coincidence between a geological control and the pattern that comes out of the plots, it can be considered that that geological control is the reason for the pattern.

Because of the configurations used in sampling or drilling grids (by systematic grid samplings, excessive local accumulation of points, drilling directions and spacing, etc.) some biases in the patterns occur. These biases can sometimes mask the real controls over mineralization, and therefore is desirable to minimize its effects. To do this, a few techniques can be applied while generating rose diagrams from the Fry plots. One of them is to use ranges of distances when considering the translations to be used in the generation of rose diagrams, therefore including in the graphs just part of the total translations. Other is to use some characteristics such as grade of sample assays, type or tonnage of mineral deposits, etc., that can be used to split the total population of points in some groups with certain geological meaning.

However, these techniques are sometimes not enough for mitigating some biases. In those cases, relative rose diagrams instead of absolute ones, can be used (Vearncombe and Vearncombe, 1999). For applying this method, the percentages of translations that fulfil certain requisite (grade, type, etc) from the total number of translations in each direction (or range of directions) are plotted.

3.3.2. Results of Fry analysis

The Fry analysis for the Deseado Massif area was carried out using 48 Au-Ag low-sulfidation epithermal mineral deposits, each one represented by a point (Fig. 3.4). The deposits under study have different categories of development stage. Four of them are open pits of the Cerro Vanguardia mine, which are located on different gold-silver bearing quartz veins. One is located over the mina Marta-Bacon underground mine, which consists primarily of an extremely silver-rich quartz vein with some gold. The other mineral deposits are either already drilled or indicated by consistent Au or Au-Ag anomalies.

The analysis was carried out with different software for different tasks. Fry plots were generated using DotProc software (from SRK Consulting), which is specialized for Fry and fractal analysis. The DotProc software uses point coordinate data, which can be imported as text files. Point coordinate data of the generated Fry plots were then imported in ILWIS to generate Fry point maps. Directional output data from DotProc were then imported in Rockworks 2002 and plotted in rose diagrams, in which they are shown as percentage frequency of directions for each angular interval of 10°. Some directional diagrams were also generated with DotProc software.

A series of analysis were made to find out whether the 48 deposits are a homogeneous population or if they constitute different groups of deposits depending on lithological association or geographical location in the Deseado Massif, and to reveal some possible controls on mineralization in the area. These analyses consisted of comparisons of five sets of plots generated from five different sets of deposits, that are: 1) the complete set of deposits (48 deposits); 2) deposits hosted in rocks of the Bahía Laura Group; 3) deposits located in the western sector of the area; 4) deposits located in the eastern sector of the area; and 5) deposits located in each one of four different sectors of district scale.

The reason for the first analysis is to infer regional structural controls for all the known deposits in the area without regard to host rock (which is a known lithologic control) and compare this inference with interpretations from the second analysis, which was carried out with deposits hosted by rocks of Bahia Laura Group. The reasons for the third and fourth analyses are as follows. In the Deseado Massif, fracturing, volcanism, and probably the associated mineralizing processes migrated in time towards the WSW direction. This means that mineralization of the area probably occurred along a few million years (likely around 25 My.) as a continuum of events that followed the climax of the migrating volcanism. Therefore, mineralization was produced in different areas, at different moments and probably under slightly different tectonic regimes and stress directions. In addition, the

Deseado Massif is divided in large blocks (grabens, half-grabens and horsts) limited by regional fractures with NNW-SSE trends, perpendicular to the mentioned direction of migration (Fig. 2.2 and 3.8). All these circumstances are likely to have produced differences in the mineralizing controls between areas separated in a WSW-ENE direction. If those differences exist, they could be detected by comparing the mineralizations in the west with those in the east. Thus, the population of deposits was divided in two groups depending on their relative E-W position. One of the groups is composed by 21 deposits located to the east of longitude 69°W, and the other is composed by 38 deposits located to the west of longitude 68°W. An overlapping of 11 deposits (70 km) was intentionally produced between both groups to try to minimize the irregularities in shapes of the sectors, that could produce biases in the analysis, and mainly to have enough points in each sector to obtain a reliable result. For the 5th analysis, four sectors of district size containing no more than 10 points each one were analyzed to test if the dominant directions of the regional scale plots were still recognizable in smaller areas and if so, with which relative strength.

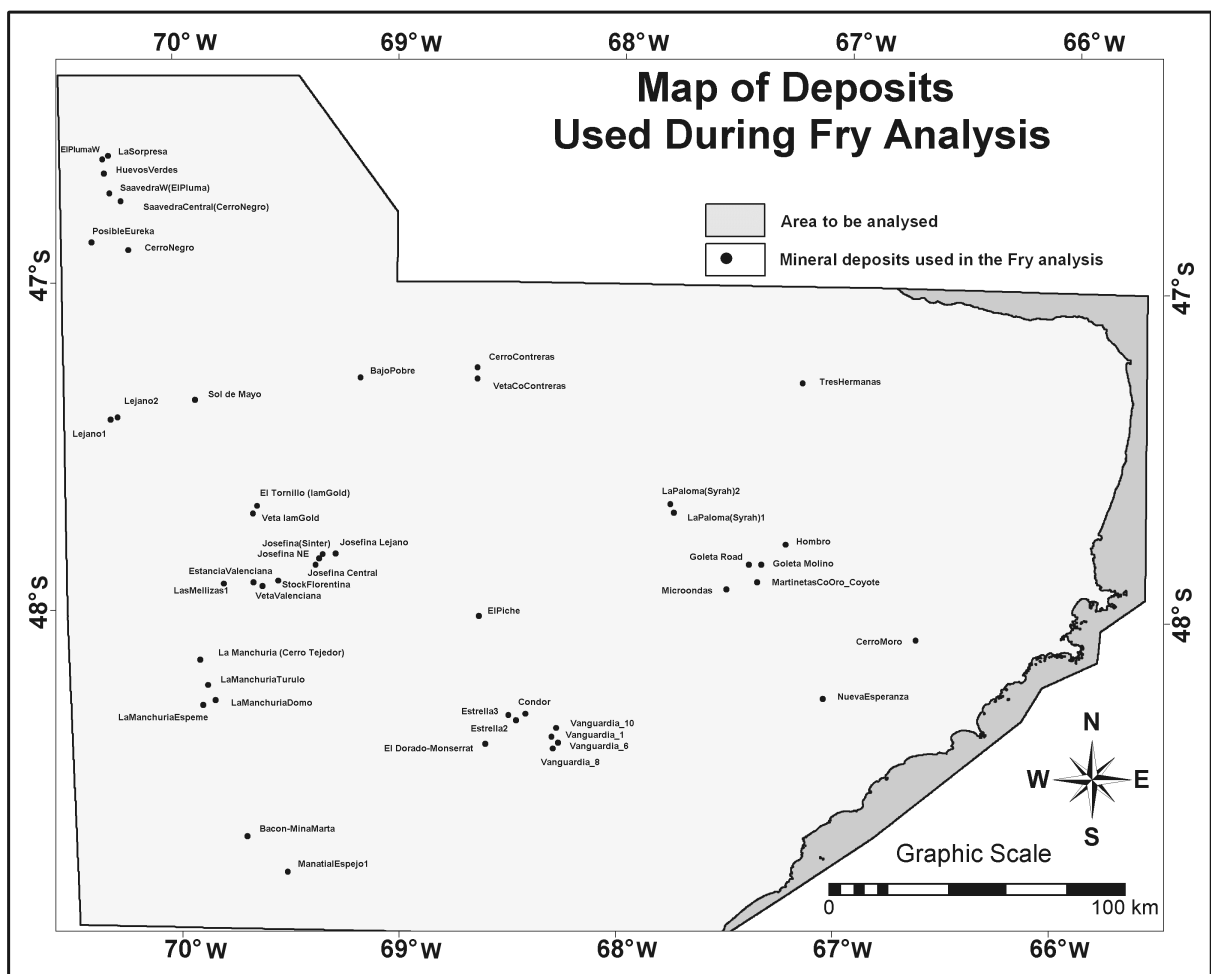


Figure 3.4: Map of study area showing locations of 48 LSED used in the Fry analysis.

In the first analysis, the total population of 48 deposits was used to generate a Fry plot (with 2256 translations) and two derived rose diagrams (Fig. 3.5). In one of the rose diagrams all translations were plotted; in the other, just the translations of less than 100 km length (range = 0-100 km) were plotted. The 100 km range threshold was selected after testing different ranges and realizing that a considerable difference in frequency of some directions between graphs occurred when changing

from a range of 200 to 100 km. In the fry plot and rose diagram with all the translations, a predominant direction with azimuth 120° - 130° and a secondary one with azimuth 160° - 170° are easily observed. Other secondary directions are recognized at 90° - 100° , 140° - 150° , and 50° - 60° in the rose diagram but they are not obvious in the Fry plot. In the rose diagram of translations of less than 100 km, two main directions at 120° - 130° and 50° - 60° , and three secondary directions at 10° - 30° , 80° - 90° , and 160° - 170° were observed. The same prominent directions are recognized in both rose diagrams; however, at short range the 50° - 60° direction is much important than at long range and a new secondary direction at 10° - 30° appears. This indicates that those two directions become more important at local scale, probably due to the presence of subsidiary fractures related to the larger areas of fracturing.

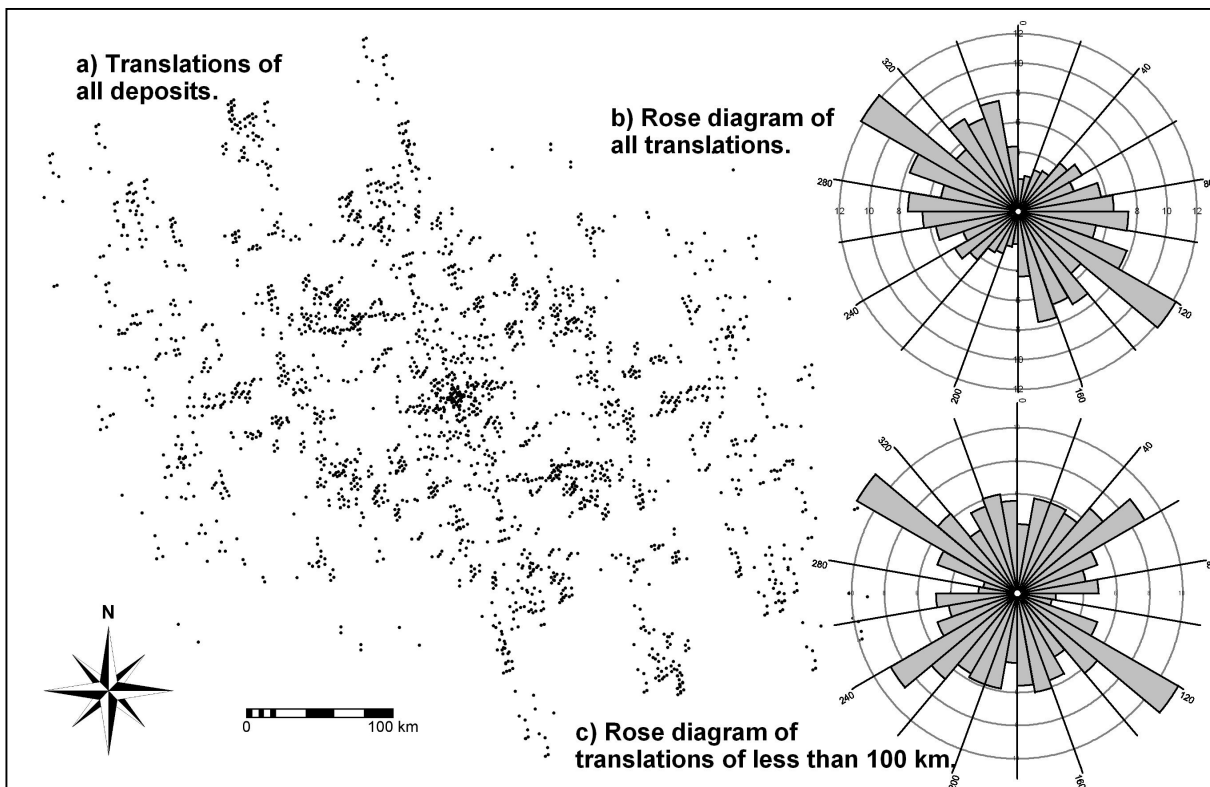


Figure 3.5: Graph generated using all deposits available (48 deposits). **a)** Fry plot with 2256 translations obtained using all the deposits. **b)** Rose diagram of all translations. A predominant direction at 120° - 130° and a less strong one at 160° - 170° are easily recognized in **a)** and **b)**; others at 90° - 100° , at 140° - 150° , and at 50° - 60° can be recognized in the rose diagram but are not obvious in the Fry plot. **c)** Rose diagram of translations of less than 100 km length showing possible enhanced local controls at 50° - 60° .

In the second analysis, only deposits hosted by rocks of the Bahía Laura Group (39 deposits) were extracted from the total population and used to generate a Fry plot with 1482 translations and a derived rose diagram using all those translations (Fig. 3.6). A predominant direction with azimuth 120° - 130° and a secondary one with azimuth 160° - 170° are easily recognized in the Fry plot and rose diagram. Secondary directions at 90° - 100° and 50° - 60° can be recognized in the rose diagram.

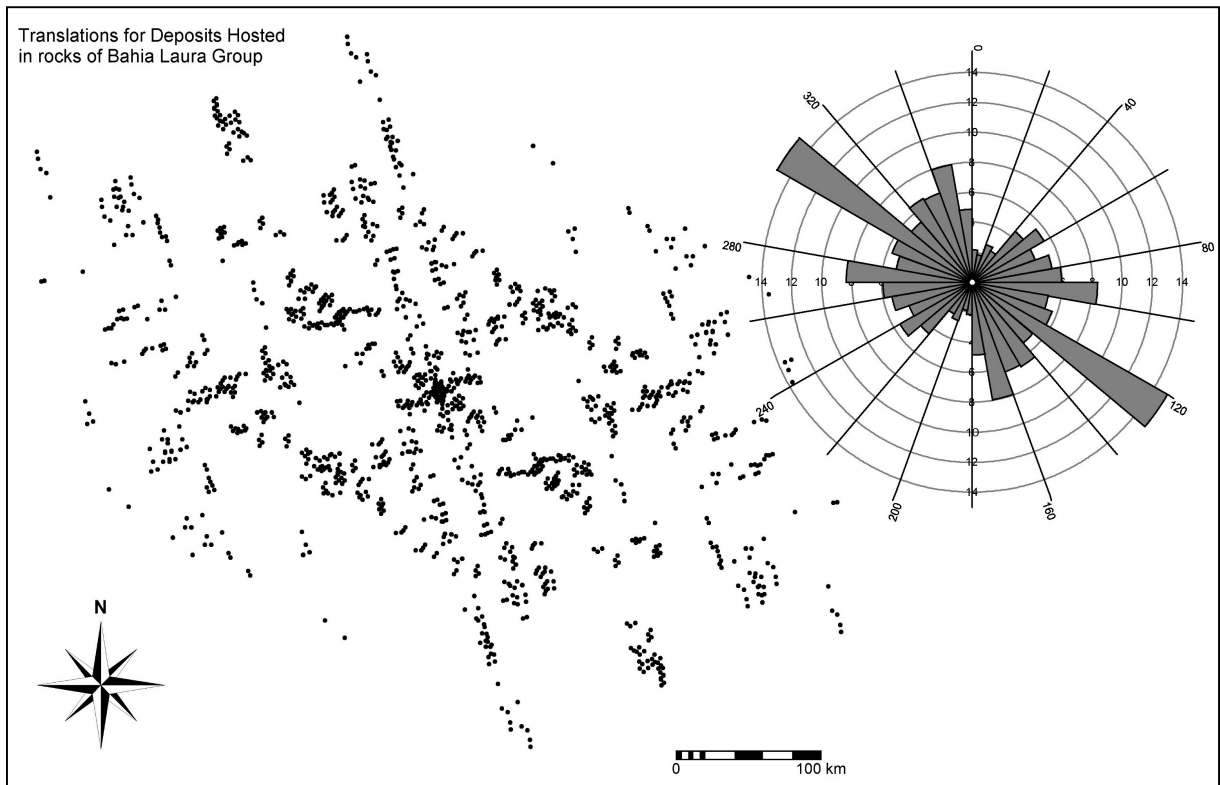


Figure 3.6: Fry plot and its corresponding rose diagram for 39 deposits hosted in Bahía Laura Group.

In the third and fourth analysis, for the western and eastern sectors respectively, rose diagrams with all the translations and with those of less than 100 km length, to try to determine possible local controls, were produced for each sector. Rose diagrams of plots for all translations in the western sector (Fig. 3.7 a, b and c) show three strong anomalous directions with azimuth 120°-130°, 140°-150° and 160°-170°, and two secondary ones with azimuths 40°-50° and 90°-100° were recognized. Diagrams for the short range (less than 100 km) for the western sector also show that the 120°-130° direction is predominant and the 160°-170° direction is important, but other directions that are not frequent in the long range diagram, are enhanced at short range, such as those at 10°-20°, 30°-50°, 70°-90°, and other close to north-south; the direction 140°-150°, frequent in the long range, is not frequent at short range. Both rose diagrams of plots generated for the eastern sector show the same principal directions with similar frequencies. They show in common one predominant direction with azimuth interval of 50°-60°, and two secondary directions at 80°-90° and 120°-130°; the rose diagram for all the points shows in addition a secondary direction at 170°-180°, while the one for range of less than 100 km show a secondary one at 140°-160° (Fig. 3.7 e and f).

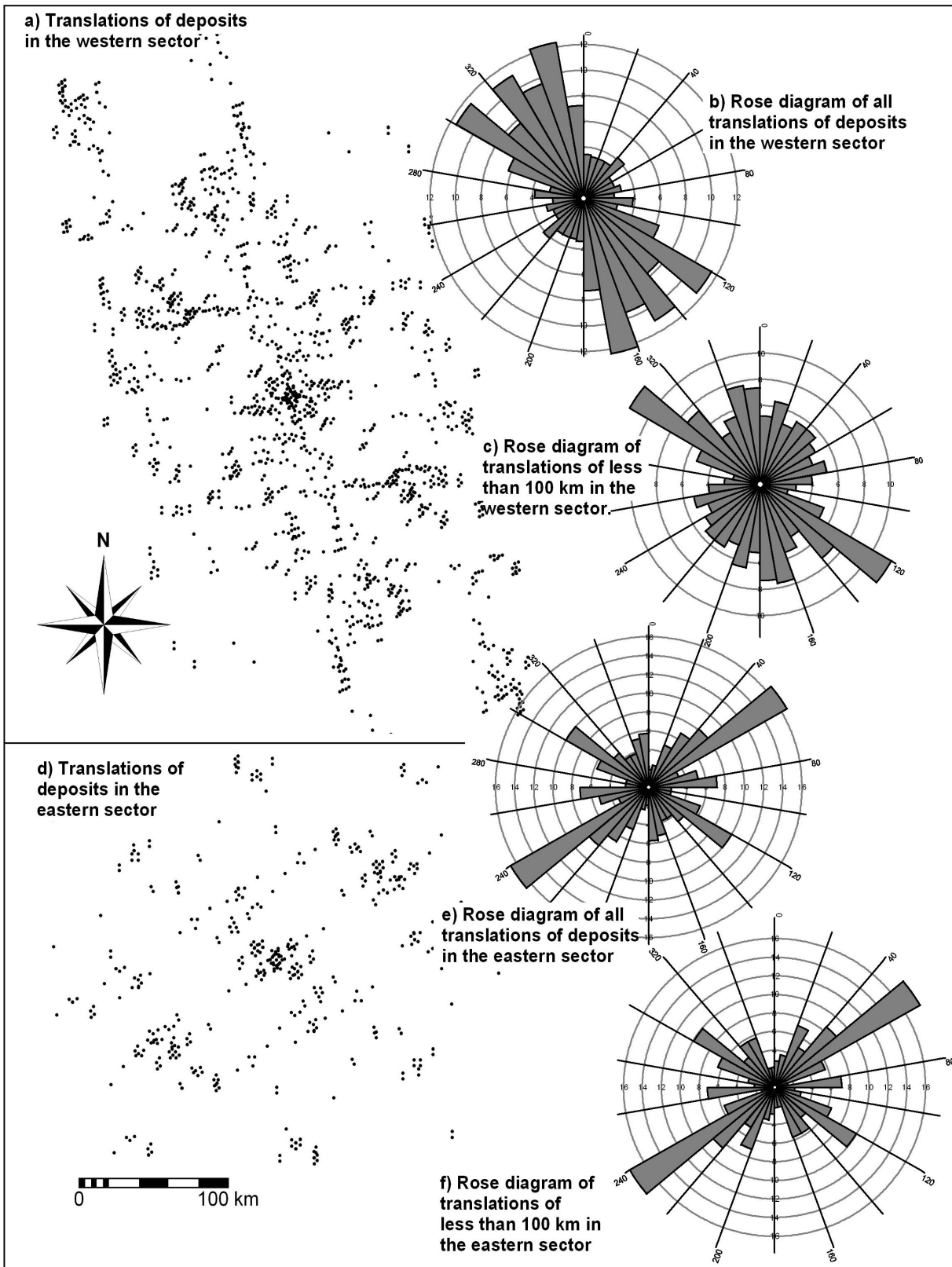


Figure 3.7: Graphs generated with points of the western and eastern sectors. In the west a general NW trend is emphasized, in the east the NE trend is predominant and the NW trends are secondary or absent.

The four sectors studied in the 5th analysis are: Cerro Saavedra, in the NW part of the Deseado Massif; Josefina-Esperanza, in the central-west part of the area; Cerro Vanguardia, in the south-central part; and Martinetas-La Paloma, in the NE of the area (Fig. 3.8). The dominant directions in the directional diagrams are variable but trends around NW-SE are present and predominant in most of the sectors (Figs. 3.8 and 3.9); in three of the sectors SW-NE trends are also well represented. Therefore, because of the small number of deposits used in each sector, the results of the 5th analysis can be considered as suggestive rather than indicative.

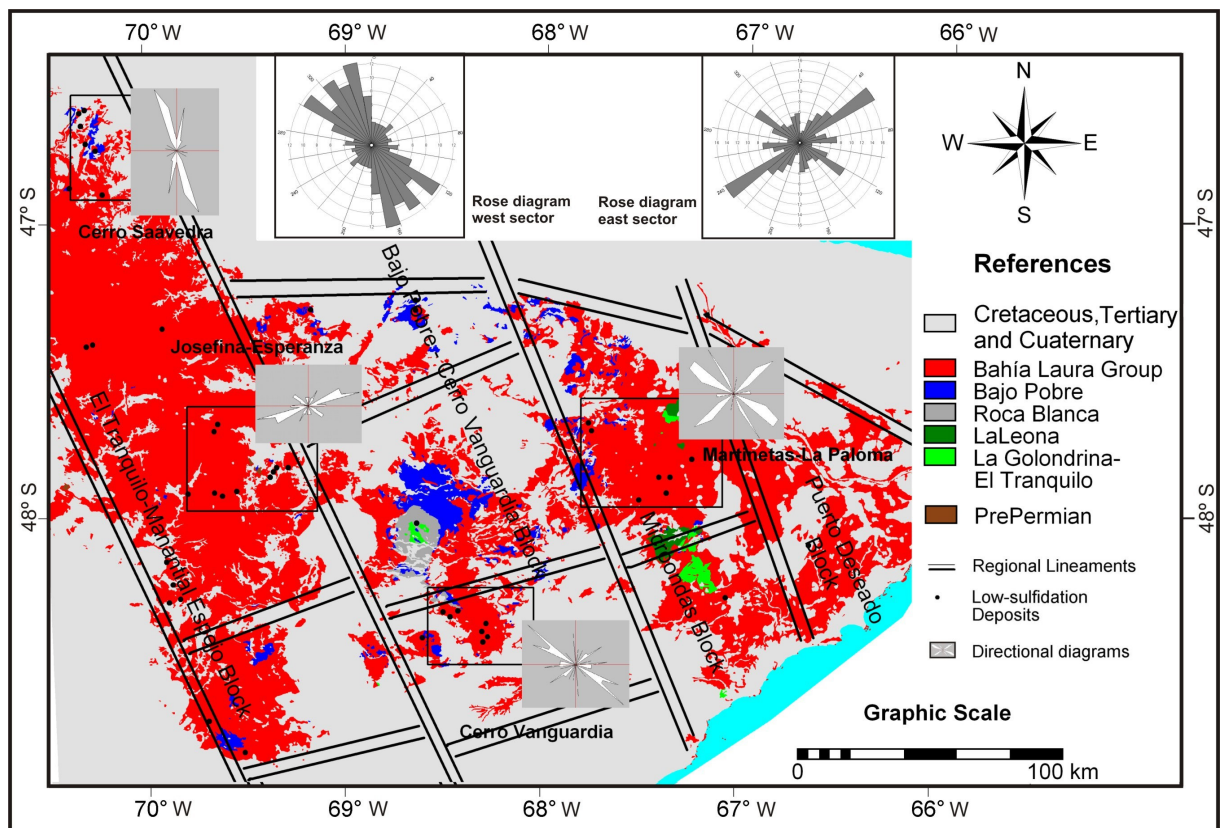


Figure 3.8: Map of the Deseado Massif showing lithology, approximate position of regional scale fractures zones that divide the Deseado Massif in large blocks (Ramos, 2002), rose diagrams for the western and eastern sectors, and directional plots of four district scale areas called Cerro Saavedra, Josefina-Esperanza, Cerro Vanguardia and Martinetas-La Paloma.

3.4. Discussion of results

The Fry plot and derivative rose diagram generated for the total population of deposits (Fig. 3.5) was compared with those generated for the deposits hosted by the Bahía Laura group (Fig. 3.6). In both of them, the same anomalous directions of 120-130° are present with similar frequencies. The separation by lithological unit had thus no important effect on the patterns determined by the Fry analysis. Only translations in the angular interval 160-170° are slightly different, being more frequent in the data derived from the group of deposits hosted by the Bahía Laura's rocks. From this comparison, it is apparent that the mineralizations occurred over the same trends in all mineralized lithologies, and therefore, lithology is not a major control of the spatial distribution of LSED in the Deseado Massif. The explanation for the distribution of the deposits has to be sought after within the structural controls.

Fry plots and rose diagrams of deposits in the western sector and those of deposits in the eastern sector are different (Figs. 3.7 and 3.9, and Table 3.1). In the western sector, NW-SE trends are strongly predominant. In the eastern sector NE-SW directions are predominant while the NW-SE directions are secondary, although the 120-130° trends are clearly indicated. Therefore, it is apparent that structures with NW-SE (mainly 120-130°) provided controls for the mineralization in the western and eastern sectors although controls by SW-NE (mainly 50-60°) trending structures were predominant in the eastern sector.

Table 3.1: Predominant (P) and secondary (S) directions recognized in Fry plots and corresponding rose diagrams generated with different sets of deposits. Range according to a certain length is used to restrict translations plotted in a rose diagram.

Data Used	Figure N°	Deposits	Translations	Range	Angular Interval								
					10°-30°	40°-50°	50°-60°	80°-90°	90°-100°	120°-130°	140°-150°	160°-170°	170°-180°
All deposits all translations	3.5 a, b	48	2257	Total			S		S	P	S	S	
All deposits	3.5 c	48	858	< 100 km	S		P	S		P		S	
Deposits hosted in Bahía Laura	3.6	39	1482	Total			S		S	P		S	
Western Area	3.7 a, b	38	1482	Total		S			S	P	P	P	
Eastern Area	3.7 d,e	21	420	Total			P	S		S			S

For the western area, the main directions indicated by the plots are, in decreasing order of frequency: 160-170°, 120-130° and 140-150°. The first one (160-170°) could represent controls on mineralization by NNW trending regional scale fractures that limit large blocks in the Deseado Massif (showed by Ramos, 2002). The second one (120-130°) corresponds with the range of directions defined for the Bajo Grande system in the Deseado Massif. The third one (140-150°) corresponds well with the general trends of the El Tranquilo system. There are two other observed secondary directions, which could be important because they are observed in the graphs generated by all sets of points. One of them, with direction 40-60° which is prominent in the eastern sector, can be ascribed to the secondary directions of El Tranquilo system; while the other, with direction around 80°-100° could be associated to some normal faults mentioned by Panza (1994) and Panza and Marin (1998). The directional diagrams generated for the eastern and western sectors are suggestive of structural controls on mineralization at regional scale, while the directional diagrams generated for each of four different districts are probably only showing predominant controls on mineralization at district scale.

Due to the fact that most of the known deposits are located in the western sector, and that most of the directions recognized in that sector have been also recognized in the eastern sector, the structural controls suggested by the Fry plot and rose diagram of the deposits located in the western sector could be useful for predicting presence of undiscovered LSED in the Deseado Massif at regional scale. However the 40-60° directions, which are highly enhanced in graphs of the eastern area, suggest that structures with these trends could also be useful in mapping LSED potential in the Deseado Massif at regional scale.

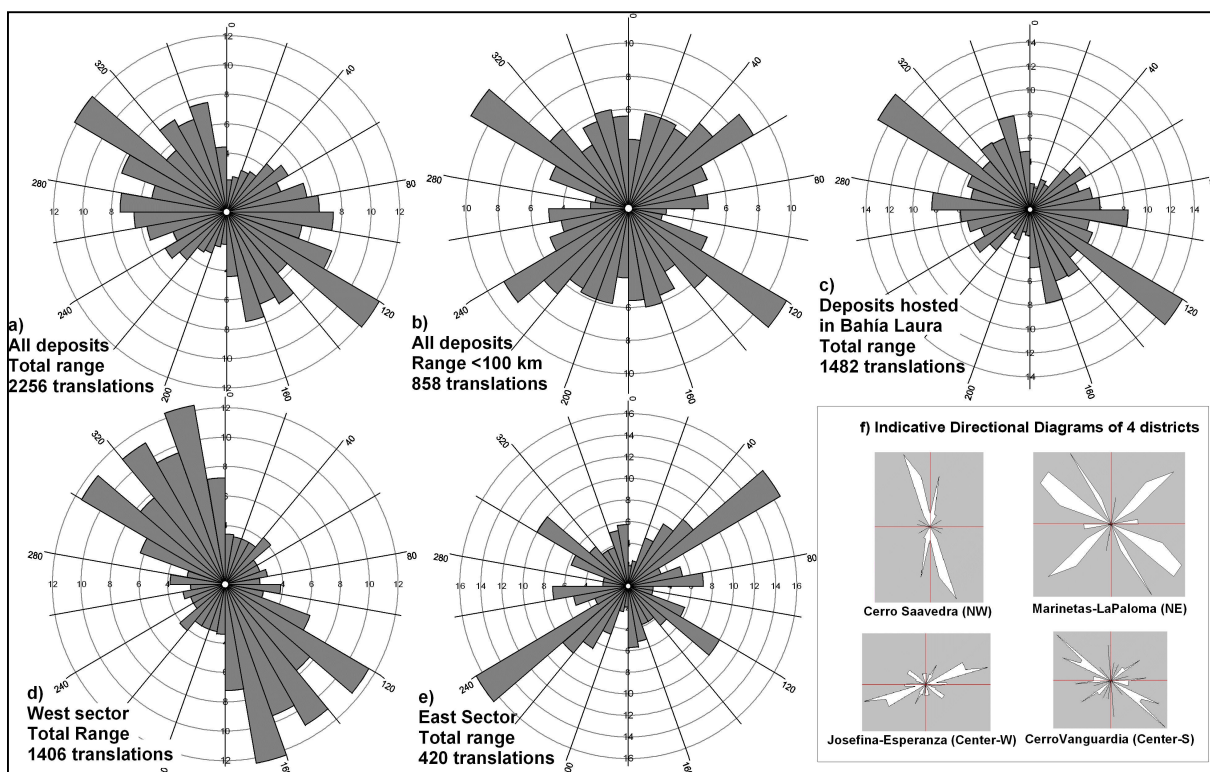


Figure 3.9: Comparison of five rose diagrams generated from four sets of deposits, and of four directional diagrams for deposits in four district scale areas of the Deseado Massif

3.5. LSED recognition criteria

The Deseado Massif has only been explored for a few years (mainly from 1990). Existing exploration and mineral occurrence data are fragmentary, sometimes confidential and mostly extracted from deposits that are not being exploited and so, are not very well understood. Therefore, some deposit recognition criteria not determined here may be proved important in the future when a better knowledge of the mineralization controls get acquired.

The LSED in the Deseado Massif are hosted by Pre-Bajo Grande Formations. Chon Aike is the Formation that hosts most of the deposits followed, in decreasing order of amount of deposits, by La Matilde, Bajo Pobre, Roca Blanca and finally the rest of them (La Golondrina, La Leona and the metamorphic basement). Because the areas covered by the Formations other than Chon Aike are small, even when they host small amount of deposits, they have also good chance to be mineralized in comparison with Chon Aike. Therefore they should also be considered during potential mapping.

Two types of hydrothermal alteration are considered as indicative features clay alteration and silica alteration. Clay alteration minerals in the LSED in the Deseado Massif are mainly illite, illite-smectite and some kaolinite. They are good indicators for these deposits but they form halos of restricted size. A halo of propylitic alteration (mainly disseminated chlorite and pyrite) is also found around the illite, illite-smectite, and silicic zones.

Different types of silica alteration constitute the most conspicuous alteration related to LSED in the Deseado Massif; however, they constitute mostly small zones around the veins. Silicification produces topographic highs that can be visually recognized and are therefore, good indications for prospection in the area. Linear silicified zones are probably the best indicators of the presence of veins, while wide elongated silicified zones can be indicative of stockworks. Silica deposited in the form of sinters has been recognized in several areas and are often associated to Au-Ag deposits such as in Manantial Espejo and La Josefina. Their siliceous nature protects them from erosion so they can

be recognized; but they are usually not very wide. The fact that they indicate the top of the systems is encouraging because mineralized zones could be underneath and/or slightly laterally displaced.

The LSED in the Deseado Massif are vein style and, therefore, strongly structurally controlled. The three most important deposits in the area, Cerro Vanguadia, Manantial Espejo and Bacon-Mina Marta are an example of this; the first of them consists of more than 140 km of quartz veins. From the Fry analysis it was inferred that at regional scale most of the deposits are related to NW-SE structural trends with three predominant directions that seem to have similar importance. However, the direction 120°-130° followed by the one at 160°-170° are probably the most important ones to be considered because they have a geological explanation and they are persistent in every graph. For district scale potential mapping, local controls probably have to be used for each district; they can be extracted from descriptions of the district done by other authors and from the Fry analysis of that district.

Based on the general information about LSED worldwide, and on the results of the Fry analysis, two sets of deposit recognition criteria for exploration of LSED in the Deseado Massif are here defined. The first is applicable for regional scale potential mapping, while the second is applicable for district scale potential mapping. Both sets of criteria consist of lithology, hydrothermal alteration and structure as indicative features. However, for mapping LSED potential at regional and district scale different mappable features were applied as criteria according to the working scale.

The following deposit recognition criteria were selected for regional scale potential mapping.

- (1) Presence of Pre-Bajo Grande Formations.
- (2) Presence of hydrothermal alteration clays.
- (3) Proximity to two sets of regional lineaments.
 - 3.a) Regional faults that separates the Deseado Massif in blocks. Lineaments with azimuths between 145° and 170° were considered in this set to include two sets of orientations pointed out by the Fry analysis.
 - 3.b) Lineaments with directions corresponding to the principal direction of the Bajo Grande system, which is in most of the cases around 116°, but shows some variations depending on the area considered. Lineaments with azimuths between 105° and 125° were considered in this set.

The following deposit recognition criteria were selected for district scale potential mapping.

- 1) Individual lithologic formations that could host mineralization in the selected district.
- 2) Presence of silicic alterations.
- 3) Presence of clay alterations.
- 4) Density of lineaments digitized at 1:100,000 scale.

3.6. Concluding remarks

In this chapter the principal characteristics of LSED worldwide and in the Deseado Massif were compiled and analyzed with the ultimate objective to define the salient deposit recognition criteria for exploration of these kind of deposits in the area at regional and district scales. This was complemented with an exploratory Fry analysis, which was useful for determining the principal structural controls on mineralization in the area. Three general types of deposit recognition criteria for both regional and district scale potential mapping were determined: lithology, hydrothermal alteration and structure. However, different specific types of recognition criteria represented by geological features were used at different scales. The extraction of these geological features is the subject of chapter 4.

CHAPTER 4: Extraction of Geological Features

Lithological, structural and remote sensing data were processed to extract two sets of indicative features, one set for LSED potential mapping at regional scale, the other set for a more detailed LSED potential mapping at district scale. Each of these sets of indicative features includes three geological themes: lithology, structure and hydrothermal alteration. In addition, several known LSED were digitized from different maps.

In this chapter, some general considerations and background of the various methods for geological feature extraction from remote sensing data are briefly discussed. Then, the ways in which regional scale geological features were extracted from the existing datasets are explained in more detail. Finally, the same is done for the extraction of district scale geological features.

4.1. General considerations

Geological maps are useful to focus efforts into prospective ground during exploration. One of the most important factors to consider during the analysis of lithological evidences is the timing of mineralization in relation with the rock age. In hydrothermal deposits, rocks older than or of the same age as the mineralizing events can be crossed by fluids and be mineralized, but younger rocks are not affected and they are therefore, less prospective. In addition, in the case of LSED formation, each lithological unit has different receptivity to mineralization, which is strongly dependent on their permeability. The physical properties constitute an important control of rock permeability and mineralization in LSED. Soft rocks may have high primary permeability, and during deformation they can develop several small fractures and lead to disseminated mineralization. On the other hand, hard rocks, such as those of Chon Aike Formation, are less permeable but brittle, and by deformation they can generate fractures in which veins can form. According to Corbett (2002), only brittle and well-fractured rocks can host veins. In addition, some ore shoots can develop in areas where the rock competency changes, as in the case of the Hishikari deposit in Japan (Izawa et al., 1990). In the Deseado Massif, this situation may occur in the boundaries between the Chon Aike Formation and others (such as Roca Blanca, Bajo Pobre, etc.).

Low-sulfidation epithermal deposits, in some cases grade outward sharply to hydrothermal alteration haloes whose widths depend on the permeability of the host rock (Hedenquist et al., 2000). In the Deseado Massif, clay and silica are the main types of alterations indicative of LSED. Both of them are usually restricted to the veins or up to a few meters away from them. Clay alteration in the area is characterized by illite, smectite, illite-smectite and scarce kaolinite. Each of these clays (and other hydroxyl) minerals exhibits unique absorption features in the short wave infrared (SWIR) part of the electromagnetic spectrum; therefore, SWIR bands of ASTER and Landsat 7 (Table 4.1) can be used to map hydrothermal clay alterations (Fig 4.1). With Landsat 7 data, only a broad group of clay alteration minerals (and alunite) can be recognized because of the limited spectral resolution of this sensor. ASTER data, on the other hand, have higher spectral resolution and in some cases can be used to determine the presence of individual minerals of that group using several spectral mapping techniques.

Silica is not recognizable in visible or near-infrared bands because it has no diagnostic spectral feature in those wavelengths. However, it can be recognized in thermal infrared (TIR) bands (wavelengths between 8 and 14 μm) from multispectral sensors. The spectral emissivity minimum of rocks shift to shorter thermal wavelengths as silica content increases (Sabins, 1999) (Fig. 4.2). Landsat 7 ETM+ data include one thermal band but ASTER data includes five thermal bands, and therefore, the latter is more suitable to map silica alteration.

Table 4.1: Characteristics of Landsat ETM and ASTER bands.

Region of Spectrum	Spatial Resolution	Spectral Range (μm)	ASTER Bands	Landsat Bands	Spectral Range (μm)	Spatial Resolution
VNIR	15 m	0.52-0.60	1	1	0.45-0.52	30 m
		0.63-0.69	2	2	0.52-0.60	
		0.76-0.86	3N (nadir looking)	3	0.63-0.69	
			3b (backward-look)	4	0.76-0.90	15 m
SWIR	30 m	1.60-1.70	4	5	1.55-1.75	30 m
		2.145-2.185	5	7	2.08-2.35	
		2.185-2.225	6			
		2.235-2.285	7			
		2.295-2.365	8			
		2.360-2.430	9			
TIR	90 m	8.125-8.475	10			
		8.475-8.825	11			
		8.925-9.275	12			
		10.25-10.95	13	6	10.40-12.50	60 m
		10.95-11.65	14			

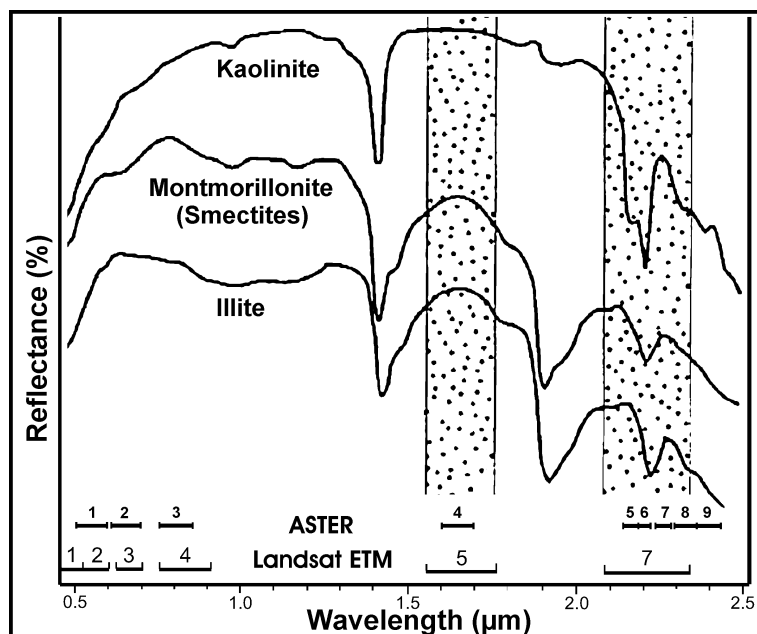


Figure 4.1: Spectra of some alteration minerals showing their characteristic absorptions pikes, and wavelength intervals of Landsat ETM and ASTER bands (modified from Sabins, 1999).

In hydrothermal systems, geological discontinuities and areas of structural weakness are used to transport hydrothermal fluids and tend to localize mineralization. In low-sulfidation epithermal systems, the presence of a fracture or fracturing system is a requisite for transporting fluids to sites of deposition. Mineralization can occur in a disseminated style in permeable rocks, but there always have to be a transporting fracture close to depositional sites. Low-sulfidation ores are usually deposited in sites of stress release where abundant epithermal fluids can flow and minerals can be deposited when sudden pressure reductions result in boiling and destabilization of some components of the fluid solutions. To know the structural patterns and understand the

styles of deformation is therefore important in exploration for epithermal deposits. Direction and length of fractures, presence of fracture intersections, and areas with high fracture density can be used to determine potential exploration targets (Rein and Kaupfmann, 2003).

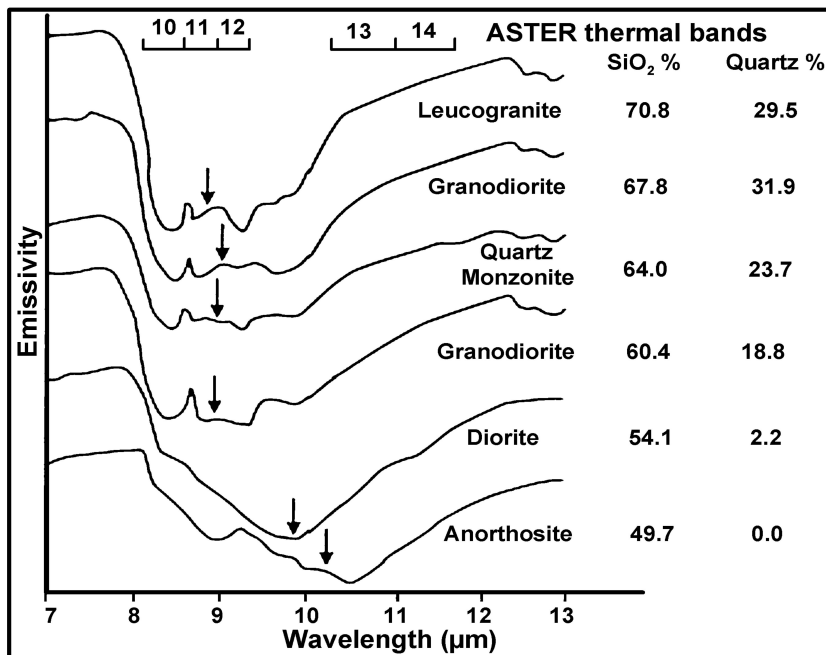


Figure 4.2: Rock emissivity minima in the thermal range of the spectrum and their shifts to shorter wavelengths as silica content increases. Also shown are the ASTER thermal bands (modified from Sabins, 1999).

Regional faults exercise significant controls on epithermal deposits, probably in guiding the emplacement of magmatic heat sources and influencing subsequent hydrothermal activity (Mitchell and Balce, 1990; White and Hedenquist, 1990). Reactivated deep-seated sub-vertical fault zones are also important because they are related to complex fracture arrays, extreme local dilation, and enhanced permeability (Henley and Etheridge, 1995). However, although regional structures control mineralization, mineral deposits are usually not emplaced in such structures but in subsidiary faults that are generated by tension produced by strike-slip movement of the controlling structures (Corbett and Leach, 1998; White and Hedenquist, 1990). Therefore, at a regional scale, only structural zones should be distinguished (White and Hedenquist, 1990). At bigger scales, structural studies have to point out the prospective structures by examining relationships between structure, geochemistry, mineral occurrences, and hydrothermal alteration. At prospect scale, even small structures, bedding planes and joints can be important because they could influence the rock permeability and therefore the location of deposits (White and Hedenquist, 1990).

In this research, the presence of fractures was inferred from the interpretation of lineaments in satellite images, DEMs and derived products. The term “lineament” has been used extensively and with different meanings (Gupta, 1991; Madani, 2001; O’Leary et al., 1976). In this work, straight or somewhat curved features recognized in the images are considered as lineaments, which are likely to represent presence of fractures. Straight valley segments, alignment of vegetation, truncation of outcrops or strata, and straight or slightly curvilinear ridges are suggestive of lineaments.

Lineament maps can be produced from RS images by visual interpretation and manual digitizing or by automatic extraction. Many authors (Budkewitsch et al., 1994; Karnieli et al., 1996; Lepage et al., 2000; Madani, 2001; Vassilas et al., 2002) have automatically extracted lineaments using various methodologies, most of which include edge detection, thresholding, and image classification. The

“GeoAnalyst” module of PCI Geomatica software (from PCI Geomatics) was used during this research for automatic extraction of lineaments from Landsat data in a pilot area. However, the results were not satisfactory; the software did not detect many important lineaments that could be easily recognized by visual analysis and in addition, many lineaments recognized are not likely to have a structural meaning. In view of the poor results obtained by automatic lineament extraction, effort was focused on enhancing Landsat images and DEMs in order to visually interpret and then digitize the lineaments manually.

Different techniques of image enhancement before visual interpretation of lineaments have been widely used by other authors. Some of them applied spatial domain filters for linear edge enhancement, such as the Laplacian high frequency spatial filters and sometimes, directional filters (e.g., Rokos et al., 2000; Suzen and Toprak, 1998). Several Landsat TM RGB color composites such as 721, 741 and 742 were also used (Arlegui and Soriano, 1998; Asadi, 2000; Rein and Kaufmann, 2003); others used PC1 from a principal components analysis that is the principal component that explains most of the topographic information (e.g., Asadi, 2000). In general, features that are parallel to the illumination source are not so easily recognized as those that are perpendicular to it (Lillesand and Kiefer, 2000). Therefore, some authors applied artificial illumination to DEMs by application of several directional filters providing illumination from different directions (e.g. Asadi, 2000; Carranza, 2002). The manifestation of lineaments partly depends of the scale of observation (Gupta, 1991); for this reason, different scales of observation were used during this research to interpret and then digitize the lineaments on the computer monitor.

A few known alteration areas were used every time clay or silica alteration was mapped as a guide to select the best methods and thresholds for the alteration being mapped. One of those areas is La Josefina project that includes small areas of kaolinite alteration, general argillic alteration (smectite and illite) and strongly silicic rocks (silica sinter and opaline bodies). Mining cadastral maps from the Santa Cruz province Mining Direction, a few published maps, and data known by the author were also used for the same purpose and to extract the position of mineral deposits.

4.2. Extraction of regional scale geological features

Regional scale geological features were extracted from different source maps, which were initially georeferenced to zone 2 of the Gauss Kruger coordinate system. The raster maps and Landsat images used in extracting regional scale features have a 30x30 m resolution.

4.2.1. Regional scale lithological features

In the Deseado Massif, the epithermal mineralization is temporally associated with the Jurassic volcanism and, therefore, the Bajo Grande and younger Formations were considered sterile. La Golondrina, La Juanita, El Tranquilo and the Pre-Permian Formations host a minor amount of deposits and account for a minor portion of the total area of the Deseado Massif; therefore, they were considered of low importance in regional potential mapping. Tertiary and Quaternary Formations are not prospective as host rocks but they should be considered when they constitute very thin layers that can mask the presence of underneath deposits hosted in older lithologies.

Seven geological maps at a scale of 1:250,000 produced by the Argentinian Geological and Mining Survey (SEGEMAR), were used to extract the lithological information. They were georeferenced to Gauss Kruger coordinate system using 286 control points recognizable in the maps as well as in well georeferenced Landsat images. The geological maps were screen-digitized using ILWIS 3.1 software and later polygonized and rasterized with a 30 m pixel size. Initially, all the Pre-Bajo Grande Formations were differentiated during digitization and the younger ones were digitized as one undifferentiated unit in view that they could be considered sterile for LSED in this region (Fig

4.3). For the regional scale potential mapping, Chon Aike, La Matilde and Bajo Pobre Formations, totalling around 23,200 km², were extracted from the digitized maps and grouped in a binary map of favorable lithology for LSED occurrence in the region. The rest of the rocks were considered non-favorable (Fig. 4.4).

Important differences are observed in the outlines of the lithologic units in the georeferenced maps when compared with lithologic boundaries recognizable in well georeferenced Landsat images. These differences are difficult to quantify because they change without any pattern within each map. In the georeferenced maps, they can vary from almost zero to up to about 600 m; however, in most cases, the differences do not exceed 300 m. These errors were likely produced by the method of mapping based on air-photographs, which always show distortions. Considering that the scale of the digitized geological maps is small, these differences are negligible in regional scale mapping.

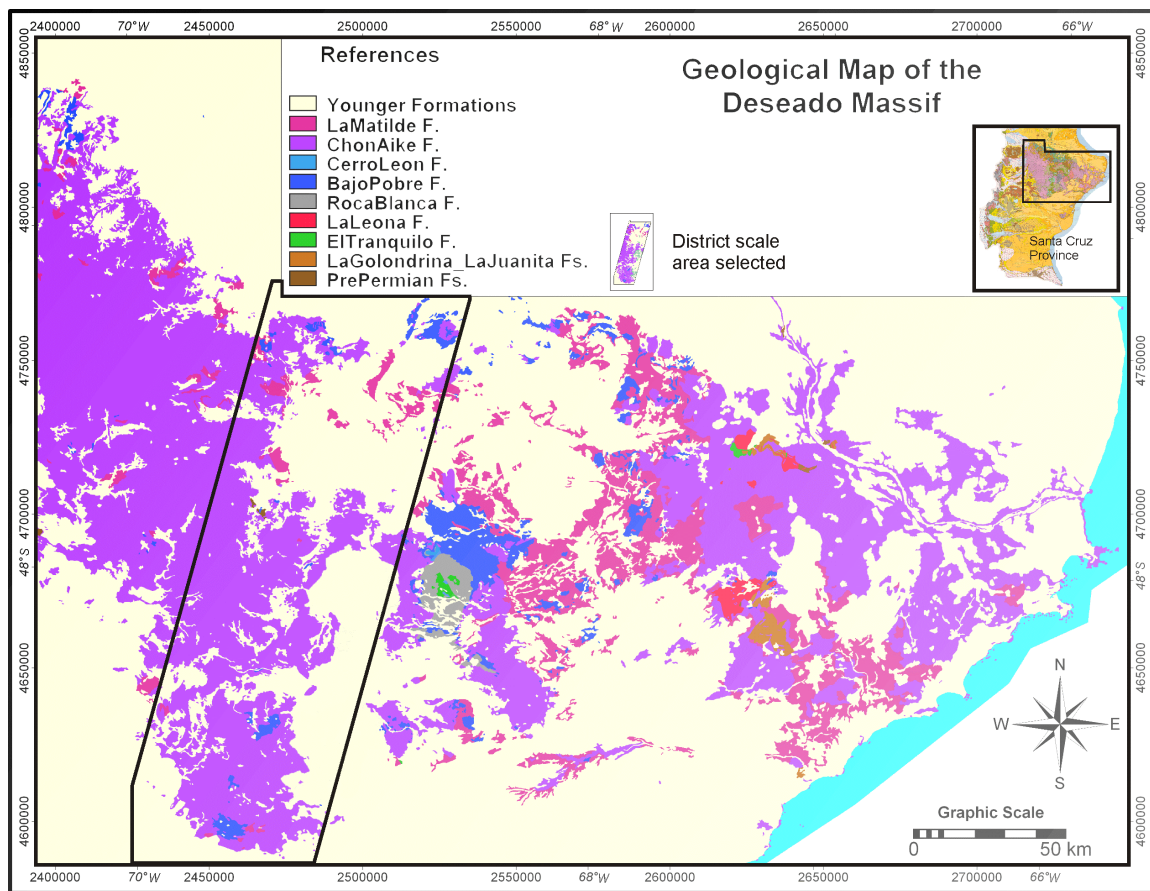


Figure 4.3: Geological map of the Deseado Massif compiled by digitization of seven 1:250,000 scale geological maps produced by SEGEMAR.

4.2.2. Regional scale hydrothermal alteration

Eleven not-validated level 1G¹ scenes of Landsat 7 ETM+ were used to map regional scale clay alteration. Data were acquired via Internet from the Earth Science Data Interface (ESDI) of the University of Maryland. The scenes were already geocoded to zone +19 of the UTM coordinate

¹ Level 1G scenes are 8-bit products radiometrically and geometrically corrected to user-specified parameters including output map projection, image orientation and pixel grid-cell size. They are free from distortions related to the sensor, satellite, and Earth (e.g., rotation, curvature). Not-validated means that it is not guaranteed that the position of features in the image and in the ground can be matched as accurately as less than 45 m.

system, using the WGS84 datum and reference ellipsoid. Therefore, they were resampled to zone 2 of the Gauss Kruger coordinate system. The Landsat images used here were acquired by the sensor in different seasons and times from September to February and from years 1999 to 2002.

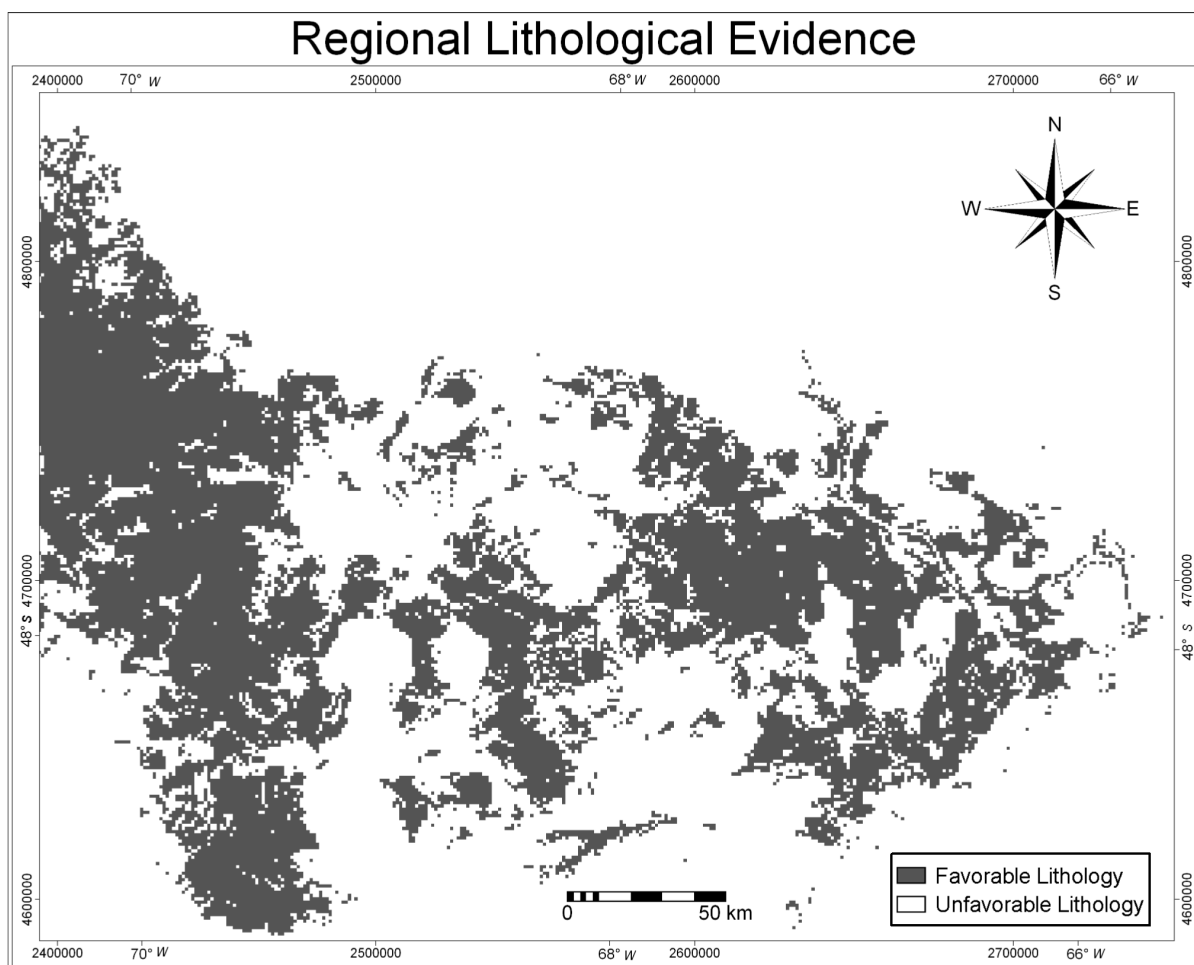


Figure 4.4: Map of regional scale lithological evidence. Chon Aike, La Matilde and Bajo Pobre Formations have been grouped in one unit.

Two techniques for alteration mapping, using Landsat 7 data, were tested in a known area. One technique uses ratios of band 5 to band 7; the other is the Crósta technique (Crósta and Moore, 1989), which is based in principal component analysis and was applied using bands 1, 4, 5 and 7. The band ratio technique used in this research is based on the fact that clay minerals (a) absorb electromagnetic radiation in the wavelengths of band 7 of Landsat and (b) reflect radiation in band 5 (Fig. 4.1). The ratio of band 5 to band 7 of sectors with clay minerals will thus be higher than those of sectors without clay minerals.

The Crósta technique, originally called Oriented Principal Component Selection (Crósta and Moore, 1989), uses principal component analysis (PCA) in a selective way, using only bands that would theoretically describe a feature under study and avoiding bands that would cause interference. It is based on the examination of PCA eigenvector loadings to decide which principal component image concentrates most of the information directly related to the theoretical spectral signatures of the feature being mapped. With Landsat ETM data the hydroxyl minerals are usually mapped by applying PCA to bands 1, 4, 5 and 7 and using the image of the principal components (PC) that show the higher difference, with opposite sign, between eigenvector loadings corresponding to bands 5 and 7; usually PC4 or PC3. If band 5 has positive sign, the clay alteration areas will appear as bright pixels;

otherwise, the pixels would be dark, but this can be inverted by negation of the image. Prior to the application of the Crósta technique, the dark object and sun angle corrections were applied to the image. The first one was applied to minimize the adverse effects that haze usually causes over bands 1 and 4; the second was applied to minimize the difference in illumination between scenes that should latter be used together. This difference is mainly produced because of the variation in the sun elevation in different seasons and times.

Both mapping techniques produced similar results (Fig. 4.5); but the Crósta technique showed some disadvantages in comparison to the band ratio technique. The disadvantages of the Crósta technique include the generation of negative numbers, the complexity of PCA, slightly less contrast, and different results obtained in overlapping areas for each one of the overlapping scenes. The last one was a serious disadvantage, which could not be overcome even using histogram matching or manual matching of the scenes. Therefore, ratios of bands 5 over 7 were selected to map clay alteration over the whole area.

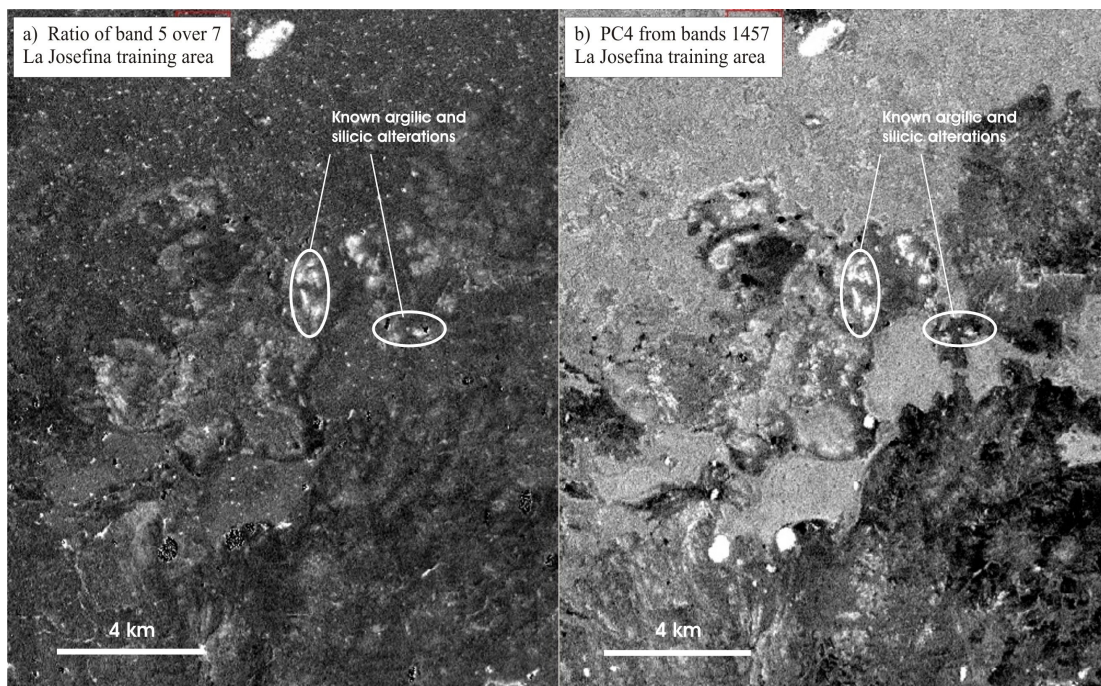


Figure 4.5: Comparison of the results of clay alteration mapping in the La Josefina test area. a) Ratios of band 5 to 7; b) Principal component image 4 from the PCA of bands 1, 4, 5 and 7. The ratio technique shows slightly better contrast, although both enhance areas with known alteration.

The first step during alteration mapping of the whole area was to apply an absolute sun angle correction to every Landsat 7 ETM+ scene using the following formula (Prakash, 2001):

$$DN' = \frac{DN}{\sin \alpha}$$

where DN' is the new digital number, DN is the original digital number and α is the solar elevation angle, which is provided in the header file of the images. In the scenes processed in this research, α varied from 32 to 52 degrees. The dark object correction was not applied because infrared bands are not significantly affected by haze. After sun angle correction, bands 5 and 7 of the 11 Landsat scenes were mosaicked.

The mosaicked bands 5 and 7 were used to create a band ratio image, which was then filtered with a low pass 9x9 kernel size filter in ENVI 3.6 to minimize the pepper-salt effect and high variability produced by a great number of small areas composed by a few pixels (sometimes one or two) that show high band ratio. In that way the image was smoothed, many small areas with high values disappeared, and larger areas with high values were preserved and slightly enhanced. After masking the zero values, which correspond to black areas around the scene, the mean and standard deviation of the filtered image were calculated to have an indication of which should be considered anomalous values. From these calculations and using known alteration zones as control information, a threshold was determined between the mean (1.1433) and the mean plus one standard deviation (1.2064) to define anomalous values; this threshold is 1.18. Then, a binary map was generated, in which values higher than 1.18 were mapped as clay alteration (Fig. 4.6).

The resultant clay alteration map showed many anomalies that are not really zones with hydrothermal alteration clays but low areas, such as lagoons and small valleys, where presumably clayey materials have been deposited by water. Water shows high absorption in band 5 of Landsat data; therefore, to eliminate part of these false hydrothermal clay anomalies, a mask generated using the pixel values lower than DN=70 in band 5 (arbitrarily selected after few tests) was applied to the alteration anomaly image.

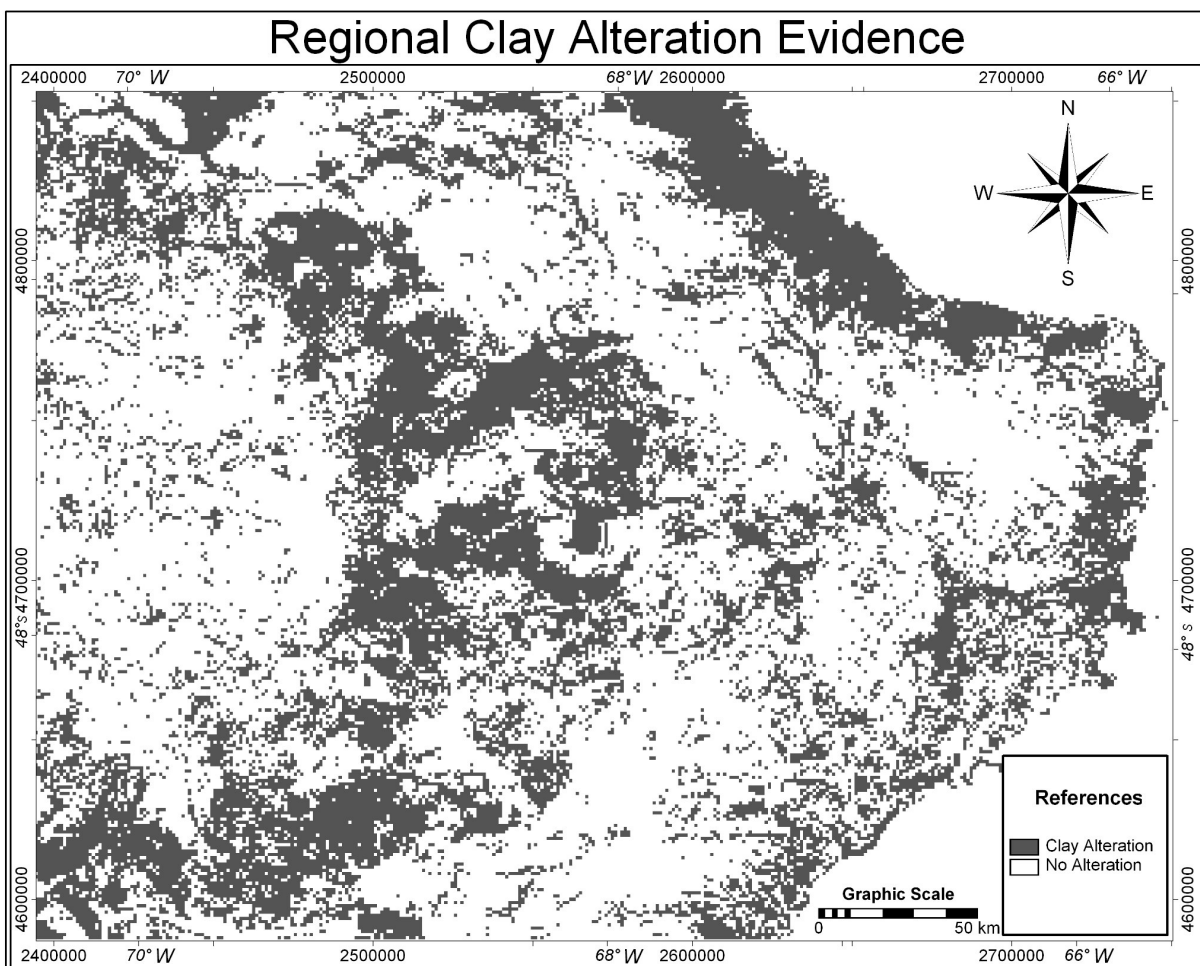


Figure 4.6: Map of regional scale clay alteration. Ratio image of bands 5 to 7 of Landsat 7 ETM+ have been filtered (by a low pass 9x9 kernel size filter) and thresholded to generate this map.

4.2.3. Regional scale structural features

A Digital Elevation Model (DEM) of 90 m resolution was the principal RS data used, with support of Landsat images, for regional scale lineament mapping. The DEM was obtained freely from the National Map Seamless Data Distribution System of the USGS. This product was generated from data acquired by the Shuttle Radar Topography Mission (SRTM). The SRTM, sponsored by the National Geospatial-Intelligence Agency (NGA) and the National Aeronautics and Space Administration (NASA), consisted of a specially modified radar system that flew onboard the Space Shuttle Endeavour during February of 2000.

The DEM was processed to generate shaded relief images that helped to recognize and delineate most regional scale lineaments. The shaded relief images were made using a moving window of 3x3 pixels, a sun angle elevation of 45°, and illumination angles (azimuth) of 0°, 30°, 60°, 90°, 120°, and 150°, to enhance linear features with different orientations. The digitized regional scale lineaments are large linear zones composed by smaller recognizable linear features. They are recognized at scales of 1:1,500,000 or smaller, and their approximate central axes were digitized (Fig 4.7). These regional scale features are likely to represent deep major faults zones probably normal faults related to the general extension during the Jurassic period, that were latter reactivated by transcurrency.

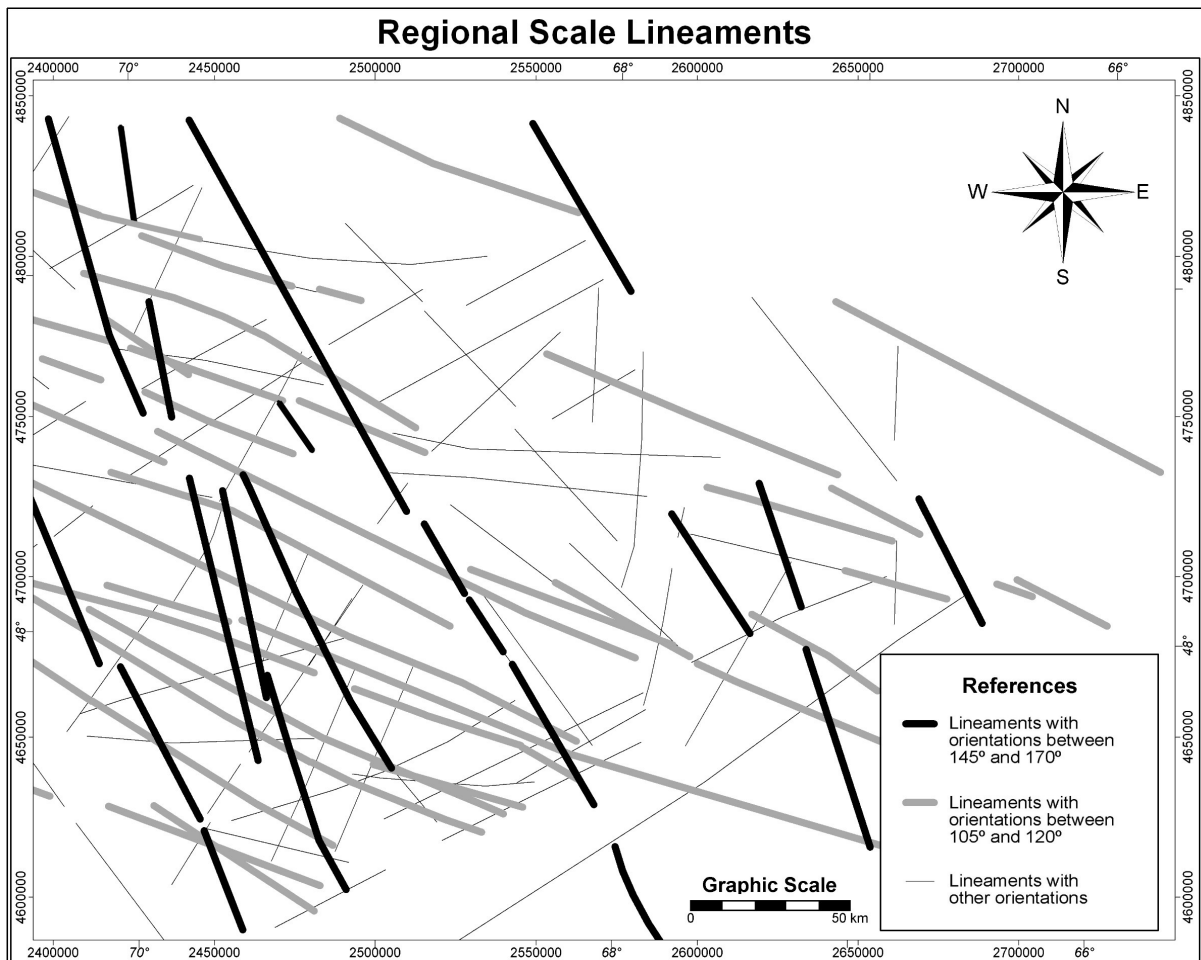


Figure 4.7: Regional scale lineaments interpreted and digitized over shaded relief images of a DEM with visual support of mosaicked Landsat images.

4.3. Extraction of district scale geological features

A portion of the Deseado Massif considered suitable for exploration of LSED and parts of which were already pointed out by the regional scale mapping, was selected to carry out a district scale potential mapping. This area is approximately located between latitudes 47°S and 49°S and between longitudes 68° 30'W and 70°W. It is a NNE-SSW oriented elongated area (Fig. 4.3). This selection was partially done because of the availability of ASTER data over it, which is considered a useful source of data to map alterations.

4.3.1. District scale lithological features

The same digitized geological maps used for regional scale mapping were used for district scale mapping. Four Pre-Bajo Grande lithological units are present in the selected area: Pre-Permian Formations, Bajo Pobre Formation, Chon Aike Formation and La Matilde Formation. One binary lithological map was created for each of those units, to be later used in the mineral potential mapping.

4.3.2. District scale hydrothermal alteration

Clay and silica alterations were used for district scale potential mapping. They were extracted from four on-demand ASTER level 2 scenes. The reflectance from atmospherically corrected SWIR bands was used to map clays, while the emissivity from TIR bands was used to map silica alteration. To select the method that was best suited for district-scale clay mapping, La Josefina project was used as a test area. Several options based in the indicative absorption peaks of clay minerals in wavelengths corresponding to different ASTER bands were experimented, including: (1) Spectral Angle Mapper (SAM) method; (2) Principal component analysis (Crósta technique); and (3) Different band ratios.

Spectral Angle Mapper was tested, using SWIR bands 4, 5, 6, 7, 8 and 9. The JPL1 (Jet Propulsion Laboratory) mineral spectral library was used; which is composed of spectra of wavelengths from 0.4 to 2.5 μm obtained from less than 45 micrometers grain size minerals. Kaolinite, illite and montmorillonite were mapped with this method. The mapping of illite yielded results that were not according to the known areas of alteration and mapping of kaolinite generated results that were partially coincident with the known alteration. The clay mapping was oriented to map mainly illite and montmorillonite that are the most abundant clay alterations in LSED elsewhere and in the Deseado Massif; therefore, and mainly in view of the results obtained for illite, SAM method was not selected for district scale mapping. Probably it would be suitable for deposit scale mapping, using better ground control.

Crósta technique applying principal components to ASTER bands 4, 5, 6, 7, 8 and 9 was tested to map clay alteration. The eigenvector loadings of the PC3 image were positive and high for ASTER band 4, negative and low for band 5 and negative and lower for band 6; therefore, that image can be used to map montmorillonite, illite, and kaolinite (and probably scarce alunite) because this is coincident with the spectral curves of these minerals (Fig. 4.8).

Ratios of ASTER bands $4/5$, $4/(5+6)$, $4/6$ and $(5+7)/6$ were applied. All the resulting images were in good agreement with the known areas of alteration (Fig.4.9). Finally, ratio of bands $4/6$ was selected to map the clay alterations for the district scale potential mapping. This ratio is simple to generate and interpret, and was considered the one that better enhanced most of the known areas of alteration. Because illite, montmorillonite, and kaolinite have high absorption in band 6 and low absorption in band 4 (Fig. 4.8), this ratio is probably the more suitable for these minerals. The mosaicked bands 4 and 6 were used to create a band ratio image, which was then filtered with a low pass 5×5 kernel size filter in ENVI 3.6 to minimize the pepper-salt effect.

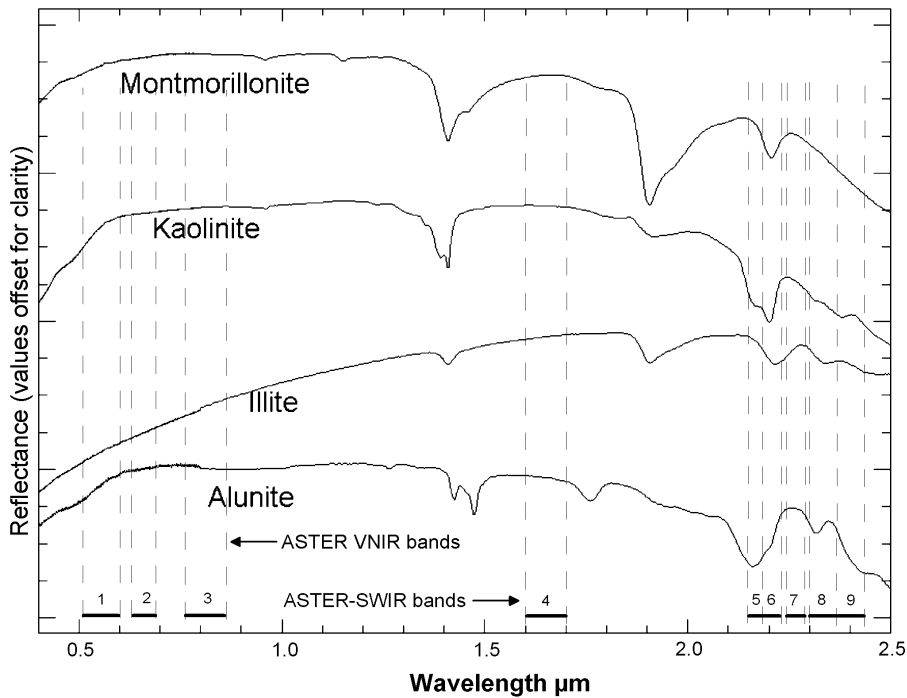


Figure 4.8: Reflectance curves for four common alteration minerals and ASTER SWIR and VNIR spectral bands. Curves were produced with data from the JPL1 spectral library with materials of less than 45 microns grain size (Grove et al., 1992).

After mosaicking the TIR bands of four scenes to be used, an average filter with a kernel of 3x3 pixels was applied to the mosaic to reduce the effect of stripping present in the original data. Later, the K_{silica} index proposed by the Metal Mining Agency of Japan (Miyatake, 2002; MMAJ, 2000) was used to map silica content. The following formula was applied:

$$K_{silica} = \log((E[10] + E[11] + E[12])/3 / E[13]) * (-1)$$

where $E[n]$ are values in each ASTER TIR band n . The resultant image (Fig. 4.10b) shows anomalously high silica content coincident with zones of silica alteration that have been mapped in the field (Fig. 4.9b). An image of band ratio 13/12 was also produced and the results were very similar to those yielded by the K_{silica} index (Fig. 4.9a). However, the K_{silica} index image was selected because it shows slightly better definition of the contours of known features.

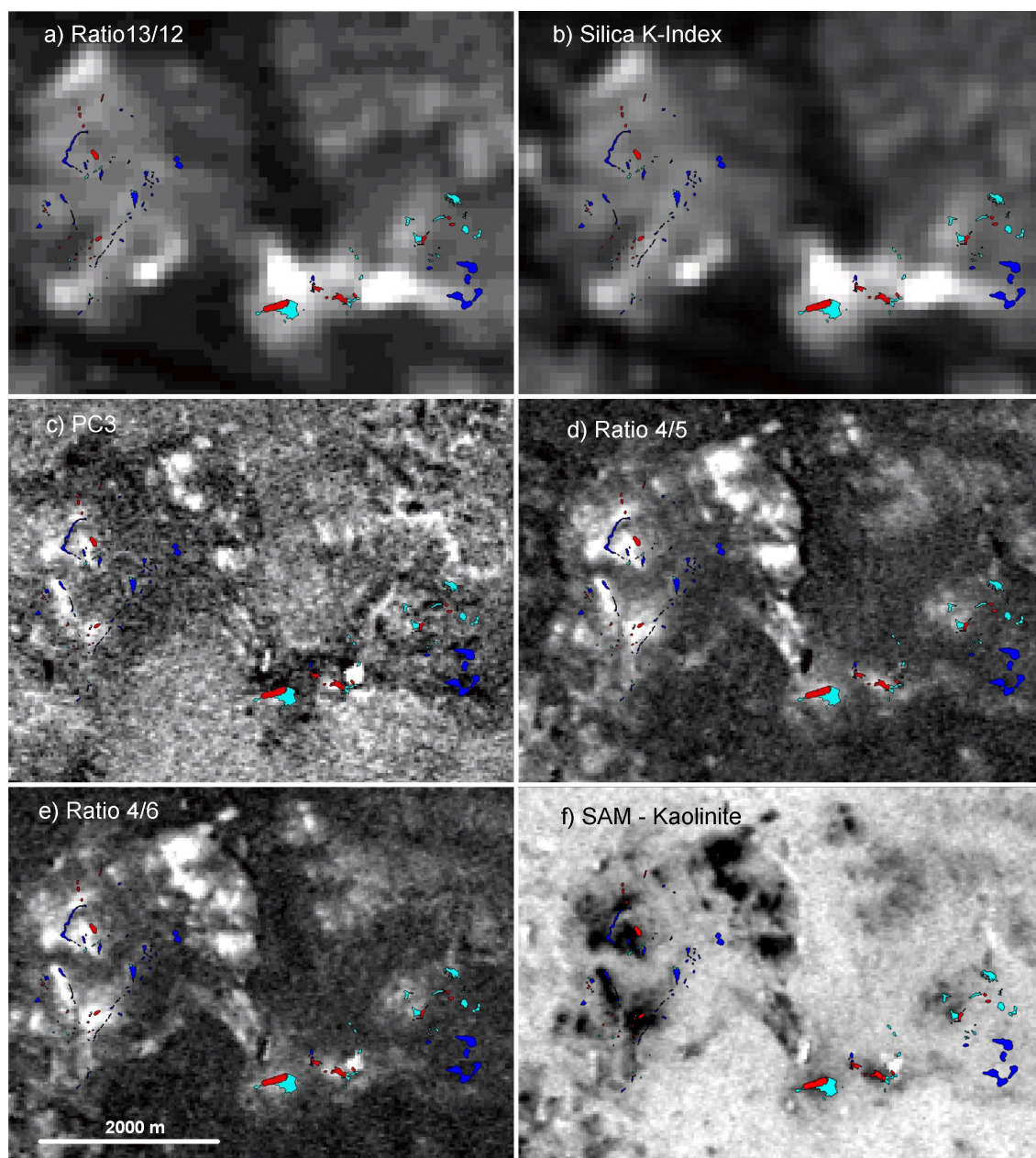


Figure 4.9: Results obtained with different alteration mapping techniques in the La Josefina test area. **a)** and **b)** were applied to TIR bands to map silica content; **c)**, **d)**, **e)** and **f)** were applied to SWIR bands to map clay alteration. Result in each case, were stretched in the same way to compare them (first, linear stretch to 255 possible values; second, 1% histogram stretch for better display). Red polygons indicate presence of clays including kaolinite in the south-central part; blue polygons represent opaline silica; and cyan polygons are silicified rocks; usually the opaline silica in the west is surrounded by some argillized rocks.

4.3.3. District scale structural features

District scale structural features were extracted from lineaments that were on-screen digitized from Landsat images and derived products. During digitization, the images were displayed on the computer monitor at full resolution scale (i.e., a scale before which individual pixels are not recognizable anymore), which in this case was about 1:100,000. Special attention was paid for not to trace features likely to be due to stratification, or slumping in the margins of quaternary or tertiary age basaltic terraces. However, some of the lineaments were digitized over terraces because they probably

represent fractures located below the basalts and were important enough to control the shape of the lava flows deposited over them. Most of the lineaments digitized probably represent portions of longer fractures, normal faults common in the volcanic environment, or joints.

Different image enhancements and band combinations were used prior to digitization. Most lineaments were digitized over 741 color composites of individual scenes or over a mosaic generated with those color composites. Shaded relief images of the Landsat mosaic (illuminated from different directions) were combined with RGB color composites to have the color of the composite and the directional enhancement of the shaded relief. In addition, band 7 images were filtered with an edge enhancement filter and used to complement lineament interpretation. The edge enhancement filter used has the following configuration:

-1	-1	-1
-1	17	-1
-1	-1	-1

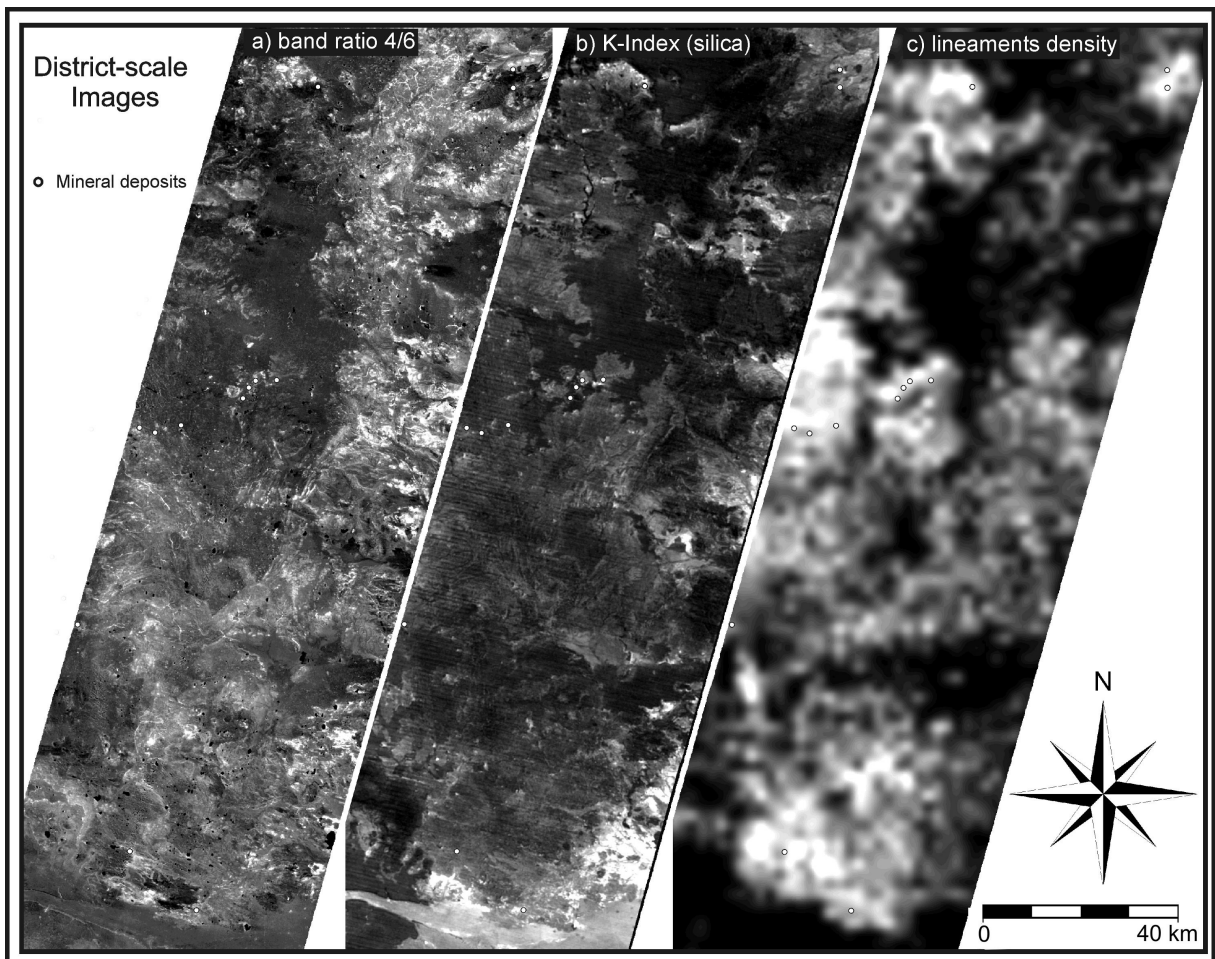


Figure 4.10: Images produced for district scale potential mapping. **a)** Clay alteration image produced from SWIR bands of ASTER. **b)** Silica alteration image (k-Index) generated from TIR bands of ASTER. **c)** Lineament density image produced from lineaments interpreted from Landsat images and derived products. White dots are mineral deposits.

The density of lineaments was calculated for an output pixel size of 2000 m. For each pixel, lineament density equal to total length of lineament segments in that pixel divided by pixel area. The lineament density image was densified up to a pixel size of 500 m and then resampled to the same georeference used for the rest of the maps for district scale potential mapping (Fig. 4.10c).

4.4. Concluding remarks

This chapter explains the procedures followed to extract regional and district scale geological features. The sources of data for the task explained here were geological maps (1:250,000 scale), Landsat images, ASTER images and a DEM generated with radar data from the SRTM.

For regional scale LSED potential mapping, the themes of spatial evidences extracted are lithology, alteration and structure. Lithological evidence consisted of maps of pre-Bajo Grande lithologies. Clay alteration was identified using a simple band ratio 5/7 using Landsat data. Band ratio 5/7 was found more useful than the Crósta (directed principal components) technique in identifying regional scale clay alteration. Structural evidences consisted of two sets of regional fracture zones – one set with azimuth orientations of 105-125° and the other set with azimuth orientations of 145-170°. These structural evidences were interpreted from shaded relief images of the DEM with visual support using enhanced Landsat images.

For district scale LSED, the themes of spatial evidences extracted are also lithology, alteration and structure. Lithological evidence was extracted from the same geological map used for regional scale. Alteration evidence was extracted from ASTER data and consisted of clay and silica alteration, respectively mapped using band ratio 4/6 and K-silica index. Band ratio 4/6 was found more useful than other ratios and methods for detecting district scale clay alteration. Structural evidence consisted of a map of density of lineaments, which were interpreted from enhanced Landsat data.

The spatial evidences extracted are used in predictive mapping of LSED potential, which is explained in the next chapter.

CHAPTER 5: Predictive Mapping of LSED Potential

In this chapter, some assumptions (deposit recognition criteria) extracted from concepts built up in the previous chapters, were tested and quantified to use them for mineral potential predictions. There are several methods to quantify the spatial associations between mineral deposits and geological features, such as point pattern analysis and weights of evidence methods. Point patterns were already studied by the use of Fry analysis in chapter 3 to obtain information that helped to decide which fracture systems are related to mineralization in the Deseado Massif. In the present chapter, the weights-of-evidence method was applied to quantify spatial associations between mineral deposits and three different types of geological features, which represent the deposit recognition criteria defined in chapter 3. The weights-of-evidence method has the advantage that quantification of spatial associations leads directly to weighting of evidential maps to be combined for mineral potential mapping. Weights-of-evidence method was applied to two datasets, one for regional scale mapping and the other for district scale mapping, generated and explained in chapter 4.

5.1. Weight-of-evidence (WofE) method

To minimize subjective bias in determining spatial associations between mineral deposits and geological features, a quantitative methodology has to be applied. Weights-of-evidence is a quantitative data-driven method used to combine datasets. It uses a log-linear form of the Bayesian probability model to estimate the relative importance of evidences by statistical means. It has been applied to combine evidences in various disciplines such as in quantitative medical diagnosis, ecology and geology (Bonham-Carter, 1994)

In the Bayesian approach, prior and posterior probabilities are amongst the most important concepts. Given an area of study that contains certain number of mineral deposits, the prior probability that a deposit occur per unit area is calculated as the total number of deposits over the total area. This initial estimate can be later increased or diminished in different areas by the use of other evidences. The prior probability can be multiplied by a factor to obtain a posterior probability that a deposit occurs given certain evidence. This posterior probability can in turn be multiplied by a second factor (calculated from another evidence) being used, in this way, as a prior probability to obtain a second posterior probability.

5.1.1. WofE calculations

Given a study area, T , composed by a number of unit area $N\{T\}$ (unit cells in a raster map) containing a number of deposits $N\{D\}$ (Fig.5.1) and assuming that each deposit occupies one unit area (one unit cell), the probability that one randomly selected unit area or cell in the map contain a deposit when no other information is available, is:

$$P\{D\} = N\{D\}/N\{T\} \quad (5-1)$$

which can be used as an estimate of the prior probability of a deposit. If a binary map, representing a new evidence, B , is also present, the probability of finding a new deposit given the presence of the new evidence, can be expressed as a conditional (or posterior) probability, $P\{D|B\}$.

$$P\{D|B\} = \frac{P\{D \cap B\}}{P\{B\}} = P\{D\} \frac{P\{B|D\}}{P\{B\}} \quad (5-2)$$

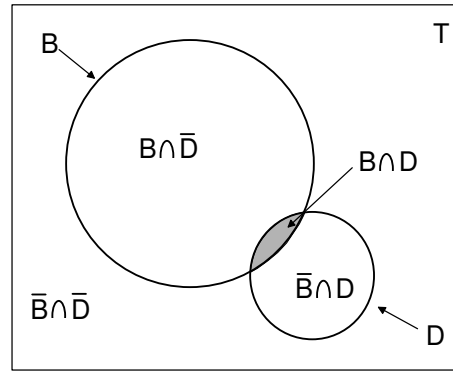


Fig. 5.1: Venn diagram showing an area of study T , an area covered by mineral deposits D , and an area covered by a binary predictor pattern B , which represents certain evidence that can be used to update the prior probability of deposit; D and B means presence while \bar{D} and \bar{B} means absence of binary patterns.

Conversely, the posterior probability of a deposit given the absence of the new evidence, $P\{D|\bar{B}\}$, can be expressed as:

$$P\{D|\bar{B}\} = \frac{P\{D \cap \bar{B}\}}{P\{\bar{B}\}} = P\{D\} \frac{P\{\bar{B}|D\}}{P\{\bar{B}\}} \quad (5-3)$$

Probability (P) can be expressed as odds (O) or vice versa using the equation:

$$O = P/(1 - P) \quad (5-4)$$

Therefore, equations 5-2 and 5-3 can be expressed, respectively, in an odds formulation as:

$$O\{D|B\} = O\{D\} \frac{P\{B|D\}}{P\{B|\bar{D}\}} \quad \text{and} \quad (5-5)$$

$$O\{D|\bar{B}\} = O\{D\} \frac{P\{\bar{B}|D\}}{P\{\bar{B}|\bar{D}\}}. \quad (5-6)$$

where $O\{D|B\}$ and $O\{D|\bar{B}\}$ are the posterior odds of a mineral deposit given presence and absence of evidence B , respectively; $P\{B|D\}/P\{B|\bar{D}\}$ is known as “sufficiency ratio” (LS) and $P\{\bar{B}|D\}/P\{\bar{B}|\bar{D}\}$ is known as “necessity ratio” (LN). LS and LN are also known as “likelihood ratios” (Bonham-Carter, 1994).

Logits are natural logarithms of odds and they are used in weights of evidence modeling. The natural logarithms are applied to both sides of equations 5-5 and 5-6 obtaining the next equations:

$$\text{Logit}\{D|B\} = \text{Logit}\{D\} + W^+ \quad \text{and} \quad (5-7)$$

$$\text{Logit}\{D|\bar{B}\} = \text{Logit}\{D\} + W^-. \quad (5-8)$$

where W^+ is the \log_e of LS and a positive weights-of-evidence when evidence B is present, and W^- is the \log_e of LN and a negative weights-of-evidence when evidence B is absent. In weights-of-evidence

method, the values of W^+ and W^- are calculated using the mineral deposit data and applying the natural logarithms of LS and LN.

$$W^+ = \log_e \frac{P\{B|D\}}{P\{B|\bar{D}\}} \text{ and} \quad (5-9)$$

$$W^- = \log_e \frac{P\{\bar{B}|D\}}{P\{\bar{B}|\bar{D}\}}. \quad (5-10)$$

The variances of the weights can be calculated respectively as (Agterberg et al., 1990; Bishop et al., 1975):

$$s^2(W^+) = \frac{1}{N\{B \cap D\}} + \frac{1}{N\{B \cap \bar{D}\}} \text{ and} \quad (5-11)$$

$$s^2(W^-) = \frac{1}{N\{\bar{B} \cap D\}} + \frac{1}{N\{\bar{B} \cap \bar{D}\}}. \quad (5-12)$$

The contrast C is a measure of the spatial association between a binary predictor pattern and mineral deposit points (Carranza, 2002), and is calculated as:

$$C = W^+ - W^- \quad (5-13)$$

A studentized value of the contrast is a useful measure of the certainty with which the contrast is known; a value of 1.5 or even 2 are ideal (Bonham-Carter, 1994). The studentized C ($Sig C$) value is the ratio of the contrast to its standard deviation, or:

$$Sig C = C / \sqrt{s^2(W^+) + s^2(W^-)} \quad (5-14)$$

When evidences from several maps are combined, weights are calculated for each map and then combined in a single equation; however, this requires an assumption of conditional independence. Usually spatial data do not satisfy the assumptions of classical statistical models particularly those regarding independence. However, assuming conditional independence, a model can be generated and although it does not fit the data perfectly, it provides a simplification that can be used for prediction and can give information about the relative contributions of each source of evidence (Bonham-Carter, 1994). The posterior probability of a deposit given the presence of two predictor patterns B_1 and B_2 can be expressed by the Bayes Rule:

$$\begin{aligned} P\{D | B_1 \cap B_2\} &= \frac{P\{D \cap B_1 \cap B_2\}}{P\{B_1 \cap B_2\}} = \frac{P\{B_1 \cap B_2 | D\} P\{D\}}{P\{B_1 \cap B_2\}} \\ &= \frac{P\{B_1 \cap B_2 | D\} P\{D\}}{P\{B_1 \cap B_2 | D\} P\{D\} + P\{B_1 \cap B_2 | \bar{D}\} P\{\bar{D}\}} \end{aligned} \quad (5-15)$$

If B_1 and B_2 are conditionally independent of each other with respect to the set of mineral deposits, equation 5-15 can be simplified because the relation $P\{B_1 \cap B_2 | D\} = P\{B_1 | D\} P\{B_2 | D\}$ is satisfied:

$$P\{D | B_1 \cap B_2\} = P\{D\} \frac{P\{B_1 | D\}}{P\{B_1\}} \frac{P\{B_2 | D\}}{P\{B_2\}} \quad (5-16)$$

Equation 5-16 is the same as equation 5-2 except that multiplying factors for two maps are used to update the prior probability to give the posterior probability. Using the odds formulation it can be shown that:

$$\log_e O\{D | B_1 \cap B_2\} = \text{logit}\{D\} + W_1^+ + W_2^+, \quad (5-17)$$

$$\log_e O\{D | B_1 \cap \overline{B_2}\} = \text{logit}\{D\} + W_1^+ + W_2^-, \quad (5-18)$$

$$\log_e O\{D | \overline{B_1} \cap B_2\} = \text{logit}\{D\} + W_1^- + W_2^+, \text{ and} \quad (5-19)$$

$$\log_e O\{D | \overline{B_1} \cap \overline{B_2}\} = \text{logit}\{D\} + W_1^- + W_2^-. \quad (5-20)$$

Finally, the general expression to combine “ n ” maps is:

$$\log_e O\{D | B_1^k \cap B_2^k \cap B_3^k \cap \dots B_n^k\} = \sum_{j=1}^n W_j^k + \log_e O\{D\} \quad (5-21)$$

where k is (+) or (-) if the binary predictor pattern is present or absent respectively. The posterior odds can be converted to posterior probabilities, based on equation 5-4, and that represents degree of mineral potential (Carranza, 2002).

5.1.2. Tests of conditional independence

Tests should be carried out to assure that assumption of conditional independence among evidences with respect to target variables is not violated. Two tests serve to this objective; first and prior to the final predictor maps combination, a pairwise test between evidence maps can be executed; and second, after combination of predictor maps, an overall test amongst all input maps can be carried out.

If two binary patterns are conditionally independent with respect to the set of deposits, then:

$$N\{B_1 \cap B_2 \cap D\} = \frac{N\{B_1 \cap D\} N\{B_2 \cap D\}}{N\{D\}} \quad (5-22)$$

where the left hand of the equation is the observed number of deposits occurring in the overlap region where both binary patterns B_1 and B_2 occur. The right hand is the predicted number of deposits in that overlap region.

The relationships between two patterns in which deposits are present can be shown in a contingency table, in which the four central cells show the four possible overlap conditions (Table 5.1) under either observed or expected (predicted) assuming independence situations.

Table 5.1: Contingency table showing four possible overlap conditions (cells in grey) between two binary predictor patterns and binary patterns of mineral deposits (Modified from Bonham-Carter, 1994).

	Pattern B1 Present	Pattern B1 Absent	Total
Pattern B2 Present	$N\{B_1 \cap B_2 \cap D\}$	$N\{\bar{B}_1 \cap B_2 \cap D\}$	$N\{B_2 \cap D\}$
Pattern B2 Absent	$N\{B_1 \cap \bar{B}_2 \cap D\}$	$N\{\bar{B}_1 \cap \bar{B}_2 \cap D\}$	$N\{\bar{B}_2 \cap D\}$
Total	$N\{B_1 \cap D\}$	$N\{\bar{B}_1 \cap D\}$	$N\{D\}$

To test the null hypothesis that there is no association between a pair of predictor maps, a statistic that compares the entire set of observed counts with the set of expected counts can be used. This is the chi-square statistic, X^2 , which is a measure of how much of the observed cells counts in a two way table diverge from the expected (predicted) cell counts (Moor and McCabe, 1999). This statistic is calculated as:

$$X^2 = \sum_{i=1}^4 \frac{(observed_i - expected_i)^2}{expected_i} \quad (5-23)$$

where the observed and expected values correspond to each of the four overlapping conditions between two binary patterns. Using equations 5-22 and 5-23, the X^2 value for each pair of binary predictor patterns with respect to the mineral deposits can be calculated.

Chi-square is strongly dependent on the units of measurement, being proportional to the size of the areal unit. However, because the mineral deposits are considered as unit cells, the units of measurement do not affect the resulting X^2 , and the resultant values from the test can be compared with critical values of X^2 with one degree of freedom (Bonham-Carter, 1994). The critical X^2 value with one degree of freedom at the 95% significant level is 3.84 (Davis, 1986). The null hypothesis can, therefore, be rejected at that confidence level if a calculated value of X^2 is higher than 3.84. Values higher than this threshold suggest that the conditional independence has been seriously violated and therefore, one of the maps has to be rejected or modified to reduce the problem (Bonham-Carter, 1994) or both maps can be combined.

After combination of all predictor maps that passed the first test of conditional independence, a second and simple test can be carried out by comparing the observed number of deposits with the predicted number of deposits by the final probability map. The predicted number of deposits can be calculated as:

$$N\{D\}_{calc} = \sum_{k=1}^m P_k * N\{A\}_k \quad (5-24)$$

where $k=1,2,\dots,m$ are pixels in the map and $N\{A\}_k$ is area per unit cell. If the predicted number of deposits exceeds the number of observed deposits by about 10-15%, it suggests that assumption conditional independence is seriously violated and some changes have to be done to remedy that situation (Bonham-Carter, 1994).

In Table 5.2, all the equations used during the next sections are shown in a more compact way and practical notation.

Table 5.2: List of equations used for WofE calculations. *Std*=standard deviation; *npixt*=total pixels in study area; *npixd*=pixels with deposits; *npixb*=pixels of present binary pattern or cumulative buffer class; *npixbd*=pixels of present binary pattern or cumulative buffer class with deposits. (*m*₁, *m*₂, *m*_{*n*})=predictor (weight) maps. *PostPro*=posterior probability map. *N{D}pred*= predicted number of deposit; *Pp*=posterior probability of each pixel in posterior probability map; *npix*=number of pixels with certain posterior probability. (Compiled from Bonham-Carter, 1994; Carranza, 2003)

Equation	Meaning	Used in
$W^+ = \log_e \frac{npixbd * (npixt - npixd)}{(npixb - npixbd) * npixd}$	Positive weight	Weights-of-evidence calculation
$W^- = \log_e \frac{(npixd - npixbd) * (npixt - npixd)}{(npixt - npixd - (npixb - npixbd)) * npixd}$	Negative weight	Weights-of-evidence calculation
$C = W^+ - W^-$	Contrast between weights	Determining spatial association
$Sig C = \frac{C}{\sqrt{(Std.W^+)^2 + (Std.W^-)^2}}$	Significance of C	Determining optimal spatial association
$X^2 = \sum_{i=1}^4 \frac{(observed_i - expected_i)^2}{expected_i}$	Chi-square	Pairwise conditional independence test
$P\{D\} = N\{D\}/N\{T\}$,	Prior probability of a deposit.	Calculation posterior prob. map
$PriorOdds = Prior Prob. / (1 - Prior Prob.)$	Conversion to odds.	Calculation posterior prob. map
$Logit\{D\} = Log_e(PriorO) = Log_eO\{D\}$	Calculation of Logits	Calculation posterior prob. map
$PostPro = \frac{e^{(Logit\{D\}+m1+m2+m3+...mn)}}{1 + e^{(Logit\{D\}+m1+m2+m3+...mn)}}$	Calculation of posterior probability map	Predictive Mapping
$N\{D\}pred = \sum (Pp * npix)$	Calculation of total predicted deposits	Overall conditional independence test

5.2. WofE application to regional scale mapping of LSED potential

5.2.1. Spatial association of LSED with regional scale geological features

The spatial associations, at regional scale, of 48 LSED with lithology, clay alteration and two sets of fracture zones were investigated by means of weights of evidence approach. The spatial association with lithology was investigated using the Chon Aike, La Matilde, and Bajo Pobre Formations as favorable lithologies. The spatial association with clay alteration was studied using a binary map of clay alteration obtained by applying ratios of band 5 to 7 of Landsat data (Fig. 4.6). The association with regional fracture zones was studied using the two sets of large fracture zones suggested from the analysis carried out in chapter 3. One set corresponds to fracture zones with azimuth orientations of 105-125°, the other with azimuth orientations of 145-170°. The digitized axes of these fracture zones were buffered in steps of 2000 m, up to 20000. The spatial association was tested with these distance buffer maps (Figs. 5.2 and 5.3). All the evidential maps were resampled to a cell size of 1000x1000 m, and each LSED was represented in a raster map as one cell.

Each binary evidence map was crossed with the map of LSED to know the number of deposits that occupy cells in each present favorable binary pattern. The number of cells occupied by each binary pattern present was extracted from the histograms of each evidence map. The total number of cells used in the calculation of the weights and contrast was the total cells in the selected area minus the cells occupied by sea water (70828 cells or 70828 km²). Positive and negative weights (W^+ and W^-) and their standard deviations ($StdW^+$ and $StdW^-$), the contrast (C) and studentized contrast ($SigC$) were calculated using the formulas provided in section 5.1 (Table 5.3).

From the calculated values for the set of buffer zones of structures with azimuth orientations of 145-170°, the cumulative class buffer from 0 to 10000 m was selected because of its high contrast and high statistical significance ($SigC$). The values of contrast and studentized contrast obtained for the set of structures with azimuth orientations of 105-125°, show no pikes when plotted against distance, suggesting that the association with LSED is not specially strong at any distance from the center of the fracture zones (Fig. 5.4). Nevertheless, the cumulative buffer class from 0 to 6000 m was initially selected because it represents a strong change in the slope of the curve contrast vs. distance.

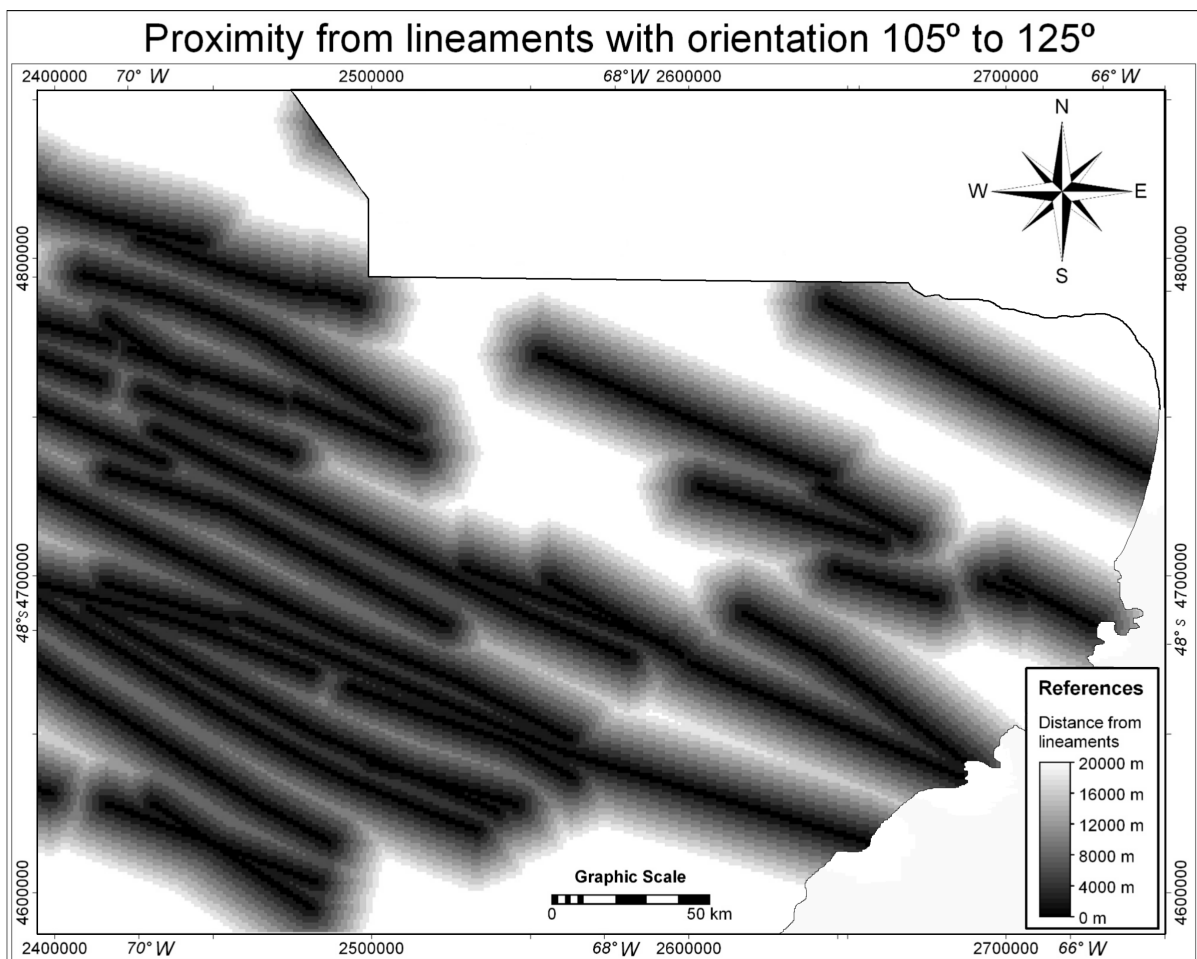


Fig. 5.2: Proximity to regional scale fractures with azimuth orientations of 105-125° used as one set of regional scale structural evidence.

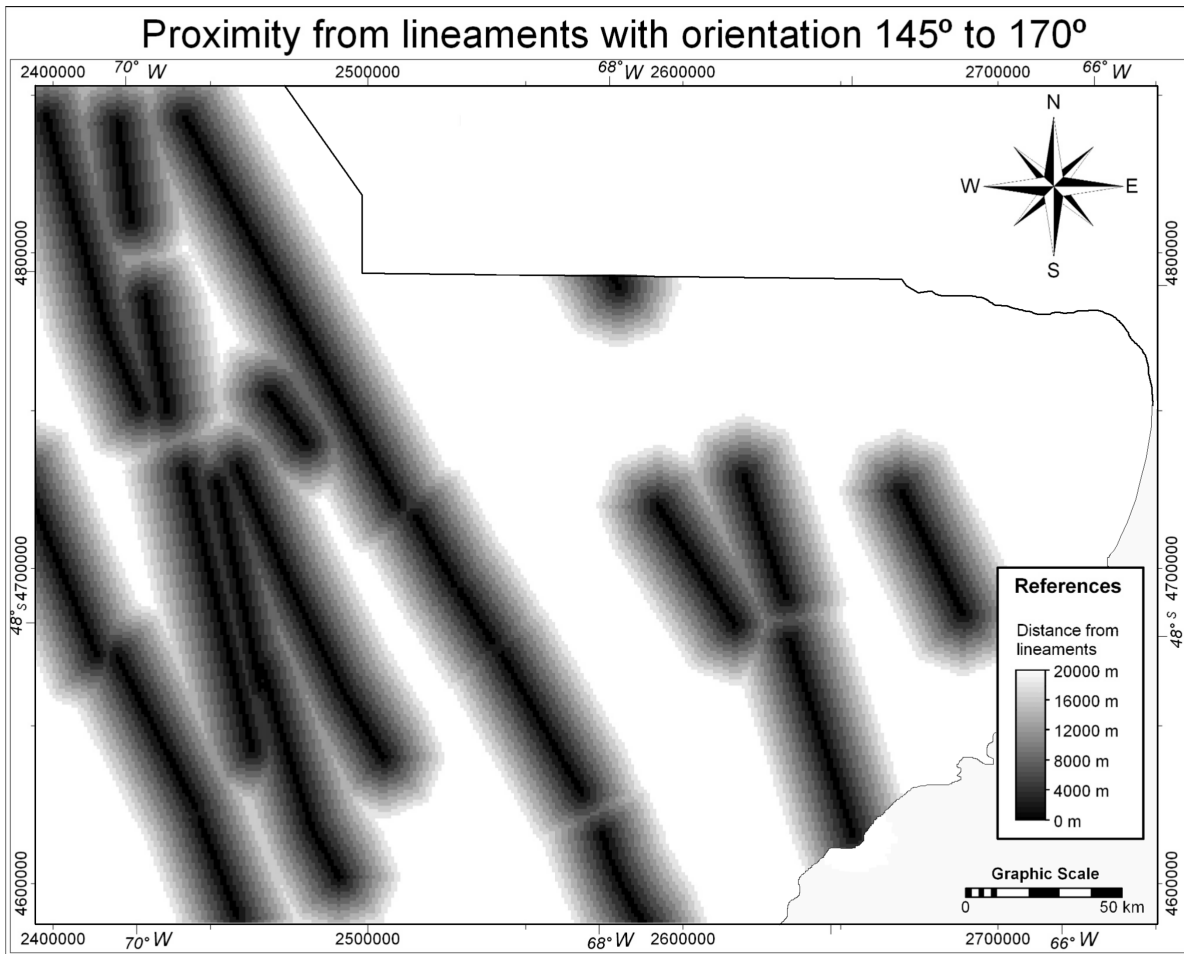


Fig. 5.3: Proximity to regional scale fractures with azimuth orientations of 145-170° considered to represent fractures produced by extension during Jurassic rifting and used here as one set of regional scale structural evidence.

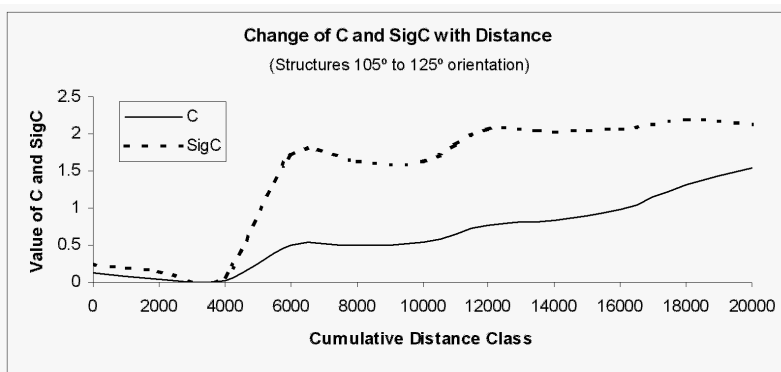


Fig. 5.4: Change of contrast (C) and studentized contrast ($SigC$) with cumulative distance class for structures with azimuth orientations of 105-125°.

Table 5.3: WofE calculations for the four regional evidence maps. Lithology includes Chon Aike, La Matilde and Bajo Pobre Formations. Bold italics indicate threshold values used to create binary predictor patterns.

Binary evidence map (buffer class)	Pixels of binary presence	Pixels of binary presence with deposits	W^+	W^-	C	$SigC$
<i>Lithology</i>	<i>23228</i>	<i>41</i>	<i>0.9584</i>	<i>-1.5284</i>	<i>2.4868</i>	<i>6.0795</i>
<i>Clay alteration</i>	<i>25144</i>	<i>32</i>	<i>0.6308</i>	<i>-0.6604</i>	<i>1.2913</i>	<i>4.2157</i>
Structures-145a170_0	2312	8	1.6332	-0.1492	1.7824	4.5953
Structures-145a170_2000	7168	19	1.3658	-0.3974	1.7633	5.9688
Structures-145a170_4000	12148	24	1.0712	-0.5053	1.5765	5.4579
Structures-145a170_6000	17009	28	0.8885	-0.6011	1.4896	5.0853
Structures-145a170_8000	21805	33	0.8043	-0.7956	1.5998	5.1357
<i>Structures-145a170_10000</i>	<i>26379</i>	<i>37</i>	<i>0.7281</i>	<i>-1.0078</i>	<i>1.7360</i>	<i>5.0536</i>
Structures-145a170_12000	30582	39	0.6328	-1.1092	1.7420	4.7096
Structures-145a170_14000	34446	39	0.5137	-1.0082	1.5219	4.1146
Structures-145a170_16000	38022	40	0.4401	-1.0226	1.4627	3.7759
Structures-145a170_18000	41317	42	0.4058	-1.2044	1.6102	3.6889
Structures-145a170_20000	43902	42	0.3450	-1.1127	1.4578	3.3397
Structures-105a125_0	5253	4	0.1166	-0.0100	0.1266	0.2423
Structures-105a125_2000	15650	11	0.0365	-0.0106	0.0471	0.1371
Structures-105a125_4000	24666	17	0.0169	-0.0091	0.0260	0.0860
<i>Structures-105a125_6000</i>	<i>32528</i>	<i>28</i>	<i>0.2393</i>	<i>-0.2608</i>	<i>0.5002</i>	<i>1.7078</i>
Structures-105a125_8000	38901	32	0.1939	-0.3020	0.4959	1.6191
Structures-105a125_10000	43409	35	0.1739	-0.3574	0.5313	1.6353
Structures-105a125_12000	47340	39	0.1954	-0.5705	0.7659	2.0707
Structures-105a125_14000	50984	41	0.1712	-0.6533	0.8245	2.0157
Structures-105a125_16000	54129	43	0.1590	-0.8172	0.9762	2.0657
Structures-105a125_18000	56822	45	0.1559	-1.1523	1.3082	2.1936
Structures-105a125_20000	58888	46	0.1422	-1.3982	1.5404	2.1323
Total pixels = 70828			Total pixels with deposits = 48			

The binary patterns corresponding to lithology and clay alteration and the cumulative buffer classes selected from each structural evidence map were converted to four predictor binary maps (Fig. 5.5). This was done by applying the correspondent positive weights to the areas with favorable binary patterns present or selected cumulative buffer class, and the negative weights to areas with favorable binary pattern absent or areas further away of the selected cumulative buffer class.

Then all predictor maps were crossed with each other producing 6 maps that were crossed in turn with the map of LSED to produce cross tables. From the resultant tables, the number of cells with mineral deposits and both binary patterns present, and the number of cells with deposits and each one of the binary patterns present were extracted to apply the pairwise conditional independence test. Outcome values from this test were high for pairs that included the set of structures with orientation 105-125° indicating that in those cases, the assumption of conditional independence was close to be violated (Table 5.4).

Table 5.4: Values of X^2 obtained in pairwise test of conditional independence for regional scale mapping.

	Lineaments 145-170°	Lineaments 105-125°	Lithology
Clay Alteration	0.24	2.74	1.34
Lineaments 145-170°		0.08	0.15
Lineaments 105-125°			2.99

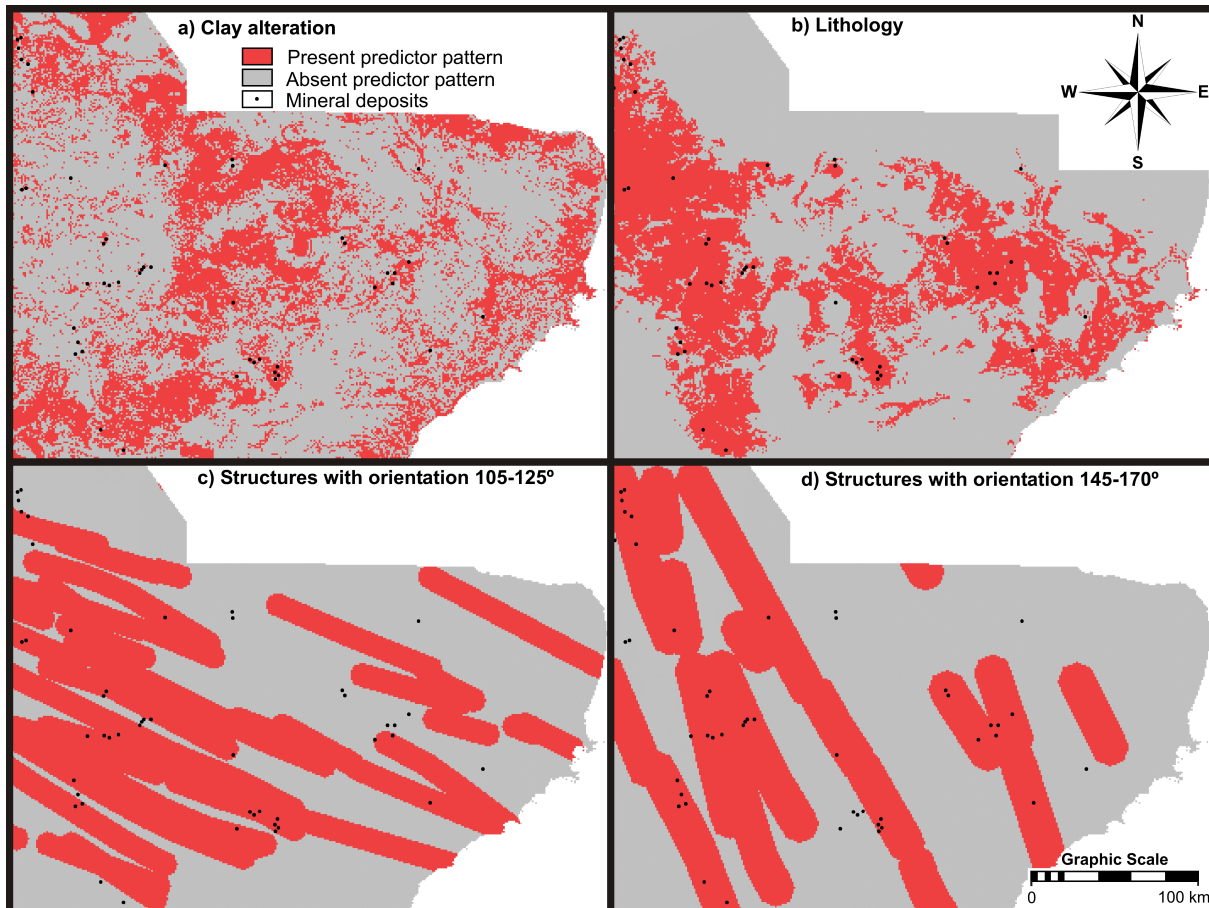


Fig. 5.5: Binary predictor maps used in regional scale mapping of LSED potential. Map c) was excluded from the combination of predictor maps.

To test the spatial association under other situation, the evidential maps of structures and that of clay alteration were used to calculate the weights and contrasts only inside the area occupied by the Pre-Bajo Grande Formations, reducing thus, the total area to be used from 70,828 km² to 29,254 km². In this case, the positive weights and values of C and $Sig C$ for the set of structures of orientations 105-125° are low and with negative sign, suggesting a possible negative association of those features with the LSED in the area (Table 5.5). This is difficult to imagine given the apparent strong relationship of LSED with regional scale fracture systems, the strong evidence provided by the Fry analysis and the presence of vein systems with those orientations such as in the northwest part of Cerro Vanguardia mine, in Manantial Espejo and in Bacon-Mina Marta.

Table 5.5: WofE calculations only inside areas of favorable lithology (Pre-Bajo Grande Formations). Note the negative values of W^+ and C obtained for the set of structures with azimuth orientations of 105-125°.

Binary evidence map (buffer class)	Pixels of binary presence	Pixels of binary presence with deposits	W^+	W	C	$SigC$
Clay alteration	10028	32	0.6667	-0.6797	1.3464	4.3937
Structures-145a170_0	1513	8	1.1739	-0.1294	1.3032	3.3571
Structures-145a170_4000	7562	24	0.6613	-0.3946	1.0559	3.6538
Structures-145a170_6000	10374	28	0.4988	-0.4381	0.9369	3.1974
Structures-145a170_8000	13081	33	0.4310	-0.5712	1.0022	3.2162
Structures-145a170_10000	15545	37	0.3727	-0.7162	1.0889	3.1690
Structures-145a170_12000	17681	39	0.2965	-0.7475	1.0440	2.8215
Structures-145a170_14000	19569	39	0.1948	-0.5693	0.7640	2.0649
Structures-145a170_16000	21276	40	0.1364	-0.4931	0.6294	1.6242
Structures-145a170_18000	22711	42	0.1198	-0.5825	0.7024	1.6085
Structures-145a170_20000	23878	42	0.0696	-0.3859	0.4555	1.0432
Structures-105a125_0	3287	4	-0.2993	0.0322	-0.3315	-0.6344
Structures-105a125_2000	9623	11	-0.3619	0.1389	-0.5008	-1.4574
Structures-105a125_4000	14822	17	-0.3586	0.2699	-0.6284	-2.0808
Structures-105a125_6000	18985	28	-0.1068	0.1717	-0.2785	-0.9505
Structures-105a125_8000	21930	32	-0.1175	0.2868	-0.4043	-1.3191
Structures-105a125_10000	23576	35	-0.1002	0.3338	-0.4340	-1.3349
Structures-105a125_12000	24909	39	-0.0469	0.2334	-0.2804	-0.7574
Structures-105a125_14000	26072	41	-0.0425	0.2938	-0.3363	-0.8215
Structures-105a125_16000	26953	43	-0.0281	0.2814	-0.3096	-0.6545
Structures-105a125_18000	27592	45	-0.0061	0.0956	-0.1016	-0.1703
Structures-105a125_20000	28028	46	0.0003	-0.0058	0.0061	0.0084
Total pixels = 29254			Total pixels with deposits = 48			

5.2.2. Regional scale prediction of mineralized zones

The prior probability of LSED, the prior odds of LSED, and the Logits were calculated from equations 5-1, 5-4 and obtaining the following values:

$$\text{Prior Probability} = 0.0006777 \quad \text{Prior Odds} = 0.0006782 \quad \text{Logit}\{D\} = -7.2961307$$

These values and the binary predictor maps were used to generate regional scale posterior probability maps of the area. Initially, a posterior probability map was generated using the four original predictor maps with values from Table 5.3. The predicted number of deposits in the resulting posterior probability map is 60, which was calculated using equation 5-24. This is 25 % higher than the number of observed deposits (i.e., 48) and therefore, it indicates that assumption of conditional independence is violated. This was already inferred from the X^2 values in the pairwise tests that included the map of structures with azimuth orientations of 105-125°. In addition, weights and contrasts calculated under the other situation (i.e. inside areas of favorable lithology) showed small negative values. These were indications that suggested that the evidence map representing those structures was problematic or indicative of a negative association, which is difficult to explain at the present level of understanding of the controlling factors on the mineralization in the area. Therefore, that map was excluded from the predictive mapping. The three remaining binary predictor maps were combined to produce a regional scale posterior probability map for LSED in the Deseado Massif (Fig. 5.6).

The posterior probability map shown in Fig. 5.6 was analyzed by an overall test for conditional independence and the predicted number of deposits is 56 (Table 5.6); this is 16.6 % higher than the

observed number of deposits and is very close to the accepted threshold of 15%; therefore, this map was accepted as statistically valid.

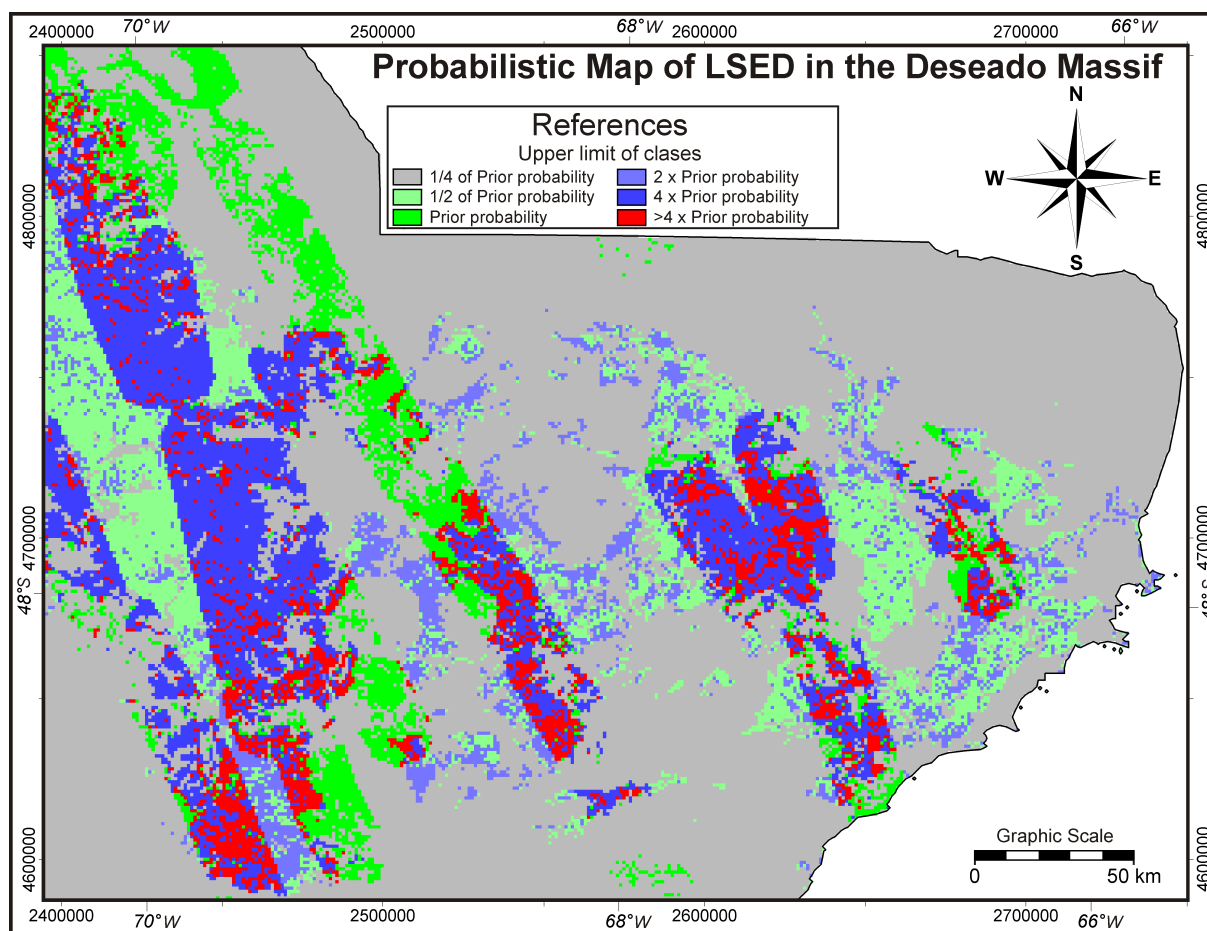


Fig. 5.6: Regional posterior probability map for LSED of the Deseado Massif generated by combination of lithological, alteration and structural evidences through weights of evidence method. Blue and red colors indicate posterior probabilities higher than the prior probability.

Table 5.6: Result of overall test of conditional independence for posterior probability map shown in Fig. 5.6.

Probability Values in map	Number of pixels (npix)	Predicted number of deposits
0.00003	21288	0.59
0.00010	12596	1.27
0.00016	8914	1.40
0.00033	6598	2.20
0.00057	4799	2.75
0.00121	3966	4.80
0.00189	8881	16.77
0.00683	3783	25.86
TOTAL	70825	55.64

Later, the posterior probability map generated using lithology, clay alteration and structures with azimuth orientations of 145-170° was thresholded into a binary map of LSED potential based on the

value of prior probability. Areas with posterior probability greater than the prior probability are considered as favorable zones for exploration for LSED (Fig. 5.7). Ten LSED of lower exploration importance than those used for prediction were used to validate the mineral potential map. Each of validation deposits were represented as a one unit cell in a raster map; then the raster map was crossed with the LSED potential map to know the number of training and validation LSED delineated in the favorable zones.

Of the 48 LSED used to generate the regional scale predictive model, 38 are delineated by the predicted favorable zones. On the other hand, all 10 validation LSED are delineated by the predicted favorable zones. Thus, the regional scale predictive model has only about 80 % success rate but has 100 % prediction rate. This implies that the 38 training LSED and the 10 validation LSED delineated by the predicted favorable zones have similar regional scale spatial characteristics and that the predictive model is useful for guiding exploration for LSED of similar regional spatial characteristics.

At regional scale, the prior probability of LSED in the area was augmented up to more than four times in 5.34% of the total area. In the favorability map, 23.5 % of the area has posterior probabilities higher than the prior probability, and therefore, suggest good potential for LSED discoveries. The area to consider for exploration is thus reduced from 70,828 km² to 16,630 km².

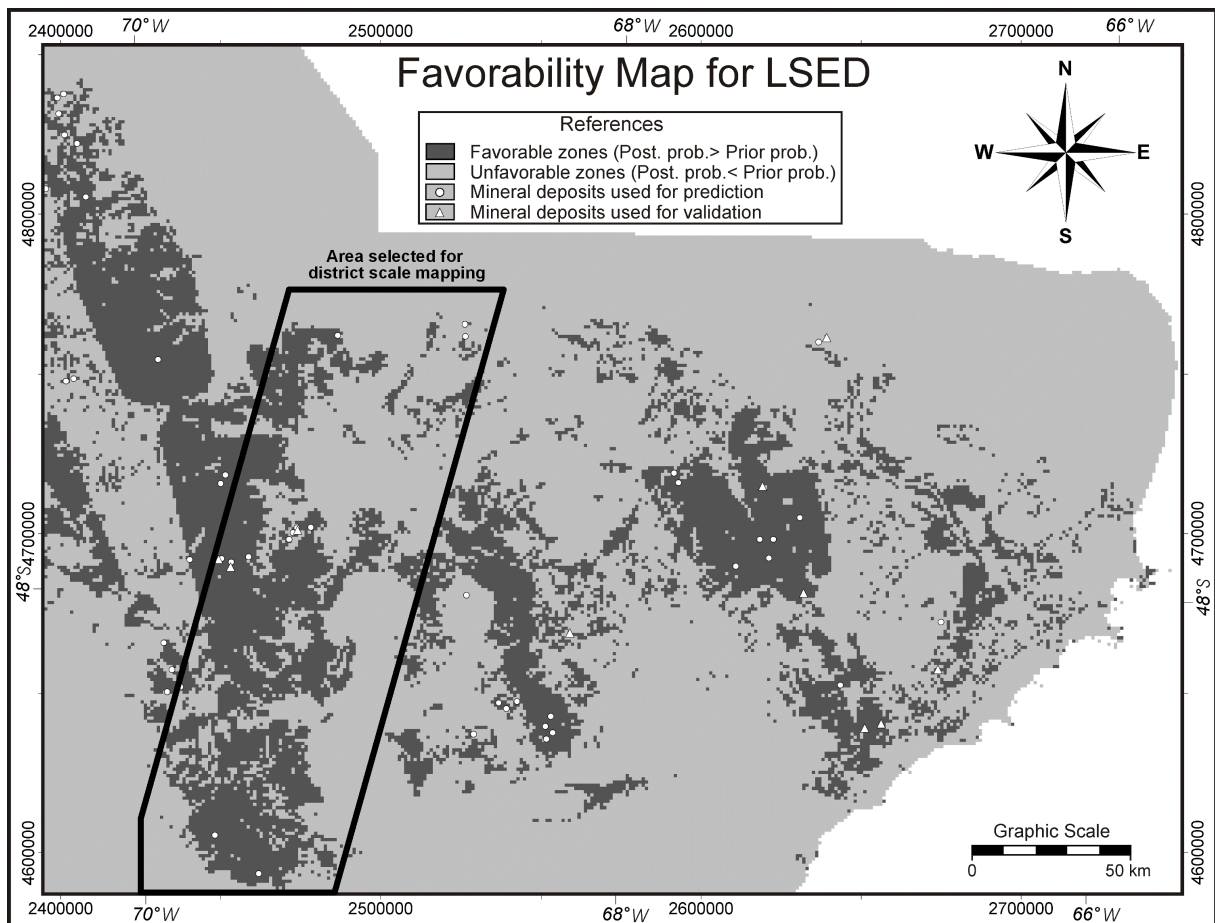


Fig. 5.7: Binary regional LSED favorability map. The set of mineral deposits used for prediction and the set used for validation are overlaid on the favorability map. The area in the slanted box was selected for district scale mapping of LSED potential.

5.3. WofE application to district scale mapping of LSED potential

Part of the western sector of the Deseado Massif was selected for district scale potential mapping of LSED potential. The selected area comprises 15,282 km² and includes favorable zones delineated by the regional scale LSED favorability map (Fig. 5.7) The location of the area was explained in section 4.3 and can also be seen in Fig. 4.3. Thirteen mineral deposits from the total set of 48 deposits, were used during the district scale potential mapping.

5.3.1. Spatial association of LSED with district scale geological features

Four evidence maps and a LSED map, resampled to a unit cell size of 100x100 m, were used to study the spatial association between LSED, lithology, structure, and alteration minerals.

The evidence map for lithology consisted of Pre-Permian, Bajo Pobre, Chon Aike and La Matilde Formations (Pre-Bajo Grande Units) and undifferentiated younger Formations. They were extracted from the geological map of Fig. 4.3.

Two evidence maps represent the alteration. One alteration map was derived from a band ratio 4/6 and represents clay alterations, including probably illite, smectites (montmorillonite) and kaolinite. The other alteration map was derived from a K-silica index image and is likely to represent silica abundance. After appropriate thresholds were applied to both 4/6 ratio and K-silica images, areas with and without clay alteration and with high or low silica content respectively, were buffered outwards in steps of 200 m up to 600 m (Fig. 5.8a, b). The reason for this is that many deposits are not located exactly over the areas with strongest argillic or silicic alterations but at some distance from them because of the configuration of the fracture system that lead to the generation of deposits and their related alterations, or because of lateral migration of the hydrothermal fluids through permeable strata.

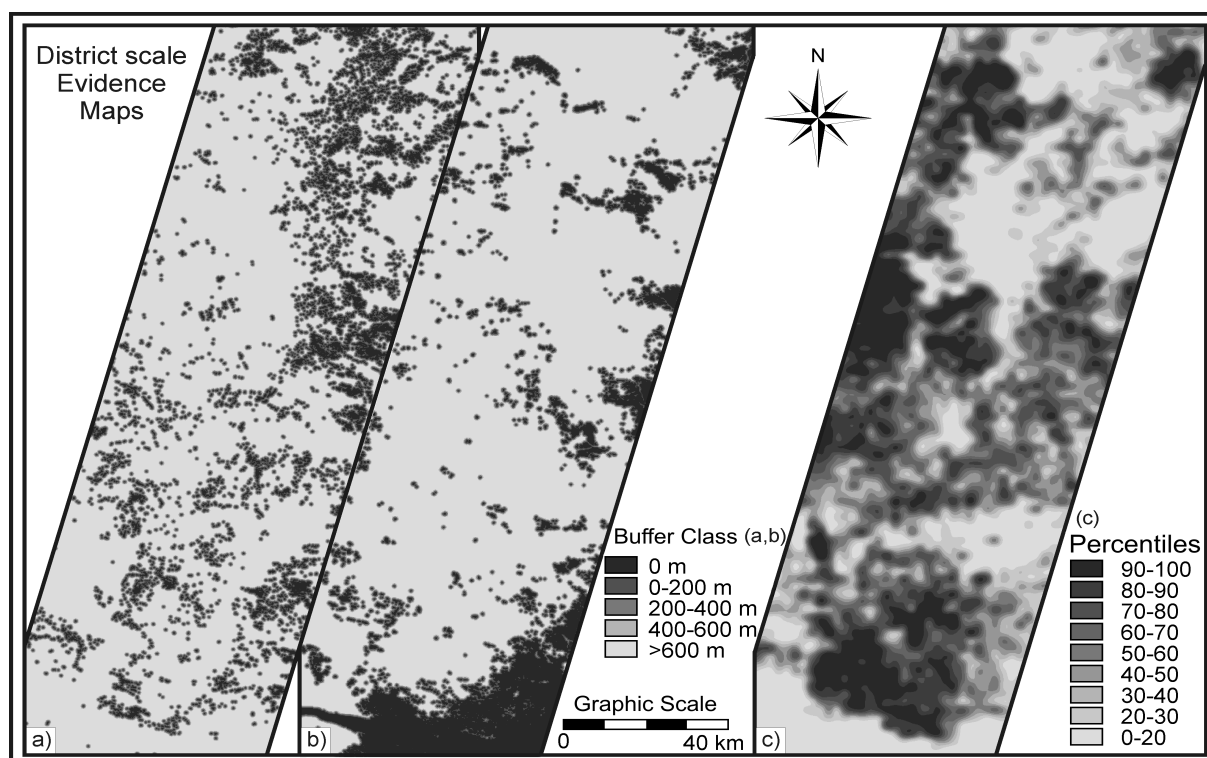


Fig. 5.8: Evidence maps used for district scale WofE modelling. (a) Clay alteration map and (b) K-silica index map were buffered in steps of 200 m up to 600 m. (c) Density sliced map of density of lineaments; density classes were determined using percentiles.

A map of density of lineaments represents the structural evidence, which is in part likely to represent differences in secondary permeability of the rocks. The original map of density of lineaments produced in chapter 4 was classified using percentile classes (Fig. 5.8c). The resultant map was used in the spatial association analysis.

Five maps were used to calculate weights and contrasts, including maps of: (1) Bajo Pobre Formation, (2) Chon Aike Formation; (3) clay alteration; (4) silica abundance; and (5) density of lineaments. After the calculations and selection of buffer intervals or classes, binary weight (predictor) maps were generated and conditional independence was checked by the pairwise test. Pairs that included the map of Bajo Pobre Formation produced high X^2 values, so that map was excluded from the posterior probability map calculation.

Initially, calculation of a posterior probability map was carried out with the remaining four predictor maps. In the resulting posterior probability map, the predicted number of deposits is 53, which is close to 300% higher than the 13 observed deposits used for modeling. Therefore, the initial posterior probability map is statistically not acceptable.

After other map combinations were tested, the one that produced the best results from the overall conditional independence test was selected for the mineral predictive mapping at district scale. The best predictive modeling was carried out only inside the areas of favorable lithologies, which include the four pre-Bajo Grande Formations. The maps of clay alteration, silica abundance and density of lineaments used to predict LSED in that areas of favorable lithologies, were first masked with the favorable lithology map, and then classified using percentile classes (Fig. 5.9).

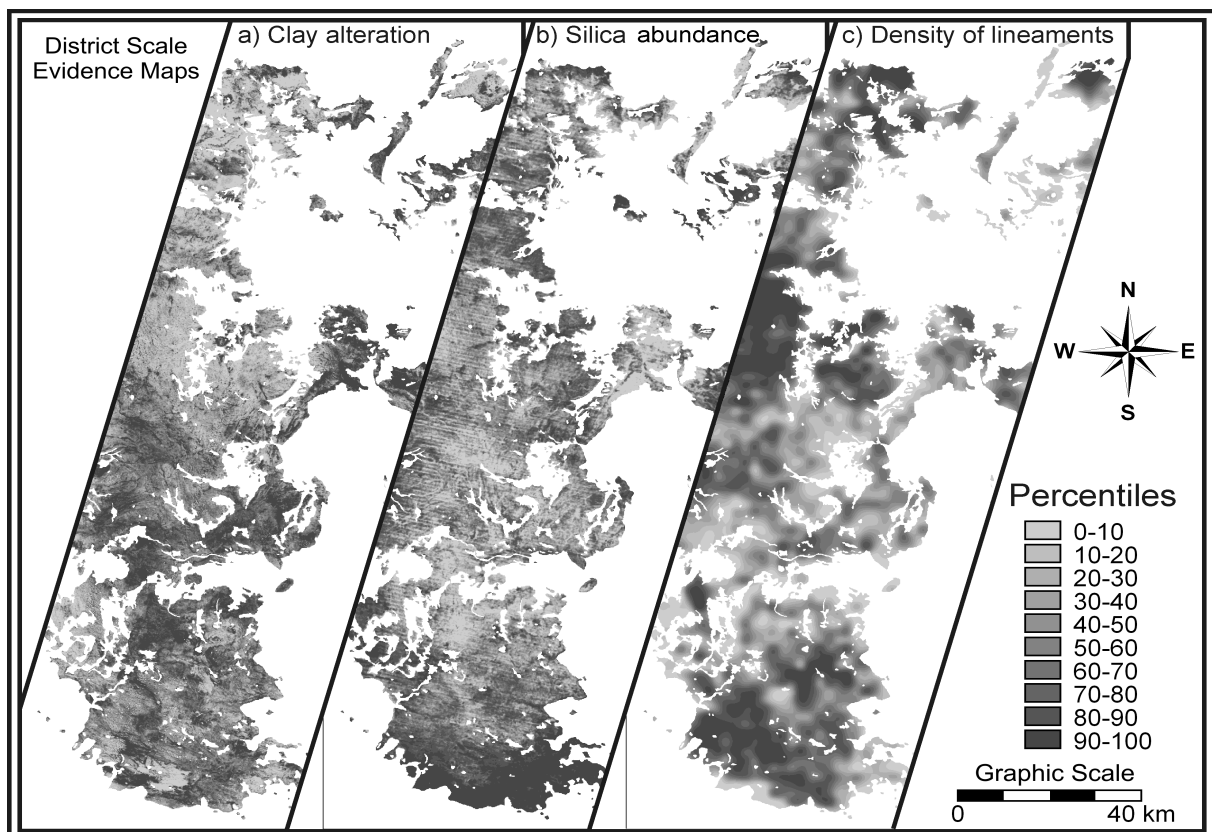


Fig. 5.9: Evidence maps used for district scale WofE modelling only inside areas of favorable lithology. Clay alteration map (a), silica abundance map (b) and density of lineaments map (c) were classified using percentile classes.

Presented in Table 5.7 are the weights and contrast values calculated for each of the cumulative classes of the evidence maps shown in Fig. 5.9. The optimum spatial association of each evidence

map with the LSED was determined based on the contrast and Studentized contrast values and binary predictor maps were generated by applying the correspondent W^+ and W^- to the patterns present and absent respectively (Fig. 5.10). Binary predictor maps of density of lineaments and K-silica index, were created based on cumulative percentile class 70-80 %, while the binary predictor map for clay alteration was created based on percentile class 90-100 % (Table 5.7).

The results of the pairwise test of conditional independence for binary predictor maps are presented in Table 5.8. The chi-square values for all pairs of maps are well below the 3.84 critical value for one degree of freedom at the 95% confidence level. Therefore, the three maps were used during following calculations.

Table 5.7: Calculation of weights and contrasts only inside areas of favorable lithology. Bold italics indicate the selected threshold cumulative classes to create binary predictor maps.

Binary evidence map	Pixels of binary presence	Pixels of binary presence with deposits	W^+	W^-	C	$SigC$
DensityLin_90-100	55546	5	1.3011	-0.3749	1.6761	2.9399
DensityLin_80-90	107852	8	1.1076	-0.7282	1.8358	3.2202
<i>DensityLin_70-80</i>	<i>164029</i>	<i>12</i>	<i>1.0938</i>	<i>-2.1951</i>	<i>3.2888</i>	<i>3.1598</i>
DensityLin_60-70	215509	13	0.9008	-	-	-
DensityLin_50-60	270083	13	0.6751	-	-	-
DensityLin_40-50	319081	13	0.5084	-	-	-
DensityLin_30-40	372812	13	0.3527	-	-	-
DensityLin_20-30	427731	13	0.2153	-	-	-
DensityLin_10-20	479396	13	0.1013	-	-	-
DensityLin_0-10	530493	13	0000	-	-	-
KIndex_90-100	56229	3	0.7781	-0.1503	0.9284	1.4103
KIndex_80-90	113762	6	0.7665	-0.3777	1.1442	2.0566
<i>KIndex_70-80</i>	<i>173965</i>	<i>10</i>	<i>0.8526</i>	<i>-1.0690</i>	<i>1.9216</i>	<i>2.9191</i>
KIndex_60-70	223683	11	0.6965	-1.3242	2.0208	2.6288
KIndex_50-60	279912	13	0.6394	-	-	-
KIndex_40-50	337884	13	0.4511	-	-	-
KIndex_30-40	394871	13	0.2953	-	-	-
KIndex_20-30	440142	13	0.1867	-	-	-
KIndex_10-20	487112	13	0.0853	-	-	-
KIndex_0-10	530493	13	0.0000	-	-	-
<i>Ratio4ov6_90-100</i>	<i>58939</i>	<i>5</i>	<i>1.2419</i>	<i>-0.3677</i>	<i>1.6096</i>	<i>2.8233</i>
Ratio4ov6_80-90	118445	6	0.7262	-0.3664	1.0926	1.9638
Ratio4ov6_70-80	170284	7	0.5173	-0.3861	0.9034	1.6238
Ratio4ov6_60-70	238524	7	0.1803	0.1760	0.3563	0.6405
Ratio4ov6_50-60	284183	8	0.1387	-0.1883	0.3270	0.5736
Ratio4ov6_40-50	337246	9	0.0853	-0.1688	0.2541	0.4228
Ratio4ov6_30-40	392906	10	0.0379	-0.1168	0.1547	0.2349
Ratio4ov6_20-30	438807	10	-0.0726	0.2891	-0.3617	-0.5495
Ratio4ov6_10-20	488691	12	0.0020	-0.0241	0.0261	0.0251
Ratio4ov6_0-10	530493	13	0.0000	-	-	-
Total pixels = 530493			Total pixels with deposits = 13			

Table 5.8: Values of X^2 obtained in pairwise test of conditional independence for district scale mapping.

	K-silica Index	Density of Lineaments
Clay Alteration	0.04	1.73
K-silica Index		0.32

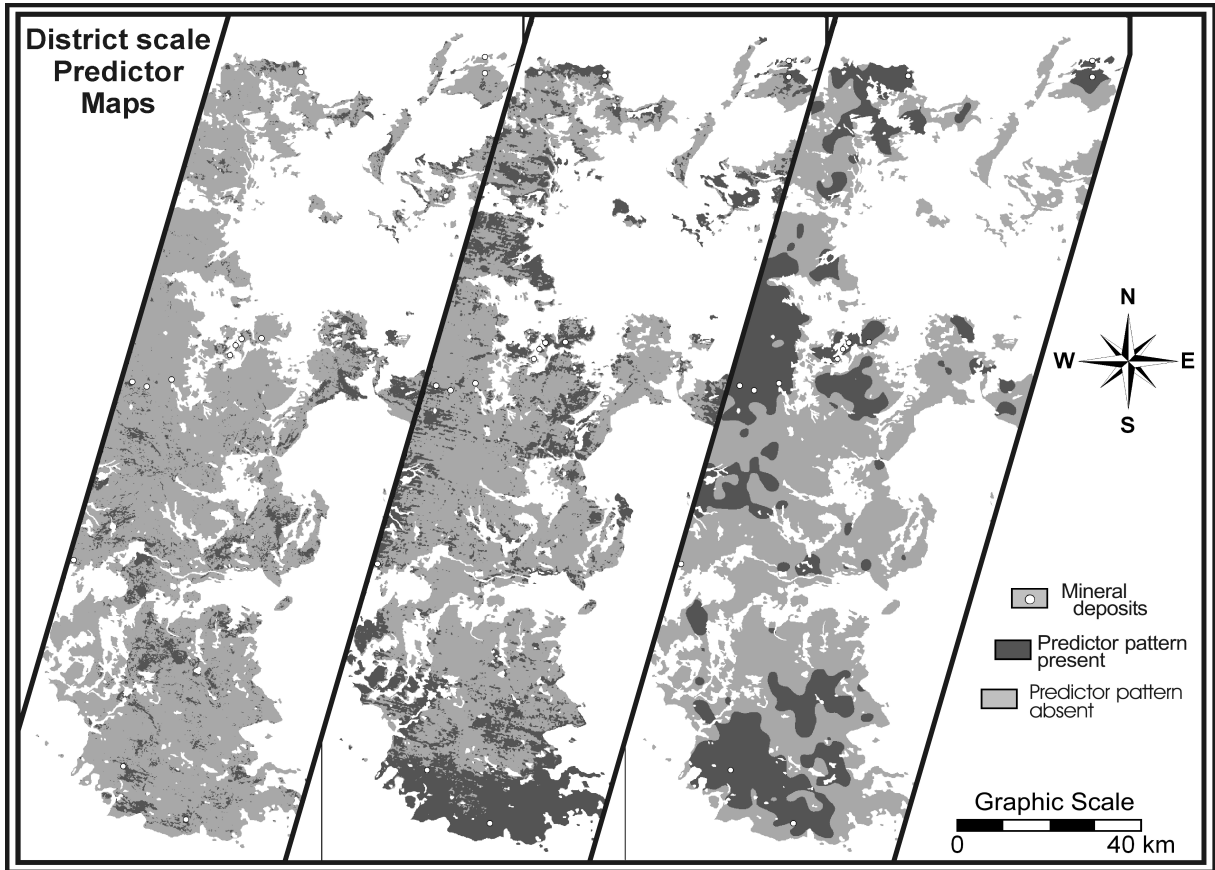


Fig. 5.10: Binary predictor maps (weight maps) used for the district scale potential mapping. **a)** Map of clay alteration. **b)** Map of silica abundance. **c)** Map of lineament density.

5.3.2. District scale prediction of mineralized zones

Values of prior probabilities, prior odds and $\text{Logit}\{D\}$ for the district scale predictive mapping were calculated and are as follows:

$$\text{Prior probability} = 0.000024505 \quad \text{Prior odds} = 0.000024506 \quad \text{Logit}\{D\} = -10.616588178.$$

Using these values and the binary predictor maps (Fig. 5.10), a posterior probability map was generated and then reclassified in five classes in relation to the prior probability (Fig. 5.11a). For the posterior probability map, the predicted number of LSED in the area covered by the favorable lithology is 14, which is only 7.6 % higher than the observed number of deposits (Table 5.9). This shows that the resultant posterior probability map is not in violation of conditional independence assumption.

A favorability map, in which areas with values higher than the prior probability are indicated as favorable areas, was made (Fig. 5.11b). In this map, only areas inside the favorable lithological formations are classified. The map was later validated using three deposits of less category than those used for the prediction because of the lack of more known mineral deposits.

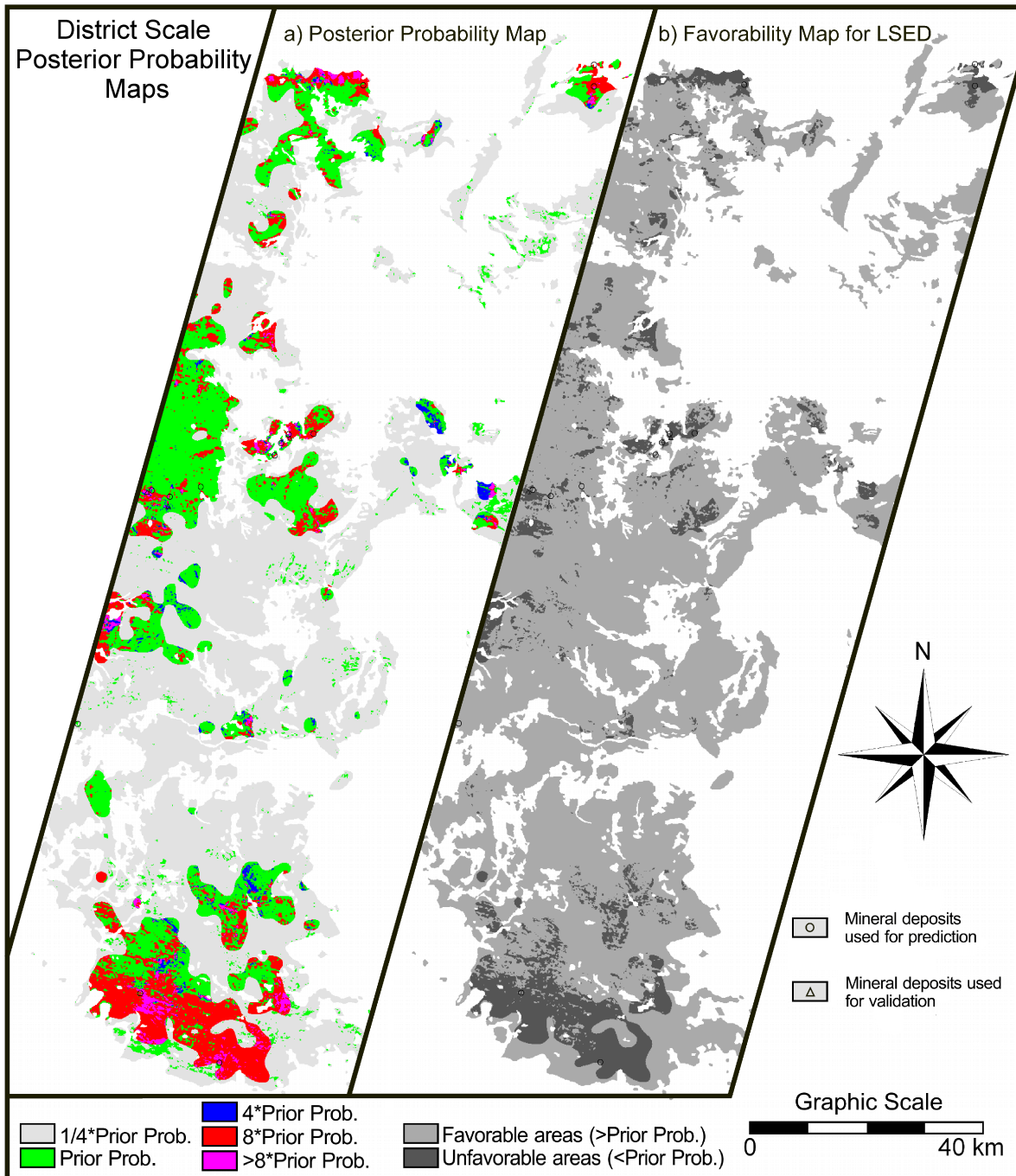


Fig. 5.11: Classified district scale LSED posterior probability map (a) and classified favorability map (b). Mineral deposits used for prediction and validation are overlaid.

Of the 13 deposits used to generate the district scale predictive model, 10 are delineated by the predicted favorable zones. On the other hand, all three validation LSED are delineated by the predicted favorable zones. Thus, district scale predictive model has about 77% success rate but has 100% prediction rate. This implies that the 13 training and 3 validation LSED have similar district scale spatial characteristics and that the predictive model is useful to guide exploration for similar LSED.

At district scale, the total area selected of 12,310 km² was first reduced to 5,304 km² (43 % of the area) by considering only the favorable lithology. Later by application of WofE, the area of favorable lithology was reduced to 671 km² (12.6% of favorable lithology area) as area with high potential for LSED. Therefore, 94.6 % of the selected district scale area can, in principle, be considered as

unfavorable. Only 671 km² can be considered as favorable for LSED. The prior probability of LSED in the area was increased up to more than four times in 11.5 % of that area.

Table 5.9: Result of overall test of conditional independence for posterior probability map shown in Fig. 5.11a.

Probability value in map	Number of pixels	Number of deposits predicted
0.0000006	219203	0.14
0.0000032	34368	0.11
0.0000044	101372	0.45
0.0000174	96919	1.69
0.0000222	11521	0.26
0.0000870	6038	0.53
0.0001188	54060	6.42
0.0005938	7012	4.16
TOTAL	530493	13.76

5.4. Discussion and concluding remarks

In this chapter, mineral potential mapping by weights-of-evidence method was carried out to predict potential for LSED in the Deseado Massif at regional and district scales. At both scales, the employed evidences were of the same types: lithological, structural and mineral alteration. However, a different dataset representing different geological features, which were derived from the results of chapter 4, were used for each scale of mapping. Few tests were carried out with each dataset corresponding to each scale of mapping to find the best map combinations to generate probabilistic maps of each study area.

For regional scale mapping, the best map combination consisted of: (a) a map of lithological evidence with Chon Aike, La Matilde and Bajo Pobre Formations combined; (b) a map of clay alteration derived from band ratio 5/7 of Landsat data; and (c) a map of regional structures with orientation 145-170° buffered in steps of 2000 m. A second map of regional structures with orientation 105-125° was rejected because it produced violation of the conditional independence assumption and apparent lack of spatial association with the LSED. This means that those structures are not related to mineralization at that scale or that the evidence map generated from digitization was not appropriate.

The values of contrast obtained for the three predictive patterns used in the regional scale prediction, show high statistical significance (*SigC*) and the weights and contrasts are relatively high. From the weights obtained it could be interpreted that lithology is the strongest predictor, and the relatively high absolute value of *W*- indicates that absence of favorable lithology precludes presence of LSED, which is validated by the fact that most of the lithologies mapped as unfavorable are younger than the mineralization and therefore, sterile. The lowest weights correspond to the clay alteration evidence (Table 5.3), which mean poor spatial association between mapped clay alteration and LSED. This apparent poor association could be because (a) some areas mapped as clay alteration are probably unrelated to mineralization or (b) alteration halos around many small deposits are not large enough to be detected from Landsat images

For district scale mapping, the best results of WofE was achieved by predicting LSED potential inside the area of favorable lithology (Pre-Bajo Grande Formations) using maps of lineament density, of clay alteration (ASTER band ratio 5/6) and silica abundance (K-silica index). The binary predictor patterns derived from each of the three evidence maps were classified according to the percentile classes. This method of map classification, using percentile classes, and weighting every class to decide which cumulative interval to use in creating a binary predictor pattern, was proven to be successful for the district scale mapping.

The selected cumulative classes show high statistical significance, contrasts and weights (Table 5.7). The values of $W+$ for all predictor patterns are similar; however, values of $W-$ are slightly different. The high absolute $W-$ values for the map of lineament density could indicate that low-density areas (indicative of low fracturing and low overall permeability) are less favorable to mineralization, which agrees with the strong structural controls on most LSED. The low absolute $W-$ values for the clay alteration evidence could be due, as in the case of regional scale, to the presence of small clay alteration halos produced by these deposits, which may not be detected by the used methods.

The technique of eliminating areas underlain by lithologies with no possibilities of hosting the deposit type being sought (rocks younger than mineralization) and then calculating weights-of-evidence to predict only in the lithologically favorable areas proved to be successful at district scale in this research. However, it has to be considered that a few meters thick layers of young gravels and basalts cover some areas and thus mask underlying favorable lithologies. Some of these areas can still be indicated as favorable because of the presence of other evidences (regional structures in this case). Therefore, it is probably better to use the whole area to make predictions at regional scale. Covered areas indicated in the regional scale mapping just by structural evidences and do not show high posterior probabilities might be also highly favorable and should not be prematurely discarded.

The practical significance of the regional scale and district scale predictive mapping of mineral potential presented in this chapter, can be deduced by comparing predicted regional and district scale favorable and unfavorable zones. The comparison was done for the area of favorable lithology of the district scale study area and results are presented in a confusion matrix (Table 5.10) derived from a cross operation of favorability maps at both scales.

Table 5.10: Confusion matrix derived from cross operation of regional scale and district scale favorability maps to compare results of potential mapping at both scales in zones of favorable lithology in the district scale area. Values in the matrix are number of 100x100m pixels.

		District scale map		TOTAL	
		Favorable	Unfavorable		
Regional scale map	Favorable	59796	393404	453200	85.43 %
	Unfavorable	7314	69979	77293	14.57 %
TOTAL		67110	463383	530493	
		12.65 %	87.35 %		

Both mapping scales showed different area reductions. The regional scale mapping delineates 85.43% of the district scale study area as favorable (i.e., $453200 \div 530493 \times 100$), while district scale mapping delineates 12.65% of the same area as favorable (i.e., $67110 \div 530493 \times 100$). About 87% of the regional scale favorable areas were mapped as unfavorable by the district scale mapping (i.e., $393404 \div 453200 \times 100$). In addition, only about 11% (i.e., $7314 \div 67110 \times 100$) of the district scale favorable zones were mapped as unfavorable by the regional scale mapping. Therefore, district scale potential mapping in favorable areas already delineated by regional scale mapping seems a reasonable practice to sequentially constrict exploration efforts. The results of comparing the regional scale predictive map with the district scale predictive map are consistent with the general approach carried out during mineral exploration to narrow down favorable areas by working first with small scale zones and focusing later in larger scale zones. This information demonstrates usefulness of application of regional and district scales of mineral potential mapping to focus or guide efforts in exploration for LSED.

CHAPTER 6: Conclusions and Recommendations

6.1. Conclusions

6.1.1. Geological controls of LSED in Deseado Massif

Literature reviews about LSED worldwide and in the Deseado Massif together with an exploratory Fry analysis of point pattern distribution were used to deduce the geological controls for LSED in the area and to determine the deposit recognition criteria to be used later for mineral potential mapping at regional and district scales.

From literatures of previous works in the study area and descriptions of mineral occurrences, it can be concluded that:

- The gold-silver mineralizations in the Deseado Massif are of the low-sulfidation epithermal type and they show highly similar spatial characteristics, so as to establish deposit recognition criteria that can be applied for predictive modelling of LSED potential in the whole area.
- Most of the mineralizations in the Deseado Massif seem to have been controlled by NNW-SSE trending fractures, produced during the rifting process that ended with the opening of the Atlantic Ocean, and probably partially by subsequent WNW-ESE transcurrent faults. These fracture systems may have acted as hydrothermal fluid pathways. However, the directions of fracturing in the area are complex, with stresses coming initially from the NNW and then rotated in several stages to the SSW; therefore, the relationship between fracturing and mineralization is complex. This complexity is accentuated by the migration of volcanism fracturing and probably of mineralization in time from ENE to WSW.
- The rocks of the Bahía Laura Group and probably those of Bajo Pobre Formation have to be considered as the main host rocks, while rocks younger than the Bahía Laura Group can be considered sterile. Silica related alterations (quartz veins, silica sinters and silicified rocks) and clay alterations that form small envelopes of illite, illite-smectite and some kaolinite around veins, are the two main types of hydrothermal alterations related to the mineralizations in the area.

From the Fry analyses of spatial distribution patterns of known LSED in the study area, it can be concluded that:

- Fracture systems were principal controls on spatial distribution of LSED in favorable lithologies in the study area. The spatial distribution of the LSED in the western half and eastern half of the study area were partially controlled by different fracture systems.
- In the western half, there is apparent stronger control on the spatial distributions by fracture systems with NW trends. In the western half, fracture systems with orientations 145-170°, which correspond with the El Tranquilo system, other fractures with orientation 160-170° and fracture systems with orientations 105-125°, which correspond with Bajo Grande system, were pointed out by the Fry analysis as the strongest controlling fracture systems. In the eastern half, there is apparent stronger control by fracture systems with NE trends, while the NW trends are weaker controls.
- The apparent differences in strengths in structural controls on spatial distribution of LSED in the western half and in the eastern half may be due to the proposed migration of fracturing and mineralization in the Deseado Massif.

6.1.2. Mapping of geological features indicative of LSED

From the mapping of geological features indicative of LSED, the following conclusions are made:

- Simple band ratios (5/7 for Landsat and 4/6 for ASTER) proved to be more suitable methods than principal component analytical techniques to map clay alterations at regional to district scales using Landsat and ASTER data.
- A great advantage of using ASTER over Landsat data is the ability to map silica abundance, which is an important indicator for LSED in the Deseado Massif. Despite other evidences used at both mapping scales, this can be inferred from the greater focusing over favorable areas produced by the district scale predictive mapping that includes silica, in comparison with the regional scale predictive mapping that only includes clays.
- The use of shaded relief images derived from a DEM was useful to extract regional scale fracture zones. Landsat color composites combined with shaded relief images generated from band 7 of the same sensor were found useful to interpret and digitize lineaments for district scale predictive mapping.

6.1.3. Predictive mapping of LSED potential

Weights-of-evidence modelling was applied to (a) quantify spatial associations between the LSED and each of the spatial evidences and (b) generate predictive models of regional and district scale potential for LSED. From this stage of the research, the following conclusions are made:

- Lithology is a very important control on emplacement of LSED and is indicated to be the strongest spatial predictor at regional scale. The relatively strong negative values of W - in the spatial association analysis indicate that absence of favorable lithology precludes presence of LSED, which is validated by the fact that most of the lithologies mapped as unfavorable are younger than the mineralization and therefore, sterile. However, from the Fry analysis it was concluded that fracture systems principally controlled the spatial distribution of the LSED in the favorable lithologies.
- The spatial association analysis and predictive mapping indicate importance of fracture systems with orientations 145-170°. This set of fractures has intermediate positive spatial association with LSED at regional scale after the lithological features.
- The 105-125° fracture system shows lack of spatial association with the LSED. However, due to strong indications from the Fry analyses, it is probable that the available data from which spatial evidences of this fracture systems were extracted were not adequate and probably a different source of information is needed, such as aeromagnetic data.
- Clay alteration showed spatial contrast values that are lower than the other spatial evidences at both scales of mapping. This shows that the spatial association of clay alteration and LSED is relatively poor, which could be explained by three possible reasons: (a) some areas mapped as clay alteration are probably unrelated to mineralization; (b) some alteration halos are not large enough to be detected with the RS data used; or (c) because of the large cell sizes used at district and mainly at regional scale mapping, small clay alteration halos are not well represented in the evidence maps.
- At regional scale, presence of fracture zones with orientations at azimuths 145-170°, presence of Chon Aike, La Matilde and Bajo Pobre Formations and presence of clay alteration extracted from Landsat Images can be used to successfully produce a mineral potential map of LSED by using a WofE approach. The mineral potential mapping at regional scale shows that 23.5% of the area has posterior probabilities of LSED occurrence higher than the prior probability, and therefore, suggests good potential for LSED discoveries. The prior probability of LSED in the area was augmented up to more than four times in 5.34 % of the total area.

The regional scale predictive model has a success rate of 80% and prediction rate of 100%. The area to consider for exploration has been reduced from 70,828 km² to 16,630 km².

- At district scale, lineament density is a very good predictor with strong positive spatial association with the LSED in the area, which demonstrates the overall importance that rock fracturing and, hence, overall rock permeability have on emplacement of LSED.
- At district scale, density of lineaments, presence of pre-Bajo Grande Formations, presence of clay alteration and abundance of silica content are useful spatial evidences for mineral potential map of LSED by using a WofE approach. The elimination of areas covered by rocks younger than the mineralization proved efficient at this scale to predict LSED potential. The district scale predictive model shows that 12.6 % of areas of favorable lithology (which represent only 5.4% of the total district scale area) have posterior probabilities higher than the prior probability, and therefore, suggests good potential for LSED discoveries. The total district scale area of 12,310 km² was first reduced to 5304 km² by considering only those sections underlain by favorable lithology and then to 671 km² by application of WofE method. The prior probability of LSED in the area covered by favorable lithology was increased up to more than four times in 11.5 % of that area by integration of spatial evidences. The district scale predictive model has a success rate of 77% and a prediction rate of 100%.
- The weights-of-evidence method was proven successful to generate mineral predictive maps and useful to investigate the spatial associations of LSED with lithology, structures and hydrothermal alteration as well as to infer some information related to the genesis of the LSED in the Deseado Massif.
- District scale potential mapping in areas delineated by the regional scale potential map, is a good practice to sequentially concentrate exploration efforts, and is in accordance with the general approach carried out during mineral exploration to constrict favorable grounds by working first with small scale zones and later focusing in larger scale zones. This information demonstrates the usefulness of the application of both scales of mineral potential mapping in focusing efforts during the process of exploration for LSED.

6.2. Recommendations

For future exploration for LSED in the study area, efforts should be oriented towards two main objectives: (1) consider results obtained in this research to improve effectiveness of LSED exploration programs; and (2) update and improve predictive models created during this work as well as knowledge about geological controls on mineralization (mainly structural) with new information especially acquired for that purpose and/or information that becomes available by other ways.

Areas that are free of mineral rights and indicated to have high posterior probabilities for LSED by the regional and district scale potential maps should be considered in planning for future exploration activities. Areas not predicted as favorable by the regional scale probability maps but show presence of regional scale fractures and are covered/masked by layers of younger gravels or basalts could be underlain by favorable lithologies and they could have potential for LSED. Therefore, they should not be prematurely discarded.

The map of LSED occurrences used to build the predictive models should be updated with data from new discoveries or existent data when they are released to the public. This is important mainly to improve the district scale predictive models and to analyze local controls on mineralization.

The predictive models could be improved by deeper analysis of structural controls on mineralization. New studies should be executed to analyze structural controlling factors in the eastern and western sectors of the Deseado Massif. Probably, the study of structural controls for district scale mapping would be the more useful ones in the future, when regional mapping becomes less necessary.

The lack of ground-truth hydrothermal alteration data for validation of the remotely-sensed alteration maps is a limiting factor for mineral potential mapping in the area. Therefore, field alteration mapping especially dedicated to improve the methods of alteration mapping from RS data should be carried out to improve the predictive models.

ASTER data should be acquired for the whole area and used to extract clay alteration, silica abundance and lineament maps. The reason for this is because, in comparison with Landsat, ASTER has a better spectral resolution in the SWIR and TIR regions and higher spatial resolution in the VNIR region. In addition, the atmospherically corrected products can be relatively easy to acquire.

Aeromagnetic data are likely to provide structural information and thus when available should be interpreted for structural analysis to improve the regional scale predictive model. Therefore, the acquisition of aeromagnetic data to cover the whole area should be an objective of the local Government.

References

- Agterberg, F. P., Bonham-Carter, G. F. and Wright, D. F., 1990, Statistical pattern integration for mineral exploration, in Gaál, G., and Merriam, D. F., eds., *Computer Applications in Resource Estimation*: Oxford, Pergamon Press., p. 1-21.
- Allison, I., de Paor, D. G., Haszeldine, S., Bowman, A. and Maguire, M., 1997, Cryptic structural trends in basement revealed by Patterson diagrams: Examples from the Scottish and Irish Caledonian orogen., in Sengrupa, S., ed., *Evolution of the geological structures in micro-to macro-scales.*: London, Chapman and Hall, p. 487-495.
- Archangelsky, S., 1958, Estudio geológico y paleontológico del Bajo de La Leona (Santa Cruz). *Acta Geológica Lilloana*, v. 2, p. 5-136.
- Archangelsky, S., 1963, Notas sobre la flora fósil de la zona de Ticó, Provincia de Santa Cruz.: *Asociación Paleontológica Argentina, Revista*, v. 3, p. 57-63.
- Archangelsky, S., 1967, Estudio de la Formación Baqueró. Cretácico inferior de Santa Cruz.: *Revista del Museo de La Plata (Nueva Serie)*, V Paleontología, v. 32.
- Arlegui, L. E. and Soriano, M. A., 1998, Characterizing lineaments from satellite images and field studies in the central Ebro basin (NE Spain). *International Journal of Remote Sensing*, v. 19, p. 3169-3185.
- Arribas, A. J., Schalamuk, I. B., de Barrio, R., Fernández, R. and Itaya, T., 1996, Edades radiométricas de mineralizaciones epitermales auríferas del Macizo del Deseado, provincia de Santa Cruz, Argentina: XXXIX Congreso Brasileiro de Geología, Anales, Salvador, Bahia, Brasil, 1996, p. 254-257.
- Arrondo, O., 1972, Estudio geológico y paleontológico en la zona de la Estancia La Juanita y alrededores. Provincia de Santa Cruz.: *Revista del Museo de La Plata (Nueva Serie)*, Sección Paleontología, v. 7, p. 1-194.
- Asadi, H. H., 2000, The Zarshuran gold deposit model applied in a mineral exploration GIS in Iran, PhD Thesis, Delft University of Technology, Delft, The Netherlands, 190 p.
- Bishop, M. M., Feinberg, S. E., and Holland, P. W., 1975, *Discrete Multivariate Analysis: Theory and practice.*: Massachusetts, MIT Press, Cambridge. 587 p.
- Boleneus, D. E., Raines, G. L., Causey, J. D., Bookstrom, A. A., Frost, T. P. and Hyndman, P. C., 2001, Assessment method for epithermal gold deposits in northeast Washington State using weights-of-evidence GIS modeling.: US Geological Survey, Open-File Report 01-501, p. 52.
- Bonham-Carter, G. F., 1994, *Geographic information systems for geoscientists: modelling with GIS*, Pergamon, p. 398.
- Buchanan, L. J., 1981, Precious metal deposits associated with volcanic environments in the southwest.: *Arizona Geological Society, Digest* 14, p. 237-262.
- Budkewitsch, P., Newton, G. and Hynes, A. J., 1994, Characterization and extraction of linear features from digital images.: *Canadian Journal of Remote Sensing*, v. 20, p. 268-279.
- Caminos, R., Llambías, E. J., Rapela, C. R. and Parica, C. A., 1988, Late Paleozoic Early Triassic magmatic activity of Argentina and the significance of new Rb/Sr ages from Northern Patagonia: *Journal of South American Earth Sciences*, v. 1, p. 137-146.
- Carlson, C. A., 1991, Spatial distribution of ore deposits: *Geology*, v. 19, p. 111-114.
- Carranza, E. J. M., 2002, Geologically-constrained mineral potential mapping (examples from the Philippines), PhD Thesis, Delft, University of Technology, Delft, The Netherlands, 480 p.
- Carranza, E. J. M., 2003, Practical Exercise: Weights of Evidence Modeling for Mineral Potential Mapping. EREG MSc Module 6: Data Analysis and Modeling, ITC.
- Chebli, G. A. and Ferello, R., 1974, Un nuevo afloramiento metamórfico en la Patagonia extraandina.: *Asociación Geológica Argentina, Revista*, v. XXIX, p. 479-481.
- Coira, B., Nullo, F. E., Proserpio, C. and Ramos, V., 1975, Tectónica de basamento de la región occidental del Macizo Nordpatagónico (provincias de Río Negro y Chubut), Rep. Argentina.: *Asociación Geológica Argentina, Revista*, p. 361-383.
- Cooke, D. R. and Simmons, S. F., 2000, Characteristics and genesis of epithermal gold deposits: *Reviews in Economic Geology*, v. 13, p. 221-244.
- Corbett, G., 2002, Epithermal gold for explorationists: Australian Institute of Geoscientists, AIG Online Journal, p. 26.
- Corbett, G. J. and Leach, T. M., 1998, Southwest Pacific Rim gold-copper systems: Structure, alteration and mineralization: *Society of Economic Geologists Special Publication*, v. 6, p. 240.
- Crósta, A. and Moore, J. M., 1989, Enhancement of Landsat Thematic Mapper imagery for residual soil mapping in SW Minas Gerais State, Brazil: a prospecting case history in Greenstone belt terrain.: 7th ERIM Thematic

- Conference: Remote sensing for exploration geology, Calgary, Canada, 2-6 October 1989, 1989, p. 1173-1187.
- Dalziel, I. W. D., Lawver, L. A. and Murphy, J. B., 2000, Plumes orogenesis and continental fragmentation.: *Earth and Planetary Science Letters*, v. 178, p. 1-11.
- Davis, J. C., 1986, *Statistics and data analysis in Geology*: New York, John Willey & Sons 641 p.
- de Barrio, R., 1989, Aspectos geológicos y geoquímicos de la Formación Chon Aike (Grupo Bahía Laura), Jurásico medio a superior, en el noroeste de la provincia de Santa Cruz.: Tesis Doctoral N° 528 (inédito) Facultad de Ciencias Naturales y Museo, La Plata.
- de Barrio, R. E., Palma, R. M. and Panza, J. L., 1986, Deseado Massif, correlation with the Andean region.: In: *The Geologic Evolution of South America*, Servicio Geológico Nacional. Unpublished Report.
- de Barrio, R. E., Panza, J. L. and Nullo, F. E., 2000, Jurásico y Cretácico del Macizo del Deseado, Provincia de Santa Cruz., in Caminos, R., ed., *Geología Argentina*, Servicio Geológico Minero Argentino, Anales 29, p. 511-527.
- De Giusto, J. M., 1956, Informe geológico zona Roca Blanca-Baqueró: Yacimientos Petrolíferos Fiscales (inédito), p. 38.
- De Giusto, J. M., Di Persia, C. and Pezzi, E., 1980, Nesocratón del Deseado: In *Geología Regional Argentina*, Academia Nacional de Ciencias, Córdoba, v. II, p. 1389-1430.
- de Paor, D. and Simpson, C., 1987, Rf/Fry version 2.0.5 (software) instruction manual.: Boston, Earth'nWare Inc.
- Di Persia, C. A., 1956, Ibidem 3a campaña.: Yacimientos Petrolíferos Fiscales (inédito), p. 56 p.
- Di Persia, C. A., 1962, Acerca del descubrimiento del Precámbrico en la Patagonia Extraandina (Provincia de Santa Cruz). Primeras Jornadas Geológicas Argentinas, Anales 2, p. 65-68.
- Echavarría, L. and Etcheverry, R., 1999, Mineralización epitermal El Dorado-Monserrat, Macizo del Deseado, Santa Cruz., in Zappettini, E., ed., *Recursos Minerales de la República Argentina*: Buenos Aires, Instituto de Geología y Recursos Minerales, Servicio Geológico Minero Argentino, Anales 35 Tomo II, p. 1219-1224.
- Feraud, G., Alric, V., Fornari, M., Bertrand, H. and Haller, M., 1999, 40Ar/39Ar dating of the Jurassic volcanic province of Patagonia: migrating magmatism related to Gondwana break-up and subduction: *Earth and Planetary Science Letters*, v. 172, p. 83-96.
- Fernández, R. R., Echeveste, H., Echavarría, L. and Schalamuk, I. B., 1996, Control volcánico y tectónico de la mineralización epitermal del área de La Josefina, Macizo del Deseado, Santa Cruz, Argentina.: In XIII Congreso Geológico Argentino y III Congreso de Exploración de Hidrocarburos, Buenos Aires, Actas III, p. 41-54.
- Feruglio, E., 1949, Descripción geológica de la Patagonia (3 tomos). Yacimientos Petrolíferos Fiscales (inédito).
- Forsythe, R., 1982, The Late Paleozoic to Early Mesozoic evolution of Southern South America: a plate tectonic interpretation.: *Journal of the Geological Society*, v. 139, p. 671-682.
- Frutos, J. and Tobar, A., 1975, Evolution of the Southwestern continental margin of South America.: III International Gondwana Symposium, Camberra, 1975, p. 565-578.
- Fry, N., 1979, Random point distributions and strain measurement in rocks.: *Tectonophysics*, v. 60, p. 89-105.
- Giacosa, R. E., Márquez, M. M. and Panza, J. L., 2002, Basamento Paleozóico Inferior del Macizo del Deseado: In M.J. Haller (Edit.) *Geología y Recursos Naturales de Santa Cruz. Relatorio del XV Congreso Geológico Argentino*, El Calafate, I-22.
- Godeas, M. A., 1985, Geología del Bajo de La Leona y su mineralogía asociada, Provincia de Santa Cruz.: *Asociación Geológica Argentina, Revista*, v. XL, p. 262-277.
- Govett, G. J. S., 1983, *Rock Geochemistry in Mineral Exploration*, Elsevier, 461 p.
- Grove, C. I., Hook, S. J. and Paylor, E. D., 1992, Laboratory reflectance spectra for 160 minerals 0.4 - 2.5 micrometers.: *Jet Propulsion Laboratory (JPL) Publication 92-2*.
- Gupta, R. P., 1991, *Remote sensing geology*, Springer-Verlag, 356 p.
- Hanna, S. S. and Fry, N., 1979, A comparison of methods of strain determination in rocks from southwest Dyfed (Pembrokeshire) and adjacent areas.: *Journal of Structural Geology*, v. 1, p. 155-162.
- Harrington, H., 1962, Paleogeographic development of South America.: *American Association of Petroleum Geologists, Bulletin*, v. 46, n.10, p. 1773-1814.
- Hayba, D. O., Bethke, P. M., Heald, P. and Foley, K. L., 1985, Geologic, mineralogic, and geochemical characteristics of volcanic-hosted epithermal precious-metal deposits.: *Reviews in Economic Geology*, v. 2, p. 129-167.
- Hechem, J. J. and Homoc, J., 1987, La relación entre las Formaciones Baqueró and Laguna Palacios en el Nesocratón del Deseado, Provincia de Santa Cruz.: *Asociación Geológica Argentina, Revista*, v. 42, p. 244-254.
- Hedenquist, J. W., Arribas, A. R. and Gonzalez-Urien, E., 2000, Exploration for epithermal gold deposits.: *Reviews in Economic Geology*, v. 13, p. 245-277.

- Henley, R. W., and Etheridge, M. A., 1995, The structural and hydrodynamic framework for epithermal exploration.
- Herbst, R., 1965, La Flora Fósil de la Formación Roca Blanca, Provincia de Santa Cruz, Patagonia, con consideraciones geológicas y estratigráficas: *Opera Lilloana*, v. 12, p. 1-102.
- Hoffman, S. J., 1986, The Soil Survey-Designing an Exploration Program, *Exploration Geochemistry: Design and Interpretation of Soil Surveys.*, 3, Society of Economic Geologists, *Reviews in Economic Geology*, p. 19-38.
- Izawa, E., Urashima, Y., Ibaraki, K., Suzuki, R., Yokoyama, T., Kawasaki, K., Koga, A. and Taguchi, S., 1990, The Hishikari gold deposit: high-grade epithermal veins in Quaternary volcanics of southern Kyushu, Japan: *Journal of Geochemical Exploration*, v. 36, p. 1-56.
- Karnieli, A., Meisels, A., Fisher, L. and Arkin, Y., 1996, Automatic extraction and evaluation of geological linear features from digital remote sensing data using a Hough transform.: *Photogrammetric Engineering and Remote Sensing*, v. 62, p. 525-531.
- Kay, S. M., Ramos, V. A., Mpodozis, C. and Sruoga, P., 1989, Late Paleozoic to Jurassic silicic magmatism at the Gondwanaland margin: analogy to the Middle Proterozoic in North America?: *Geology*, v. 17, p. 324-328.
- Lagarde, J. L., Omar, S. A. and Roddaz, B., 1990, Structural characteristics of granitic plutons emplaced during weak regional deformation: examples from late Carboniferous plutons, Morocco: *Journal of Structural Geology*, v. 12, p. 805-821.
- Leanza, A. F., 1958, *Geología Regional, La Argentina, suma de geografía*. Tomo I, Capítulo III: Buenos Aires, Editorial Peuser, p. 217-349.
- Legg, C. A., 1994, *Remote Sensing and Geographic Information Systems: Geological mapping, mineral exploration and mining*: John Willey & Sons and Praxis Publishing LTD, p. 166.
- Lepage, R., Rouhana, R. G., St-Onge, B., Noumeir, R. and Desjardins, R., 2000, Cellular neural network for automated detection of geological lineaments on Radarsat images.: *IEEE Transactions on Geoscience and Remote Sensing*, v. 38, p. 1224-1233.
- Lesta, P. J. and Ferello, R., 1972, Región extraandina de Chubut y norte de Santa Cruz.: In: *Geología Regional Argentina*. Academia Nacional de Ciencias, p. 601-654.
- Leymarie, P., 1968, Une Méthode permettant de mettre en évidence le caractere ordonné de la distribution de gites minéraux.: *Mineralium Deposita*, v. 3, p. 334-343.
- Lillesand, T. M. and Kiefer, R. W., 2000, *Remote sensing and image interpretation.*, Wiley & Sons, 724 p.
- Lindgren, W., 1922, A suggestion for the terminology of certain mineral deposits.: *Economic Geology*, v. 17, p. 292-294.
- Lock, B. E., 1980, Flat-plate subduction of the Cape Fold Belt of South Africa.: *Geology*, v. 8, p. 35-39.
- Ludington, S., Barton Jr., P. B. and Johnson, K. M., 1985, Mineral deposit models: theory and practice (a modified version of a speech given at the first McKelvey Forum on Mineral Resources, February 6, 1985): US Geological Survey, Open-File Report 85-391, p. 18.
- Madani, A. A., 2001, Selection of the optimum Landsat Thematic Mapper bands for automatic lineaments extraction, Wadi Natash area, South Eastern Desert, Egypt.: 22nd Asian Conference on Remote Sensing, Singapore, 5-9 November 2001, 2001.
- Marchionni, D., Cavayas, F. and Rolleri, E., 1999, Potentiel de detection des traits structuraux d'un territoire semi-desertique sur des images RADARSAT: le cas du Macizo del Deseado, Argentina.: *CEOS-SAR Workshop (CNES-ESA)*, Toulouse, p. 479-484.
- Márquez, M. J., Giacosa, R. E. and Godeas, M. A., 2002, Los Granitoides gondwánicos del borde oriental del Macizo del Deseado.: In M.J. Haller (Edit): *Geología y Recursos Naturales de Santa Cruz. Relatorio del XV Congreso Geológico Argentino*, El Calafate, I-4, p. 57-70.
- Mitchell, A. H. G. and Balce, G. R., 1990, Geological features of some epithermal gold systems, Philippines: *Journal of Geochemical Exploration*, v. 35, p. 241-246.
- Miyatake, S., 2002, Regional lineament analysis and alteration mineral mapping for intrusive-related copper exploration in the Myanmar central volcanic belt.: 23rd Asian Conference on Remote Sensing (papers on-line), Katmandu, November, 2002, 2002, p. 4.
- MMAJ, 2000, Technical development report: Examination of indices for discriminating rocks and minerals and their universal validity (In Japanese with English abstract). p. 1-31.
- Moor, D. S., and McCabe, G. P., 1999, *Introduction to the practice of statistics*: New York, W.H. Freeman and Company, 825 p.
- Mpodozis, C. and Ramos, V. A., 1989, The Andes of Chile and Argentina.: In Ericksen, G.E., T Cañas Pinochet, and J.A. Reinmund eds., *Geology of the Andes and its relation to hydrocarbon and mineral resources. Circum-Pacific Earth Science Series*, v. 11.

- Mykietiuk, K., Cábana, M. C., Echavarría, L., Etcheverry, R. and Fernández, R. R., 2000, Análisis estructural en el área de la Estancia Flecha Negra, Macizo del Deseado, Provincia de Santa Cruz: Relaciones con manifestaciones de oro y plata.: V Congreso de Mineralogía y Metalogenia, INREMI, La Plata, Publicacion 6, p. 351-355.
- Mykietiuk, K., Gobbo, E. J. and Fernández, R. R., 2002, Análisis estructural vinculado a la alteración hidrotermal del área de la Estancia La Esperanza, Macizo del Deseado, Santa Cruz.: In M.J. Haller (ed.) Geología y Recursos Naturales de Santa Cruz. Relatorio del XV Congreso Geológico Argentino, El Calafate.
- Nullo, F. E., 1991, Cuencas extensionales del Mesozoico inferior en el extremo sur de Sudamérica. Un modelo transpresional.: Asociacion Geologica Argentina, Revista, v. XLVI, p. 115-126.
- O'Leary, D. W., Friedman, J. D. and Pohn, H. A., 1976, Lineaments and linear lineation: Some proposed new standards for old terms.: Geological Society of America, Bulletin, v. 87, p. 1463-1469.
- Palma, M. A., 1989, Los eventos geológicos del Macizo del Deseado durante la evolución tectónica del continente Austral.: Reunión Sobre Geotranssectas de América del Sur, Mar del Plata o Montevideo, 1989, p. 97-101.
- Palma, M. A. and Ubaldón, M. C., 1988, Las sedimentitas gondwánicas de la Formación La Golondrina en la Estancia Dos Hermanos, Provincia de Santa Cruz.: Asociación Geológica Argentina, Revista (43), v. 3, p. 388-403.
- Pankhurst, R. J. and Rapela, C. R., 1995, Production of Jurassic rhyolite by anatexis of the lower crust of Patagonia: Earth and Planetary Science Letters, v. 134, p. 23-36.
- Panza, J. L., 1982, Descripción geológica de las Hojas 53e "Gobernador Moyano" y 54e "Cerro Vanguardia": Servicio Geológico Nacional (inédito). p. 197 p.
- Panza, J. L., 1994, Hoja Geológica 4969 - II (Tres Cerros), Provincia de Santa Cruz.: Dirección Nacional del Servicio Geológico, Secretaría de Minería de la Nación. Programa Nacional de Cartas Geológicas de la República Argentina (1:250000), Boletín N° 213, p. 103.
- Panza, J. L. and Cobos, J. C., 2001, Hoja Geológica 4769-III, Destacamento La Maria.: Servicio Geológico Minero Argentino, Subsecretaría de Minería de la Nación. Programa Nacional de Cartas Geológicas de la República Argentina (1:250000), Boletín N°296.
- Panza, J. L. and Marín, G., 1998, Hoja Geológica 4969-I, Gobernador Gregores.: Servicio Geológico Minero Argentino, Subsecretaría de Minería de la Nación. Programa Nacional de Cartas Geológicas de la República Argentina (1:250000), Boletín N°239.
- Patterson, A. L., 1934, A Fourier series method for the determination of the component of intra-atomic distances in crystals.: Physics Reviews, v. 46, p. 372-376.
- Patterson, A. L., 1935, A direct method for the determination of the components of intra-atomic distances in crystals: Zietschrift für Kristallographie, v. 90, p. 517-554.
- Perutz, M. F., 1942, X-ray analysis of haemoglobine.: Nature, v. 149, p. 491-494.
- Pezzuchi, H., 1978, Estudio geológico de la zona de estancia Dos Hermanos-estancia 25 de marzo y adyacencias, Departamento Deseado, Provincia de Santa Cruz.: Facultad de Ciencias Naturales y Museo, Universidad Nacional de La Plata, Tesis Doctoral N° 365 (inédito).
- Pirajno, F., 1992, Hydrothermal Mineral Deposits: Principles and Fundamental Concepts for the Exploration Geologist., Springer-Verlag, 709 p.
- Prakash, A., 2001, Radiometric Aspects (Chapter 8). in Janssen, L. L. F., and Huurneman, G. C., eds., Principles of remote sensing. ITC Educational Textbook Series, International Institute for Aerospace Survey and Earth Sciences (ITC).
- Ramos, V. A., 1983, Evolución Tectónica y metalogénesis de la Cordillera Patagónica.: II Congreso Nacional de Geología Económica, Actas I, p. 108-124.
- Ramos, V. A., 1984, Patagonia: ¿Un Continente Paleozóico a la deriva?: IX Congreso Geológico Argentino, Actas II, p. 311-325.
- Ramos, V. A., 1999, Las provincias geológicas de la República Argentina, Geología Argentina: Buenos Aires, Instituto de Geología y Recursos Minerales, Anales 29 (3), p. 41-96.
- Ramos, V. A., 2002, Evolución Tectónica.: In M.J. Haller (Edit.): Geología y Recursos Naturales de Santa Cruz. Relatorio del XV Congreso Geológico Argentino, El Calafate, I-22, p. 1-23.
- Ramos, V. A., Jordan, T. E., Allmendinger, R. W., Mpodozis, C., Kay, S. M., Cortes, J. M. and Palma, M., 1986, Paleozoic terranes of the central Argentine-Chilean Andes.: Tectonics, v. 5, p. 855-880.
- Ramsay, J. G., 1967, Folding and fracturing of rocks., McGraw-Hill, N.Y.
- Reimer, W., Miller, H. and Mehl, H., 1996, Mesozoic and Paleozoic Paleo-stress fields of the South Patagonian Massif deduced from structural and remote sensing data.: In: Storey, B.C., King, E.C., and Livermore, R.A. (eds.), Weddell Sea tectonics and Gondwana break-up, Geological Society Special Publication N° 108, p. 73-85.

- Rein, B. and Kaufmann, H., 2003, Exploration for gold using panchromatic stereoscopic intelligence satellite photographs and Landsat TM data in Hebei area, China.: *International Journal of Remote Sensing*, v. 24, p. 2427-2438.
- Rokos, D., Mavrantza, R., Vamvoukakis, K., St-Seymour, Kouli, M., Karfakis, I. and Denes, G., 2000, Localization of alteration zoning for the detection of epithermal gold by integration of remote sensing and geochemical techniques: Lesvos Island, Aegean Sea, Hellas.: *Proceedings of the Fourteenth International Conference on Applied Geologic Remote Sensing*, Las Vegas Nevada, p. 161-168.
- Sabins, F. F., 1999, Remote sensing for mineral exploration: *Ore Geology Reviews*, v. 14, p. 157-183.
- Sanders, G., 2000, Regional geologic setting of the gold-silver veins of the Deseado Massif, Southern Patagonia, Argentina.: *Argentina Mining 2000: Exploration, Geology, Mine Development and Business Opportunities Conference*, Engineering and Mining Journal and LatinoMineria, Mendoza., p. 60.
- Schalamuk, I. B., De Barrio, R. E., Zubia, M., Genini, A. and Echeveste, H., 1999, Provincia auroargentífera del Deseado, Santa Cruz, in Zappettini, E., ed., *Recursos Minerales de la República Argentina.*, Anales 35, Instituto de Geología y Recursos Minerales, SEGEMAR., p. 1178-1188.
- Schalamuk, I. B., de Barrio, R. E., Zubia, M. A., Genini, A. and Valvano, J., 2002, Mineralizaciones auroargentíferas del Macizo del Deseado y su encuadre metalogénico, Provincia de Santa Cruz: *Relatorio XV Congreso Geológico Argentino*, El Calafate.
- Schalamuk, I. B., Zubia, M., Genini, A. and Fernandez, R. R., 1997, Jurassic epithermal Au-Ag deposits of Patagonia, Argentina: *Ore Geology Reviews*, v. 12, p. 173-186.
- Sillitoe, R. H., 2002, Rifting, bimodal volcanism, and bonanza gold veins.: *Society of Economic Geologists, Newsletter N° 48*, p. 24-26.
- Stipanovic, P. and Reig, A. O., 1956, El Complejo Porfírico de la Patagonia extraandina y su fauna de anuros.: *Acta Geológica Lilloana 1*., p. 185-297.
- Suzen, M. L. and Toprak, V., 1998, Filtering of Satellite Images in Geological Lineament Analyses: An Application to a Fault Zone in Central Turkey.: *International Journal of Remote Sensing*, v. 19, p. 1101-1114.
- Townley, B. K., Maksaev, V., Palacios, C., Lahsen, A. and Parada, M. A., 2000, Base and precious metals geochemistry of rock units of the mainland Aisén region, Chilean Patagonia.: *Journal of Geochemical Exploration*, v. 68, p. 21-46.
- Uliana, M. A. and Biddle, K. T., 1988, Mesozoic-Cenozoic paleogeographic and geodynamic evolution of Southern South America.: *Revista Brasileira de Geociências*, v. 18, p. 172-190.
- Uliana, M. A., Biddle, K. T. and Cerdan, J., 1989, Mesozoic extension and the formation of Argentine sedimentary basins.: In A.J. Tankard and H.R. Balkwill, eds., *Extensional Tectonics and Stratigraphy of the North Atlantic Margins: AAPG Memoir 46*, Chapter 39, p. 599-614.
- Uliana, M. A., Biddle, K. T., Phelps, D. W. and Gust, D. A., 1985, Significado del Vulcanismo y extensión mesojurásicos en el extremo meridional de Sudamérica.: *Asociación Geológica Argentina, Revista*, v. 40, p. 231-253.
- Varela, R., Pezzuchi, H., Genini, A. and Zubia, M., 1991, Dataciones de rocas magmáticas en el Jurásico inferior del nordeste del Macizo del Deseado, Santa Cruz.: *Asociación Geológica Argentina, Revista* 46, v. 3-4, p. 257-262.
- Vassilas, N., Perantonis, S., Charou, E., Tsenoglou, T., Stefouli, M. and Varoufakis, S., 2002, Delineation of lineaments from satellite data based on efficient neural network and pattern recognition techniques.: *Methods and Applications of Artificial Intelligence, Second Hellenic Conference on Artificial Intelligence, SETN 2002*. 2002, *Proceedings, Thessaloniki, Greece, 2002*, p. 355-366.
- Vearncombe, J. and Vearncombe, S., 1999, The Spatial Distribution of Mineralization: Application of Fry Analysis: *Economic Geology*, p. 475-486.
- White, N. C. and Hedenquist, J. W., 1990, Epithermal environments and styles of mineralization: Variations and their causes, and guidelines for exploration.: *Journal of Geochemical Exploration*, v. 36, p. 445-474.
- White, N. C. and Hedenquist, J. W., 1995, Epithermal gold deposits: styles, characteristics and exploration.: *Society of Economic Geologists, Newsletter N° 23*, p. 9-13.
- Winter, H. d. I. R., 1984, Tectonostratigraphy, as applied to analysis of South African Phanerozoic basins.: *Transactions Geological Society South Africa*, v. 87, p. 169-179.
- Wright, D. F. and Bonham-Carter, G. F., 1996, VHMS favorability mapping with GIS-based integration models, Chisel Lake-Anderson Lake area.: *Geological Survey of Canada, Bulletin* 426, p. 339-401.